

Aus dem Institut für Integrative Neuroanatomie
der Medizinischen Fakultät Charité – Universitätsmedizin Berlin

DISSERTATION

"Improved Morphological Characterisation of Cortical Neurons"

zur Erlangung des akademischen Grades
Doctor medicinae (Dr. med.)

vorgelegt der Medizinischen Fakultät
Charité – Universitätsmedizin Berlin

von

Felix Johannes Bolduan

aus Berlin

Datum der Promotion: 03.12.2021

Table of contents

1. Summary	3
Abstract	3
Abstract Deutsch	3
1.1. Introduction.....	4
1.2. Methods.....	5
1.3. Results	11
1.4. Discussion	18
1.5. References	21
2. Anteilserklärung / eidesstattliche Versicherung	24
3. Selected papers.....	26
3.1. Minimizing shrinkage of acute brain slices using metal spacers during histological embedding.....	26
3.2. Dendritic action potentials and computation in human layer 2/3 cortical neurons	39
3.3. Distinct Localization of SNAP47 Protein in GABAergic and Glutamatergic Neurons in the Mouse and the Rat Hippocampus	44
4. Curriculum vitae.....	62
5. List of Publications.....	63
6. Danksagung	64

1. Summary

Abstract

Analyzing the morphology and molecular features of neurons are major components in neuroscientific studies and classifications. For this, elaborate techniques, like intracellular biocytin staining of single neurons in acute brain slices, immunofluorescence labeling and confocal microscopy, were applied. Here, these techniques were used to study the SNAP47 protein distribution in the hippocampus of mice and rats and the morphology of human cortical pyramidal neurons. Although these approaches provide accurate results, a considerable problem in morphological analyses remains: the reduction in thickness of slices (shrinkage) due to the embedding under cover slip. In this thesis, the time course of shrinkage in conventional embedded slices and its impact on the morphology of neurons and anatomical parameter are shown. This impact is not compensable with usually used linear correction approaches. Moreover, this dissertation provides a novel method for the embedding of acute brain slices, which is effective in reducing the shrinkage and the resulting error. Thereby, the preciseness of morphological studies can be substantially improved.

Abstract Deutsch

Analysen morphologischer und molekularer Eigenschaften von Nervenzellen sind essenzielle Komponenten neurowissenschaftlicher Studien und Klassifikationen. Aufwändige Methoden, wie intrazelluläre Biozytinfärbung in frischen Gehirnschnitten und Immunfluoreszenzfärbungen kombiniert mit konfokaler Mikroskopie werden hierfür benutzt. Diese Arbeit zeigt, dass jene Techniken sowohl für die SNAP47 Protein Verteilung in Hippocampi von Mäusen und Ratten als auch für morphologische Analysen humaner, kortikaler Nervenzellen benutzt werden können. Auch wenn diese Methoden präzise Ergebnisse liefern, bleibt ein bedeutendes Artefakt in morphologischen Analysen bestehen: Die Reduktion der Schnittdicke (Schrumpfen) durch konventionelles Einbetten unter Deckgläsern. Diese Dissertation beschreibt den zeitlichen Verlauf dieses Artefakts und den Einfluss auf morphologische Parameter. Es wird dargestellt, dass dieser Einfluss nicht durch gewöhnlich angewandte lineare Methoden kompensierbar ist. Des Weiteren wird eine neue Eindeckmethode angeboten, die effektiv das Schrumpfen und resultierende Fehler in morphologischen Parametern reduziert. Auf diese Art kann die Präzision morphologischer Untersuchungen in hohem Maße gesteigert werden.

1.1. Introduction

Understanding of brain function requires a profound knowledge of its structural and functional units: the neurons. It is widely recognized, that neuronal activity represents the biological correlate for information encoding and processing underlying cognition. However, until today many neuron types in the rodent or human brain are not characterized in a comprehensive manner in terms of their anatomical, physiological and molecular properties (Allen Institute for Brain Science, 2015; Shen, 2015). Thus, there is a reasonable motivation to further investigate and classify the building blocks of our brain.

Characterizing neuronal morphology is essential for their classification and also for their functional understanding: The localization of the somato-dendritic domain defines potential inputs to a neuron and its dendritic length and diameters determine electronic properties, essential for our understanding of their network functions. Furthermore, dendritic spines, its development and density are involved in long-term potentiation and learning (Matsuzaki *et al.*, 2004) and, finally, the location of the axonal branching helps to identify the target region of a neuron. Thus, there is a big need of precise morphological analyses of neurons, which additionally provide essential data for performing computational analysis (e.g. Traub *et al.*, 1994).

The history of neuroanatomical studies looks back a long history: More than 100 years ago, Camillo Golgi and Santiago Ramón y Cajal performed first morphological studies of Golgi-stained neurons (Ramón y Cajal, 1909, 1911). Today, morphological characterization is mostly performed by intracellular biocytin staining while doing patch-clamp recordings with subsequent visualization (Booker *et al.*, 2014): While early analysis was performed with conventional microscopes and drawing the neurons by hand, technical advances today enable the precise digital imaging by confocal microscopy, a technique which was invented and patented by Marvin Minsky in 1950' (Minsky, 1988), and computer assisted 3D reconstructions of the neurons. Confocal microscopy is not only a key method in order to perform morphological studies, by combining it with immunofluorescence labeling, it may be also used for the analysis of molecular features (e.g. immunocytochemical detection of protein expression) of neurons - beside the morphology another important point in neuroscientific investigations.

Morphological analysis depends critically on faithful preservation of the structure of neurons and the surrounding nervous tissue during histological processing. Despite the substantial progress during the last century, one major artefact of morphological analysis remains and counteracts accurate preservation of nervous tissue: the reduction in thickness of acute slices (shrinkage) along the z-axis (here and anywhere else in this thesis: the axis that is perpendicular to the cut surfaces of the slice) due to the histological processing and the embedding under cover slip.

The histological processing could produce shrinkage especially when it includes dehydration and drying procedures (Pyapali *et al.*, 1998; Hellwig, 2000). Avoiding dehydration during the processing steps and using aqueous-mounting medium for embedding could reduce substantial shrinkage but cannot totally prevent it (Egger *et al.*, 2008; Swietek *et al.*, 2016). Independently, if significant z-shrinkage was detected, it was usually compensated by applying a linear correction factor to the z-coordinates of cells reconstructions (Pyapali *et al.*, 1998; Hellwig, 2000; Marx *et al.*, 2012; Degro *et al.*, 2015). However, the time course of shrinkage and its impact on the morphology of cells are unknown. Moreover, the adequacy of compensation with a linear correction factor is not certain.

The main aim of this thesis is to describe an approach how to obtain accurate images of neurons and analyze their molecular features by using confocal microscopy. The impact of tissue shrinkage along the z-axis on the morphology of the cells is shown. It is demonstrated that the routine use of linear correction factors is an inappropriate approach to compensate for the shrinkage. This thesis further describes a novel way of embedding slices, which can significantly minimize shrinkage and its resulting artefact. In this way, uncompromised high resolution images and reconstructions of neurons can be achieved that can be used for following accurate computational analyses (Gidon *et al.*, 2020).

1.2. Methods

This thesis, including all experimental procedures and data handling, complies with Charité's statutes of good scientific practice ("Satzung der Charité zur Sicherung guter wissenschaftlicher Praxis").

In total, three sets of experiments were performed and published in three distinct papers: One deals with the shrinkage of acute brain slices, with its impact on

morphological parameters and with a new method, which minimizes this artefact (Bolduan *et al.*, 2020). The second set of experiments is an investigation about the differential distribution of the synaptosomal-associated protein of 47kDa (SNAP47) in rodent hippocampal neurons (Munster-Wandowski *et al.*, 2017). The third set is a morphological study of human cortical pyramidal neurons, which forms part of the publication by Gidon *et al.* (2020).

Slice preparation

Experiments and animal maintenance were performed in accordance with local (LaGeSo, Berlin, T 0215/11), national (German Animal Welfare Act) and international guidelines (EU Directive 2010/63/EU). For all experiments that deal with tissue shrinkage along the z-axis, male and female rats (P21-25; 'Wistar-VGAT-Venus' rats), which express yellow fluorescent protein (YFP) Venus, a yellow shifted variant of the green fluorescent protein (GFP) under the promoter of the vesicular GABA-transporter (VGAT) (Uematsu *et al.*, 2007)) were anesthetized with isoflurane and decapitated. Brains were quickly dissected and transferred to carbogenated (95% oxygen/ 5% carbon dioxide), semifrozen, sucrose-based artificial cerebrospinal fluid [sACSF, containing (in mM) NaCl (87), KCl (2.5), NaHCO₃ (25), NaH₂PO₄ (1.25), Glucose (25), Sucrose (75), Na₂-Pyruvate (1), Na₂-Ascorbate (1), MgCl₂ (7), CaCl₂ (0.5)]. 300µm thick, horizontal slices were cut of the hippocampal formation by using a vibratome (VT1200s, Leica, Germany) and were subsequently transferred to carbogenated, warm (34°C) sACSF. After 30min, the temperature of the sACSF in the storage chamber was decreased to room temperature. To study the time course of shrinkage, some of these slices were directly fixed with 4% paraformaldehyde (PFA) in 0.1M Phosphate buffer (PB) for 24h at 4°C, the rest was used for patch-clamp recordings.

Tissue for morphological studies of human pyramidal neurons was obtained from resections of the anterior temporal lobe of epilepsy and brain tumor patients carried out at the Department of Neurosurgery of the Charite (Gidon *et al.*, 2020). All experiments involving human brains were accepted by the Ethics Committee of the Charité – Universitätsmedizin Berlin and comply with the Declaration of Helsinki. After surgical resection, colleagues from the Larkum laboratory did further tissue processing for the electrophysiological experiments. In brief, removed brain tissue was transported in carbogenated semifrozen N-methyl-D-glucamin (NMDG) solution

[(containing (in mM): NMDG (93), HCl (93), KCl (2.5), NaH₂PO₄ (1.2), NaHCO₃ (30), MgSO₄ (10), CaCl₂ (0.5), HEPES (20), glucose (25), Na-L-ascorbate (5), thiourea (2), Na-pyruvate (3)], choline solution [containing (in mM) Choline chloride (110), KCl (2.5), NaH₂PO₄ (1.25), NaHCO₃ (26), MgCl₂ (7), CaCl₂ (0.5), 15 glucose (10), Na-L-ascorbate (11.6), Na-pyruvate (3.1)] or sACSF [containing (in mM) NaCl (87), NaH₂PO₄ (1.25), KCl (2.5), CaCl₂ (0.5), MgCl₂ (3) Glucose (10), NaHCO₃ (25), Sucrose (75)] within 10-40min to the laboratory. After removal of the pia, tissue was cut into 300µm thick slices by using a vibratome (VT1200, Leica, Germany). Afterwards, slices were stored in either HEPES [identical to NMDG solution but with NaCl (92) instead of NMDG and HCL (93)] or artificial cerebrospinal fluid [ACSF, containing (in mM) NaCl (125), KCl (2.5), NaH₂PO₄ (1.25), NaHCO₃ (25), MgCl₂ (1), CaCl₂ (1), glucose (25)]

Patch-clamp recordings and filling of neurons

In order to perform morphological and shrinkage analyses of neurons, cells need to be intracellularly labeled and visualized. Therefore, patch-clamp experiments were necessary: acute hippocampal rat slices were transferred to a recording chamber, filled with 32°C ACSF [containing (in mM) NaCl (125), KCl (2.5), NaHCO₃ (25), NaH₂PO₄ (1.25), Glucose (25), Na₂-Pyruvate (1), Na₂-Ascorbate (1), MgCl₂ (1), CaCl₂ (2)]. Principal cells of the Subiculum were visualized by an upright microscope (BX-510, Olympus, Hamburg, Germany) equipped with a digital camera (Retiga-2000R, O Imaging, Surrey, Canada). On a horizontal electrode puller (P-97, Sutter Instruments, Novato, CA) patching pipettes were pulled from borosilicate glass capillaries (2 mm outer/1 mm inner diameter, Hilgenberg, Germany). Patch-clamp recordings were performed with a Multiclamp 700B amplifier (Molecular devices, San Jose, CA). Patched cells were filled with a biocytin containing intracellular solution [containing (in mM) κ-gluconate (130), KCl (10), MgCl₂ (2), EGTA (10), HEPES (10), Na₂-ATP (2), Na₂-GTP (0.3), Na₂-creatinine (1), and 0.1% Biocytin; 290–310 mOsm]. After 16-20 min in whole-cell configuration, a sufficient diffusion of biocytin into cells' dendrites could be assumed (Marx *et al.*, 2012). Recordings were terminated and slices were fixed with 4% PFA in 0.1M PB for 24h at 4°C.

Patch-clamp recordings and intracellular biocytin filling of cortical human pyramidal neurons were performed by colleagues in the Larkum laboratory. The procedure was similar, except that dual whole-cell recordings from the soma and dendrites were

performed. Other minor differences refer to the technical equipment (a Dagan BVC-700A amplifier (Dagan Minneapolis, MN) was used) and the internal solution [containing (in mM) K-gluconate (130), KCl (20), Mg-ATP (4), Na₂-phosphocreatine (10), GTP-Tris (0.3), HEPES (10) and 0.1% Biocytin; 300 mOsm] that were used.

Histological processing of acute slices

For morphological and shrinkage analyses all fixed acute slices – both rodent and human - were first intensely rinsed in PB. To visualize biocytin labeled neurons, they were incubated with Alexa Flour-647-conjugated streptavidin (Invitrogen, Eugene, OR; dilution 1:1000 in PB, including 0.05% NaN₃ and 0.1% Triton-X as detergent) overnight at 4°C (histological processing like previously described: Booker *et al.*, 2014). Streptavidin binds with high affinity to biocytin. As biocytin is distributed through the entire intracellular space, the neurons can be completely visualized by illuminating with a red laser (643 nm wavelength), exciting the conjugated fluorophore to emit light in the infrared range.

After the incubation, slices were rinsed again in PB and finally embedded in a solidifying water soluble mounting medium (Fluoromount, Southern Biotech, AL) either conventionally on glass slides with a coverslip or sandwiched between two coverslips with a 300 µm thick custom-made metal spacer (wh Münzprüfer, Berlin, Germany). One coverslip was glued with cyanoacrylate (Uhu, Bühl, Germany) onto the metal spacer. This one functioned as the ground for the mounting. The other coverslip was positioned on top of the mounted slice and sealed with nail polish. Some slices without biocytin-filled cells were embedded with a 300µm thick agar spacer between the glass slide and the coverslip (Booker *et al.*, 2014; Degro *et al.*, 2015).

Perfusion, sectioning and histological processing of brains for analyses of the SNAP47 protein distribution

Perfusion and sectioning for examining the SNAP47 protein distribution was performed by members of the laboratory (Munster-Wandowski *et al.*, 2017): In summary, male VGAT-YFP rats and mice (3 and 2.5 months old, respectively) were anesthetized with ketamine (Actavis) and xylazine (Bayer Health Care, Berlin, Germany) and perfused transcardially with fixative containing 4% PFA (Electron Microscopy Sciences, Hatfield, PA), 0.2% picric acid (Fluka Chemie, Buchs,

Switzerland) diluted in 0,1 M PB. The brains were dissected and cut into blocks by using a coronal rodent brain matrix (ASI Instruments, Warren, MI).

Afterwards, the coronal tissue blocks were cut at 20 µm in a cryostat (CM 3050S; Leica, Wetzlar, Germany). Afterwards, sections were rinsed in PB and incubated in a blocking solution containing 10% normal goat serum (NGS), 0.3% Triton-X100 and 0.05%NaN₃ in PB for 1 hour at room temperature. Subsequently, the primary antibodies (anti- SNAP47, Synaptic System, Göttingen, Germany, Cat. No.: 111403, host: rabbit, dilution: 1:300 and anti-GFP (to detect GABAergic interneurons), UC Davis/NIH NeuroMab, USA, Cat. No.: 75-132, host: mouse, dilution: 1:2000 in PB, including 5% NGS, 0.3% Triton-X100, 0.05% NaN₃) were applied. After an incubation period of 2-3 days at 4°C, sections were intensely rinsed and incubated over night at 4°C with the fluorochrome conjugated secondary antibodies (goat anti-rabbit, Life Technologies, Darmstadt, Germany, dilution: 1:500 and goat anti-mouse, Invitrogen, dilution: 1:300 in PB, including 3% NGS, 0.1% Triton-X100, 0.05% NaN₃). Finally, sections were mounted in Fluorsave mounting medium (Calbiochem, San Diego, CA) on a glass slide and coverslipped.

Measuring of z-shrinkage

Slice thickness and its time course was estimated and compared between distinct embedding techniques in fixed slices that do not contain biocytin-filled neurons. For this purpose, a confocal microscope (Fluo View 1000, Olympus) with a silicone oil-immersion 30x (N.A 1.05) objective lens was used. Slices top and bottom were focused and the table's vertical movement was taken as the slice thickness. Slices embedded with metal spacers need a special holder (whMünzprüfer, Berlin, Germany) in order to perform confocal imaging.

Morphological analysis of intracellular stained neurons

Intracellular stained rodent and human neurons were imaged with a 20x (N.A 0.75) or a 30x (N.A 1.05) silicon oil-immersion objective on the confocal microscope. For performing 3D reconstructions, a 30x objective was used and image stacks were collected at 1024x1024 resolution in the xy plane and 1µm steps for the human neurons or 0.5µm steps for the rat neurons along the z-axis. The excitation wavelength was 635nm for Alexa Fluor-647-conjugated streptavidin. Single image stacks were stitched together in the FIJI/ImageJ software environment (Schindelin *et*

al., 2012) using the 3D stitching plugin (Preibisch *et al.*, 2009). Finally, 3D reconstructions were performed with the simple neurite tracer plugin (Longair *et al.*, 2011) or the Neutube software package (Feng *et al.*, 2015). Reconstructed neuronal morphology was stored in the SWC file format (Cannon *et al.*, 1998).

To study the impact of shrinkage on the morphology of cells, selected slices embedded with the metal spacer, containing biocytin-filled rodent neurons, were embedded a second time without any spacer. After 11-14 days, these cells were imaged again. Thereby, we were able to obtain two different images of the same cell, first in a minimal shrunken state embedded with a metal spacer and second in a shrunken state embedded without any spacer. A second reconstruction of the neuron was accomplished. The total dendritic lengths as a morphological parameter were used to demonstrate the impact of slice shrinkage.

Measurements of the total dendritic lengths and potential shrinkage compensation were performed using custom made “hoc” scripts in the Neuron software environment (Hines & Carnevale, 1997). Shrinkage compensation was performed by applying a linear correction factor to the z-coordinates of neurons reconstruction. This factor was determined by the quotient of the slice thickness measured embedded with the metal spacer system and the one embedded on a normal glass slide without any spacer. To examine deformations of the slice in the xy plane due to the embedding, the z-values of the SWC files were set to zero and the total dendritic lengths were estimated of the collapsed neuron under the different embedding conditions. Moreover, two-dimensional extent of neuronal structures/dendritic segments were estimated in a xy projection of an image of the minimally shrunken, metal spacer embedded neuron and compared to their extent in the shrunken state with no spacer.

Estimation of shrinkage degrees in slices portions

In order to assess evidence for a non-linear shrinkage, yz projections of confocal image stacks of three neurons both in the unshrunken and the shrunken state were trisected in an upper, a middle and a lower third. Distances parallel to the z-axis of neuronal structures/dendritic segments were estimated in each third. Their extents were compared between the shrunken and the unshrunken state of the cell. Thereby, the degree of shrinkage in the upper, middle and bottom part of the slice could be estimated and compared. The difference to 1 of the quotient of the shrunken length

and the unshrunk length of distances of neuronal structures is defined as the degree of shrinkage.

Analysis of SNAP47 protein expression

For studying the distribution of the SNAP47 protein, the coronal hippocampal slices were imaged on our confocal laser-scanning microscope by using a 30x (N.A 1.05) or a 60x (N.A 1.30) silicon oil immersion lens. The excitation wavelengths were 488nm for anti-mouse Alexa Fluor-488 and 635 nm for anti-rabbit Alexa Fluor-647. Image stacks were collected at 1024x1024 resolution in the xy plane and 0.5 μm steps along the z-axis. In order to compare the SNAP47 fluorescence signal intensity between mouse and rat hippocampal GABAergic interneurons, we determined the mean labeling intensity over the somata (excluding nucleus) of these neurons and the surrounding neuropil in the mouse and the rat hippocampus by using the FIJI/ImageJ software package.

Statistics

Statistical analysis was performed by using Graphpad Prism version 5.00 (GraphPad Software, San Diego, CA). The slice thickness dependence on time and embedding method was compared with a two-way ANOVA for repeated measurements. For comparison of the first and last measurement of slice thickness as well as for the degree of shrinkage in distinct depths of the slice one-way analyses of variance (ANOVA) with Bonferroni's Multiple Comparison Tests was used. All other paired and unpaired data sets were compared with non-parametric Wilcoxon matched-pairs tests or Mann-Whitney tests, respectively. Data is shown as mean \pm Standard deviation. Statistical significance was assumed if $p < 0.05$.

1.3. Results

Analyzing molecular features of neurons using the example of the SNAP47 protein

Using immunofluorescence labeling and confocal microscopy is an appropriate approach to examine molecular features of neurons and the cellular distribution of specific proteins in distinct areas. Here, this is demonstrated by using the example of the synaptosomal-associated protein of 47kDa (SNAP47) distribution.

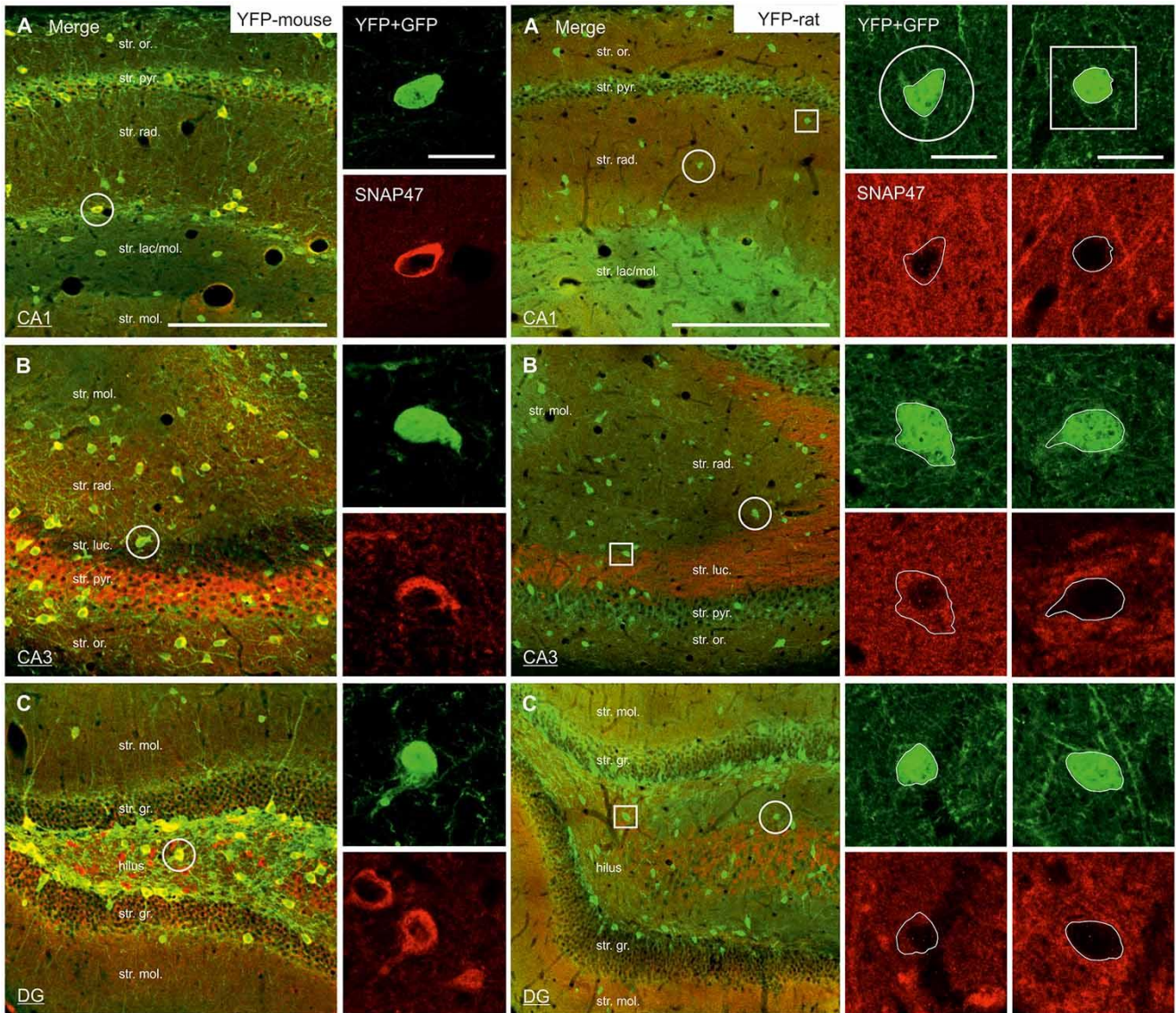


Figure 1: SNAP47 expression in the hippocampus and in its YFP-positive INs of VGAT-Venus (YFP) transgenic mice

Confocal images of double immunolabeling for YFP (green) and SNAP47 (red) in the CA1 (A), the CA3 areas (B) and the dentate gyrus (DG; C) of VGAT-Venus (YFP) transgenic mice. Insets on the right show strong cytoplasmic localization of SNAP47 (bottom images) in YFP-positive cell bodies (top images). Scale bars represent, (A–C), 250 μ m; insets, 20 μ m. (adapted from Munster-Wandowski *et al.*, 2017)

Figure 2: SNAP47 expression in the hippocampus and in its YFP-positive INs of VGAT-Venus (YFP) transgenic rats

Confocal images of double immunolabeling for YFP (green) and SNAP47 (red) in the CA1 (A), the CA3 area (B) and the DG (C) of VGAT-Venus (YFP) transgenic rats. Insets on the right show SNAP47-positive INs (circles, first column) with weak cytoplasmic labeling (bottom images) in the YFP-positive cell bodies (top images) and SNAP47-negative INs (squares, second column). Scale bars represent, (A–C), 250 μ m; insets, 20 μ m. (adapted from Munster-Wandowski *et al.*, 2017)

To this end, we performed double immunostaining against SNAP47 and GFP (to detect GABAergic Interneurons (IN), see Methods) in hippocampal slices from mouse and rat. Two-channel confocal imaging of these slices revealed a different expression of this protein in distinct hippocampal areas from mouse or rat (Fig. 1 and 2). The

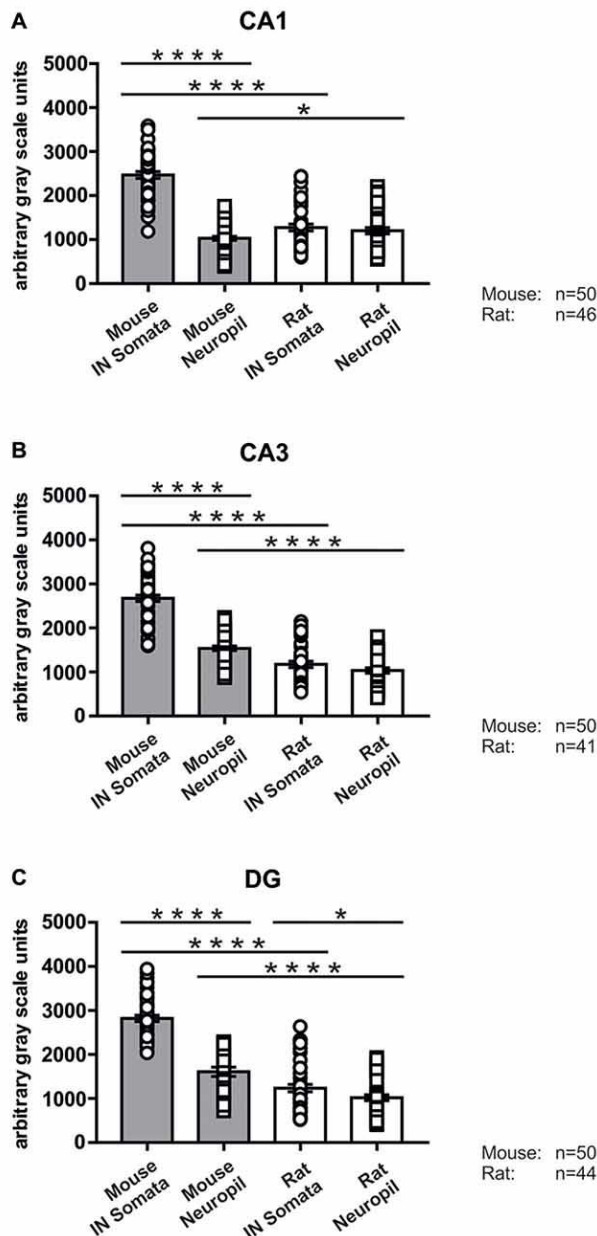


Figure 3: Immunolabeling intensities for SNAP47 in YFP-positive INs and surrounding neuropil in the mouse and the rat hippocampus

Summary bar charts of the immunolabeling intensity for SNAP47 in the somata of YFP-positive INs and surrounding neuropil in the CA1 area (A), the CA3 area (B) and the DG (C) of the mouse and the rat hippocampus. * $P = 0.04$, **** $P < 0.0001$. (Adapted from Munster-Wandowski *et al.*, 2017)

differences are most striking in the hippocampal CA3 area between mouse and rat. In mouse, there is a strong immunoreactivity in the Stratum pyramidale and a very weak one in the Stratum lucidum. In rat, the staining pattern is exactly the opposite. This emphasizes a species-specific SNAP47 distribution. In addition, the SNAP47 expression in GABAergic INs is also different between mice (high somatic immunoreactivity against SNAP47, Fig.1) and rats (weak/no somatic immunoreactivity against SNAP47, Fig 2). By measuring the mean intensity of immunofluorescence (arbitrary gray scale units) in the cytoplasm of YFP-positive cell bodies and comparing it with the mean intensity in the surrounding neuropil, we could quantitatively confirm these observations (Fig. 3).

Analyzing the morphology of human cortical pyramidal neurons

To obtain accurate images of neurons for subsequent analyses, acute human brain slices were

made. Subsequently, patch-clamp recordings of cortical pyramidal cells with intracellular biocytin filling, histological procedures, confocal microscopy and reconstruction were performed (see Methods). In this way, we imaged and identified 87 human pyramidal cells in 51 human brain slices. We have selected 12 of these

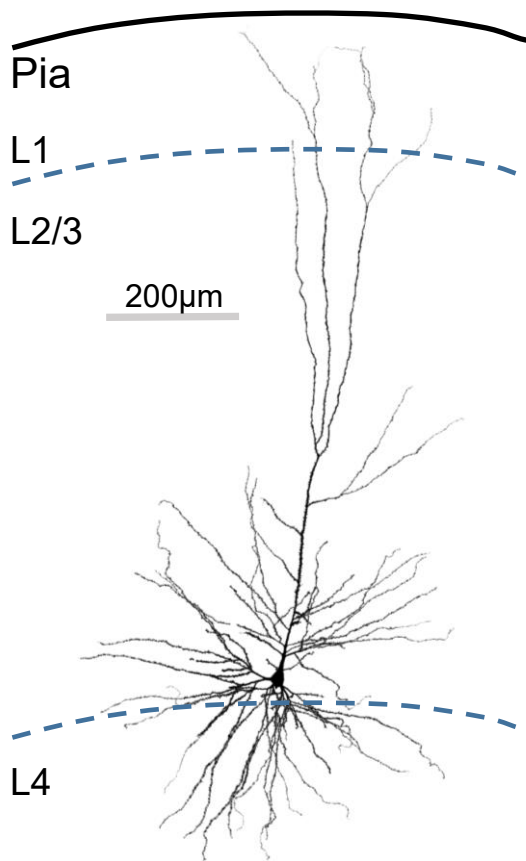


Figure 4: Reconstruction of a L2/3 pyramidal neuron

Intracellular stained L2/3 human pyramidal neuron 1130 μm below the pial surface (black line). Dashed lines represent the cortical layer borders. (Adapted from Gidon *et al.*, 2020)

neurons for 3D reconstructions (representative result: Fig. 4). This morphological raw data served as the basis for any following analyses, i.e. estimation of the total dendritic length, of the distance to the pia, the diameter of certain dendritic portions, as well as the spine density. In our study (Gidon *et al.*, 2020), this morphological data revealed an interesting finding: The somata of the investigated layer 2 and 3 (L2/3) neurons were located around 850 μm below the pia mater, on average, whereas the apical dendrites extended up to it. From electrophysiological experiments, we found that subthreshold (steady-state) potentials attenuated from the apical dendrite to the soma with a length constant (λ_{steady}) of 195 μm and, reversely, back-propagating action potentials (bAPs) with a λ_{bAP} of 290 μm (Gidon *et al.*, 2020). Hence, there is a so much strong attenuation of electrical activity to and from distally located synapses that

active intrinsic properties are required to compensate for that. These active intrinsic properties were dendritic Ca^{2+} dependent action potentials (dCaAPs), a type of action potential that has been described in our study for the first time. To investigate the functional outcome of the dCaAPs, a compartmental model of a L2/3 pyramidal neuron was created (Gidon *et al.*, 2020). For this purpose, very accurate morphological data is required and interfering artefacts should be avoided. One major artefact is the collapse of slices along the z-axis (z-shrinkage) due to conventional embedding under coverslip.

Metal spacers reduce the shrinkage of embedded slices

In order to minimize z-shrinkage in acute slices we created the metal spacer system. This system consists of a metal spacer, which is in thickness equal to that of the

slices (300µm). The metal spacer and the embedded slice are sandwiched between two glass cover slips. This construction requires a special holder for imaging on a confocal microscope stage but enables imaging from both sides by flipping the metal spacer with the embedded slice in its holder. Thereby, even in thick slices deep structures could be imaged with a high signal to noise ratio.

To validate, whether this system can effectively minimize z-shrinkage, we first assessed the time course of shrinkage of 300µm thick acute slices embedded in a polymerizing aqueous mounting medium using three distinct techniques: (1) on a regular glass slide without any spacer and with coverslip (conventional embedding), (2) on a normal glass slide with a 300µm thick agar spacer between slide and coverslip, and (3) with the metal spacer system. The thickness of these slices was measured over a period of two months. The first measurement was performed three hours after embedding. Conventionally embedded slices (n=11) shrunk already by about 22 ± 8% in the first measurement (percentages referring to the nominal thickness of the acute slice of 300 µm), whereas slices with metal (n=8) or agar

A

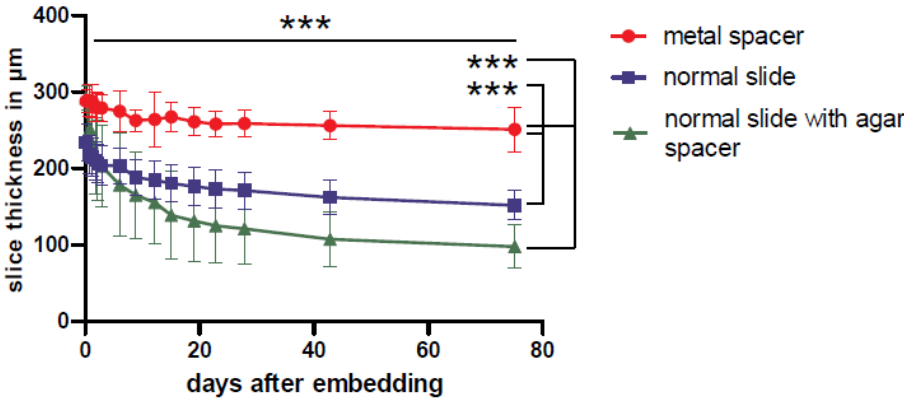
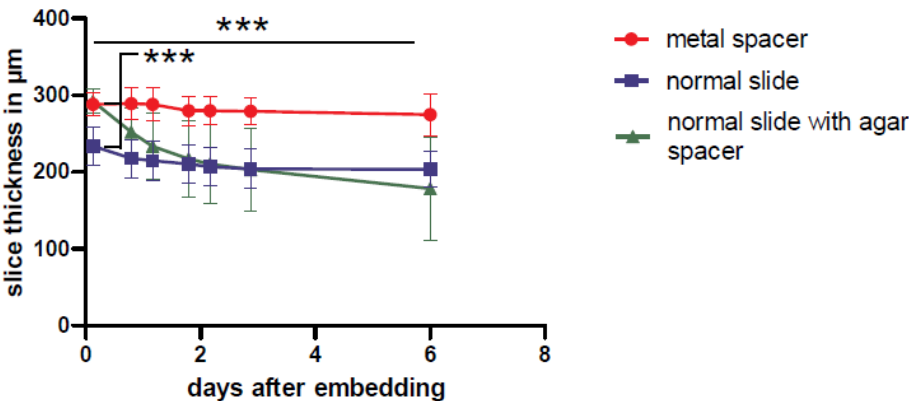


Figure 5: Shrinkage of acute slices depending on the embedding method

B



A Summary graph of the average slice thickness over time after embedding without any spacer (blue squares, n=11), with an agar spacer (green triangles, n=14) or a metal spacer (red circles, 8 slices). **B** The plot shows the same data at higher temporal resolution for the first six days. Error bars indicate standard deviation. (***) P < 0.001 (adapted from Bolduan et al., 2020)

spacers (n=14) showed only a minimal z-shrinkage of $4 \pm 5\%$ and $3 \pm 5\%$, respectively. Hence, a substantial initial z-shrinkage occurred without a spacer. Metal and agar spacers could minimize this initial shrinking process. The shrinking process continued over the next days and weeks for all slices and approached asymptotic levels beyond two months. However, the speed of shrinkage and the asymptotic level substantially differed between these three embedding approaches. Conventionally embedded slices shrunk by about $49 \pm 6\%$ after two months. Slices with agar spacer showed even a stronger shrinkage after two months; they shrunk by about $67 \pm 9\%$. In contrast, slices embedded with the metal spacer system showed only a shrinkage of $16 \pm 9\%$ when measured two months after embedding (Fig. 5A).

Thus, agar spacers can prevent the initial shrinkage, but are not useful to minimize shrinkage for the longer term, as the degree of shrinkage exceeded that of conventional embedded slices already six days post-embedding ($40 \pm 22\%$ vs. $32 \pm 7\%$; Fig 5B). In comparison, slices with the metal spacer system shrunk only by about $8 \pm 8\%$ six days after embedding.

In summary, metal spacers can substantially reduce but not fully prevent z-shrinkage.

The impact of shrinkage on anatomical parameters of intracellular stained neurons

Although z-shrinkage as an artefact has been recognized for a long time, its precise impact on the morphology of neurons and anatomical parameters has not been fully characterized yet. Previous studies used linear correction factors employed to the cell's three-dimensional reconstruction to compensate for shrinkage artefacts (Pyapali *et al.*, 1998; Hellwig, 2000; Marx *et al.*, 2012; Degro *et al.*, 2015). Whether this compensation is adequate remained unclear.

To assess the impact of shrinkage on the neurons morphology, we performed whole-cell patch-clamp recordings combined with intracellular staining of cortical pyramidal cells in 300 μ m thick acute hippocampal slices. After histological processing, we embedded all slices with the metal spacer system, imaged them on a confocal microscope and reconstructed the neuronal morphologies. Subsequently, all slices were embedded a second time on a normal glass slide without spacer (conventional embedding). 11 to 14 days after this second embedding, the neurons were imaged and reconstructed anew. Hereby, we obtained reconstructions of the somato-dendritic domains of six pyramidal neurons in a minimally shrunken state embedded with the metal spacer system and in a strongly shrunken state after conventional

embedding. We calculated the length of all dendritic branches (total dendritic length) as an anatomical parameter in the minimally shrunken state and the strongly shrunken state. The total dendritic length of cells was reduced by about $5.7 \pm 1.2\%$ ($P=0.0313$, six neurons) after the reembedding, indicating an alteration in anatomical parameters by z-shrinkage. However, when we applied a linear correction to the shrunken reconstruction – using the quotient of the slice thickness mounted with metal spacer divided by the thickness without spacer as correction factor – this led to an overcompensation of the total dendritic length by about $6.8 \pm 1.8\%$ on average ($P=0.0313$, six neurons).

Thus, z-shrinkage causes an error in anatomical parameters, which is not compensable, emphasizing the importance of minimizing shrinkage.

Two reasons could be responsible for this overcompensation: First, collapsing of slices along the z-axis is accompanied by an alteration in xy plane (the plane that is parallel to the slices cut surface). Second, the z-shrinkage is not a uniform process but rather differential/non-uniform, whereby the degree of shrinkage differs in distinct depths of the slice.

To analyze these two possibilities, we first checked if the slices showed evidence for deformation in the xy-plane. We projected the reconstructions of all six neurons both in the non-shrunken (made after embedding with the metal spacer system) and shrunken (made after conventional embedding) status into the xy plane and could thereby ignore their dimensions along the z-axis. The comparison of these 2D dendritic lengths in the two different embedding conditions revealed that the shrunken reconstruction was persistently larger by a factor of $5.2 \pm 2.3\%$ on average ($P=0.0313$, 6 neurons). Hence, conventional embedded slices without any spacer suffer not only a severe z-shrinkage, but also a mild dilation in the xy plane. This finding was confirmed by comparing the lengths of neuronal structures (i.e. dendritic segments) in xy projections of confocal image stacks in the non-shrunken state with those in the shrunken one. The 2D projected lengths of neuronal structures in the xy projection of the image of the shrunken, conventional embedded slice were larger by about $8.2 \pm 6\%$ ($P<0.0001$, 110 dendritic segments from 4 pairs of image stacks).

In order to investigate the possibility of a non-linear shrinkage, we estimated the degree of shrinkage in distinct depths of the slice (see Methods). We found a strong degree of z-shrinkage in the top and bottom third of the slice ($45 \pm 14\%$ and $44 \pm 15\%$, respectively) and a lower degree in the middle third of the slice ($30 \pm 12\%$),

indicating a non-linear shrinkage ($P=0.0105$, ANOVA, 95%CI of differences between upper and middle third: 0.01770 to 0.2748, between middle and lower third: -0.2667 to -0.009547, Bonferroni's multiple comparison test, 15 dendritic segments in each sample from 3 slices).

In summary, we demonstrated that shrinkage along the z-axis has an impact on the morphology and anatomical parameters of the neuron. This shrinkage is non-linear and beside the z-shrinkage, slices suffer additional dilation in xy plane. Therefore, the error that is produced by the shrinkage artefact is not compensable with a simple linear correction approach.

1.4. Discussion

When classifying and describing neurons, three main points should be outlined: their electrophysiological behavior, their morphological structure and their molecular features/protein markers (Ascoli *et al.*, 2008). Here, it was demonstrated that the above-described neuroanatomical methods can be used for accurate morphological and molecular marker/protein expression analyses. However, one artefact counteracts precise morphological analyses as it produces a non-compensable error: Reduction of slice thickness along the z-axis (z-shrinkage) due to conventional embedding techniques with coverslips. To substantially minimize this artefact and errors it incurs, a new approach to embed acute slices by using the metal spacer system was provided.

Immunofluorescence and intracellular labeling combined with confocal microscopy in anatomical studies of neurons

Molecular features, such as protein expression, and morphological analyses are basics of investigations and classifications of neurons (Ascoli *et al.*, 2008). For the first, immunofluorescence labeling combined with confocal microscopy could be performed. For the latter, intracellular biocytin-staining during patch-clamp recordings is combined with confocal microscopy. Especially the confocal microscopy is a major advance in performing anatomical studies. By single point illumination and rejection of out-of-focus light, confocal microscopy provides high-resolution images with a precise 3D localization and good contrast (Semwogerere & Weeks, 2005). Although these techniques are in use for a while (Booker *et al.*, 2014; Kuster *et al.*, 2015;

Swietek *et al.*, 2016), they are still the most common approach to discover new anatomical insights of neurons.

Synaptosomal-associated protein of 47kDa (SNAP47), unlike other members of the SNAP family, does not contribute directly to exocytosis of neurotransmitter and synaptic vesicle recycling but rather plays a crucial role in intracellular vesicle trafficking and fusion events (Kuster *et al.*, 2015) and is also involved in the release of brain-derived neurotrophic factor (Shimojo *et al.*, 2015). However, little is known about its precise cellular localization in the hippocampus, especially in GABAergic interneurons. Here, we used immunofluorescence labeling and confocal microscopy for studying the cellular distribution of SNAP47 in mouse and rat hippocampus. Interestingly, we found a species specific distribution. In particular in GABAergic interneurons the difference in SNAP47 expression is very striking: Whereas interneurons in the mouse synthesize this SNAP isoform at high levels, interneurons in the rat showed only low levels of expression. Immunofluorescence labeling was supplemented with in situ hybridization of SNAP47 RNA to confirm that the results from the immunolabeling indeed correspond to endogenous protein production (Munster-Wandowski *et al.*, 2017). Hence, trafficking and storage of the SNAP47 protein exhibit species-dependent mechanisms. Nevertheless, it needs further studies to determine the precise subcellular localization and the functional role of the SNAP47 protein.

By using intracellular biocytin staining and confocal microscopy, we furthermore imaged and reconstructed human layer 2/3 pyramidal neurons. As these reconstructions were the basis of following computational approaches to model the activity of these neurons, it was relevant to achieve accurate morphological reconstructions and anatomical parameters (Gidon *et al.*, 2020). Therefore, interfering artefacts should be recognized and minimized.

Z-Shrinkage of acute slices after conventional embedding approaches

One major interfering artifact in histological work is the reduction in thickness of slices along the z-axis (z-shrinkage) due to the embedding. We investigated the time course of shrinkage and found that conventional embedded slices without any spacer already shrunk directly after embedding. The shrinking process continued with a decelerating speed and reached almost a steady state beyond two months after

embedding. Adhesive forces and the gravity of the cover slip are most likely responsible for this shrinkage.

Agar spacers, which were used in some previous studies to prevent shrinkage (Booker *et al.*, 2014; Degro *et al.*, 2015), can avoid the initial shrinkage directly after embedding, but do not prevent shrinkage for the long term. They even promote the shrinking process. Thus, two months post-embedding, the slice thickness reached a steady state that was even below the one of conventional embedded slices without any spacer. The reason for that could be a water loss and shrinkage of the agar spacer over time causing additional adhesive forces onto the slice.

Z-shrinkage leads to a non-compensable error in anatomical parameters

If z-shrinkage was recognized, usually a linear correction factor was employed to compensate for this artefact (Pyapali *et al.*, 1998; Hellwig, 2000; Marx *et al.*, 2012). In order to compensate correctly, this would require a uniform shrinking process and the absence of alterations in xy plane. However, the impact of shrinkage on anatomical parameters has not been studied yet and it has never been proven whether the usually used compensation is adequate.

We examined the impact of z-shrinkage on the morphology of neurons and its dendritic length by imaging the same cell twice, minimally shrunken and shrunken. Thereby, we demonstrated that z-shrinkage leads to a reduction of the total dendritic length. This error was not compensable with the application of linear correction factors.

Two reasons are responsible for this: First, a dilation in xy plane, which occurred due to the embedding with cover slip and second, a non-uniform shrinking process along the z-axis, whereby the degree of shrinkage is different in distinct depths of the slice. In fact, it has been previously described that a non-linear shrinking process occurred after embedding slices with conventional techniques (Egger *et al.*, 2008): They found a strong shrinkage at the slices margins and a moderate one in the center of the slice, according to our results. The reason for this could be a damage to cells during slicing procedure and a washout of cells and cell debris in the marginal/superficial portions of the slice. This causes an increased compressibility in these slice portions, which leads to a stronger z-shrinkage here. The metal spacer system can avoid the compression of slices and can thereby minimize the shrinkage artefact and the resulting non-compensable error in anatomical parameters.

The metal spacer system substantially minimizes but not fully prevent z-shrinkage

The metal spacer system can minimize the shrinkage degree to negligible values in the first time post-embedding but cannot totally prevent shrinkage in the long term. Ongoing collapsing of slices along the z-axis could be explained by the mounting medium. In fact, previous published studies argued that mounting media, also aqueous mounting media (but there is no data for our embedding medium Fluoromount), cause z-shrinkage (Claiborne *et al.*, 1986; Mainen *et al.*, 1996). These studies suggested 100% glycerol as preferential mounting medium, because it could prevent shrinkage. However, pure glycerol has several disadvantages: As it remains liquid, sealing of the slides is difficult and evaporation of the embedding medium is possible. Additionally, imaging with a microscope could be problematic as movements of the slice in its liquid embedding medium could occur. Finally, it has been reported that stained neurons tend to fade over some weeks if they are embedded in 100% glycerol (Jaeger, 2000). Hence, pure glycerol is not a suitable alternative.

In summary, the metal spacer system is a convenient embedding approach, which can substantially minimize z-shrinkage and the resulting non-compensable error in anatomical parameters, particularly in the first days after embedding. Thus, the metal spacer system improves the accuracy of morphological analyses.

1.5. References

- Allen Institute for Brain Science (2015) [Internet]. The Big Neuron Project [cited 2019 Nov 04]. Available from: <https://alleninstitute.org/bigneuron/about/>.
- Ascoli, G.A., Alonso-Nanclares, L., Anderson, S.A., Barrionuevo, G., Benavides-Piccione, R., Burkhalter, A., Buzsaki, G., Cauli, B., Defelipe, J., Fairen, A., Feldmeyer, D., Fishell, G., Fregnac, Y., Freund, T.F., Gardner, D., Gardner, E.P., Goldberg, J.H., Helmstaedter, M., Hestrin, S., Karube, F., Kisvarday, Z.F., Lambolez, B., Lewis, D.A., Marin, O., Markram, H., Munoz, A., Packer, A., Petersen, C.C., Rockland, K.S., Rossier, J., Rudy, B., Somogyi, P., Staiger, J.F., Tamas, G., Thomson, A.M., Toledo-Rodriguez, M., Wang, Y., West, D.C. & Yuste, R. (2008) Petilla terminology: nomenclature of features of GABAergic interneurons of the cerebral cortex. *Nat Rev Neurosci*, **9**, 557-568.
- Bolduan, F., Grosser, S. & Vida, I. (2020) Minimizing shrinkage of acute brain slices using metal spacers during histological embedding. *Brain Structure and Function*, **225**, 2577-2589.

- Booker, S.A., Song, J. & Vida, I. (2014) Whole-cell patch-clamp recordings from morphologically- and neurochemically-identified hippocampal interneurons. *J Vis Exp*, e51706.
- Cannon, R.C., Turner, D.A., Pyapali, G.K. & Wheal, H.V. (1998) An on-line archive of reconstructed hippocampal neurons. *J Neurosci Methods*, **84**, 49-54.
- Claiborne, B.J., Amaral, D.G. & Cowan, W.M. (1986) A light and electron microscopic analysis of the mossy fibers of the rat dentate gyrus. *J Comp Neurol*, **246**, 435-458.
- Degro, C.E., Kulik, A., Booker, S.A. & Vida, I. (2015) Compartmental distribution of GABAB receptor-mediated currents along the somatodendritic axis of hippocampal principal cells. *Front Synaptic Neurosci*, **7**, 6.
- Egger, V., Nevian, T. & Bruno, R.M. (2008) Subcolumnar dendritic and axonal organization of spiny stellate and star pyramid neurons within a barrel in rat somatosensory cortex. *Cereb Cortex*, **18**, 876-889.
- Feng, L., Zhao, T. & Kim, J. (2015) neuTube 1.0: A New Design for Efficient Neuron Reconstruction Software Based on the SWC Format. *eNeuro*, **2**.
- Gidon, A., Zolnik, T.A., Fidzinski, P., Bolduan, F., Papoutsi, A., Poirazi, P., Holtkamp, M., Vida, I. & Larkum, M.E. (2020) Dendritic action potentials and computation in human layer 2/3 cortical neurons. *Science*, **367**, 83-87.
- Hellwig, B. (2000) A quantitative analysis of the local connectivity between pyramidal neurons in layers 2/3 of the rat visual cortex. *Biol Cybern*, **82**, 111-121.
- Hines, M.L. & Carnevale, N.T. (1997) The NEURON simulation environment. *Neural Comput*, **9**, 1179-1209.
- Jaeger, D. (2000) Accurate reconstruction of neuronal morphology. *Computational neuroscience: Realistic Modeling for Experimentalists*, 159-178.
- Kuster, A., Nola, S., Dingli, F., Vacca, B., Gauchy, C., Beaujouan, J.C., Nunez, M., Moncion, T., Loew, D., Formstecher, E., Galli, T. & Proux-Gillardeaux, V. (2015) The Q-soluble N-Ethylmaleimide-sensitive Factor Attachment Protein Receptor (Q-SNARE) SNAP-47 Regulates Trafficking of Selected Vesicle-associated Membrane Proteins (VAMPs). *J Biol Chem*, **290**, 28056-28069.
- Longair, M.H., Baker, D.A. & Armstrong, J.D. (2011) Simple Neurite Tracer: open source software for reconstruction, visualization and analysis of neuronal processes. *Bioinformatics*, **27**, 2453-2454.
- Mainen, Z.F., Carnevale, N.T., Zador, A.M., Claiborne, B.J. & Brown, T.H. (1996) Electrotonic architecture of hippocampal CA1 pyramidal neurons based on three-dimensional reconstructions. *J Neurophysiol*, **76**, 1904-1923.
- Marx, M., Gunter, R.H., Hucko, W., Radnikow, G. & Feldmeyer, D. (2012) Improved biocytin labeling and neuronal 3D reconstruction. *Nat Protoc*, **7**, 394-407.
- Matsuzaki, M., Honkura, N., Ellis-Davies, G.C.R. & Kasai, H. (2004) Structural basis of long-term potentiation in single dendritic spines. *Nature*, **429**, 761-766.
- Minsky, M. (1988) Memoir on inventing the confocal scanning microscope. *Scanning*, **10**, 128-138.

- Munster-Wandowski, A., Heilmann, H., Bolduan, F., Trimbuch, T., Yanagawa, Y. & Vida, I. (2017) Distinct Localization of SNAP47 Protein in GABAergic and Glutamatergic Neurons in the Mouse and the Rat Hippocampus. *Front Neuroanat*, **11**, 56.
- Preibisch, S., Saalfeld, S. & Tomancak, P. (2009) Globally optimal stitching of tiled 3D microscopic image acquisitions. *Bioinformatics*, **25**, 1463-1465.
- Pyapali, G.K., Sik, A., Penttonen, M., Buzsaki, G. & Turner, D.A. (1998) Dendritic properties of hippocampal CA1 pyramidal neurons in the rat: intracellular staining in vivo and in vitro. *J Comp Neurol*, **391**, 335-352.
- Ramón y Cajal, S. (1909, 1911) *Histologie du Système Nerveux de l'Homme et des Vertébrés*, Maloine, Paris, France.
- Schindelin, J., Arganda-Carreras, I., Frise, E., Kaynig, V., Longair, M., Pietzsch, T., Preibisch, S., Rueden, C., Saalfeld, S., Schmid, B., Tinevez, J.Y., White, D.J., Hartenstein, V., Eliceiri, K., Tomancak, P. & Cardona, A. (2012) Fiji: an open-source platform for biological-image analysis. *Nat Methods*, **9**, 676-682.
- Semwogerere, D. & Weeks, E.R. (2005) Confocal microscopy. *Encyclopedia of biomaterials and biomedical engineering*, **23**, 1-10.
- Shen, H. (2015) Neuron encyclopaedia fires up to reveal brain secrets. *Nature*, **520**, 13-14.
- Shimojo, M., Courchet, J., Pieraut, S., Torabi-Rander, N., Sando, R., 3rd, Polleux, F. & Maximov, A. (2015) SNAREs Controlling Vesicular Release of BDNF and Development of Callosal Axons. *Cell reports*, **11**, 1054-1066.
- Swietek, B., Gupta, A., Proddutur, A. & Santhakumar, V. (2016) Immunostaining of Biocytin-filled and Processed Sections for Neurochemical Markers. *J Vis Exp*.
- Traub, R.D., Jefferys, J.G., Miles, R., Whittington, M.A. & Tóth, K. (1994) A branching dendritic model of a rodent CA3 pyramidal neurone. *J Physiol*, **481 (Pt 1)**, 79-95.
- Uematsu, M., Hirai, Y., Karube, F., Ebihara, S., Kato, M., Abe, K., Obata, K., Yoshida, S., Hirabayashi, M., Yanagawa, Y. & Kawaguchi, Y. (2007) Quantitative Chemical Composition of Cortical GABAergic Neurons Revealed in Transgenic Venus-Expressing Rats. *Cerebral Cortex*, **18**, 315-330.

2. Anteilserklärung / eidesstattliche Versicherung

„Ich, Felix Johannes Bolduan, versichere an Eides statt durch meine eigenhändige Unterschrift, dass ich die vorgelegte Dissertation mit dem Thema: „Improved Morphological Characterisation of Cortical Neurons“ / „Verbesserte Morphologische Charakterisierung kortikaler Neurone“ selbstständig und ohne nicht offengelegte Hilfe Dritter verfasst und keine anderen als die angegebenen Quellen und Hilfsmittel genutzt habe.

Alle Stellen, die wörtlich oder dem Sinne nach auf Publikationen oder Vorträgen anderer Autoren/innen beruhen, sind als solche in korrekter Zitierung kenntlich gemacht. Die Abschnitte zu Methodik (insbesondere praktische Arbeiten, Laborbestimmungen, statistische Aufarbeitung) und Resultaten (insbesondere Abbildungen, Graphiken und Tabellen) werden von mir verantwortet.

Meine Anteile an etwaigen Publikationen zu dieser Dissertation entsprechen denen, die in der untenstehenden gemeinsamen Erklärung mit dem/der Erstbetreuer/in, angegeben sind. Für sämtliche im Rahmen der Dissertation entstandenen Publikationen wurden die Richtlinien des ICMJE (International Committee of Medical Journal Editors; www.icmje.org) zur Autorenschaft eingehalten. Ich erkläre ferner, dass ich mich zur Einhaltung der Satzung der Charité – Universitätsmedizin Berlin zur Sicherung Guter Wissenschaftlicher Praxis verpflichte.

Weiterhin versichere ich, dass ich diese Dissertation weder in gleicher noch in ähnlicher Form bereits an einer anderen Fakultät eingereicht habe.

Die Bedeutung dieser eidesstattlichen Versicherung und die strafrechtlichen Folgen einer unwahren eidesstattlichen Versicherung (§§156, 161 des Strafgesetzbuches) sind mir bekannt und bewusst.“

Datum

Unterschrift

Anteilserklärung an den erfolgten Publikationen

Felix Johannes Bolduan hatte folgenden Anteil an den folgenden Publikationen:

Publikation 1: Münster-Wandowski A, Heilmann H, Bolduan F, Trimbuch T, Yanagawa Y, Vida I. Distinct Localization of SNAP47 Protein in GABAergic and Glutamatergic Neurons in the Mouse and the Rat Hippocampus. Front Neuroanat. 2017.

Beitrag im Einzelnen: Durchführung der konfokalen Mikroskopie zur Gewinnung der Abbildungen der immunhistochemisch gefärbten Nervenzellen (beispielsweise Figure 4 + 5). Auch die Quantifizierung der Immunfluoreszenz erfolgte durch Felix Bolduan (Figure 6). Felix Bolduan beteiligte sich am Korrekturlesen und Modifizieren des gesamten, präfinalen Manuskripts.

Publikation 2: Gidon A, Zolnik TA, Fidzinski P, Bolduan F, Papoutsis A, Poirazi P, Holtkamp M, Vida I, Larkum ME. Dendritic action potentials and computation in human layer 2/3 cortical neurons. Science. 2020.

Beitrag im Einzelnen: Die morphologischen Analysen, welche den Patch-Clamp-Recordings und entsprechenden immunhistochemischen Färbungen folgen, wurde allesamt von Felix Bolduan durchgeführt. Dies umfasst das konfokale Mikroskopieren von 51 menschlichen Gehirnschnitten, welche insgesamt 87 Pyramidenzellen enthielten. Von diesen wurden des Weiteren 12 vollständig rekonstruiert und für entsprechende Abbildungen und folgende Computational Models zugänglich gemacht (vgl. Figure 1A, 2A, 3A, S1A, S2A und S11A1). Auch der Methodenabschnitt „Visualization of biocytin-filled neurons“ und „Confocal imaging and reconstruction of neurons“ wurde von Felix Bolduan geschrieben und im Anschluss von Imre Vida angepasst. Felix Bolduan hat das gesamte Manuskript mit den anderen Autoren Korrektur gelesen und modifiziert.

Publikation 3: Bolduan F, Grosser S, Vida I. Minimizing shrinkage of acute brain slices using metal spacers during histological embedding. Brain Struct Funct. 2020.

Beitrag im Einzelnen: Sämtliche Experimente des Papers (von der Präparation der Gehirne über das Durchführen der Patch-Clamp-Recordings mit intrazellulärem Füllen der Neurone, den histologischen

Prozeduren mit immunhistochemischer Färbung, dem konfokalen Mikroskopieren und dem Rekonstruieren der Nervenzellen), wie auch sämtliche (statistischen) Auswertungen wurden von Felix Bolduan durchgeführt. Lediglich bei den Präparationen, Patch-clamp-recordings und bei den Auswertungen zur dendritischen „Spine“-Dichte unterstützte Sabine Grosser und bei den immunhistochemischen Färbungen unterstützte teilweise Ina Wolter. Alle Figuren und das komplette Manuskript wurden von Felix Bolduan erstellt. Modifizierungen fanden durch die beiden Ko-Autoren statt.

Unterschrift, Datum und Stempel des erstbetreuenden Hochschullehrers

Unterschrift des Doktoranden

3. Selected papers

3.1. Minimizing shrinkage of acute brain slices using metal spacers during histological embedding

Brain Structure and Function (2020) 225:2577–2589
<https://doi.org/10.1007/s00429-020-02141-3>

METHODS PAPER



Minimizing shrinkage of acute brain slices using metal spacers during histological embedding

Felix Bolduan¹ · Sabine Grosser¹ · Imre Vida¹

Received: 9 April 2020 / Accepted: 2 September 2020 / Published online: 12 September 2020
© The Author(s) 2020

Abstract

The morphological structure of neurons provides the basis for their functions and is a major focus of contemporary neuroscience studies. Intracellular staining of single cells in acute slices is a well-established approach, offering high-resolution information on neuronal morphology, complementing their physiology. Despite major technical advances, however, a common histological artifact often precludes precise morphological analysis: shrinkage of the sampled tissue after embedding for microscopy. Here, we describe a new approach using a metal spacer, sandwiched between two coverslips to reduce shrinkage of whole-mount slice preparations during embedding with aqueous mounting medium under a coverslip. This approach additionally allows imaging the slices from both sides to obtain better quality images of deeper structures. We demonstrate that the use of this spacer system can efficiently and stably reduce the shrinkage of slices, whereas conventional embedding methods without spacer or with agar spacer cause severe, progressive shrinkage after embedding. We further show that the shrinkage of slices is not uniform and artifacts in morphology and anatomical parameters produced cannot be compensated using linear correction algorithms. Our study, thus, emphasizes the importance of preventing the deformation of slice preparations and offers an effective means for reducing shrinkage and associated artifacts during embedding.

Keywords Acute brain slice · Single cell morphology · Biocytin labeling · Histology · Tissue shrinkage · Confocal imaging

Introduction

The morphology of neurons provides the structural framework for their functions, including the integration of synaptic inputs and the generation of action potentials (Kasper et al. 1994; Norenberg et al. 2010; DeFelipe et al. 2013; de Sousa et al. 2015; Gullledge and Bravo, 2016; Mihaljevic et al. 2018). Indeed, from Cajal's morphological studies of Golgi stained neurons (Ramón y Cajal 1909, 1911) up to today's high-resolution confocal images of genetically identified and biocytin stained neurons (Bartos et al. 2002; Thomson and Armstrong 2011; Booker et al. 2014), anatomical investigations offered important insights for the

understanding of the physiological and circuit functions of neurons and also provided essential data for computational analysis (Traub et al. 1994; Major et al. 1994; Norenberg et al. 2010; Gidon et al. 2020). While identification, labeling and imaging of neurons have shown substantial advances in recent decades, a major technical problem of morphological analysis remains: the shrinkage of tissue during histological processing and embedding.

Processing of tissue sections or acute slice material by applying conventional methods leads to a strong reduction in their overall dimensions, in particular, in their thickness along the 'z-axis' (the axis perpendicular to the cut surfaces of the slice or section). This deformation of the tissue has a substantial impact on the morphology of the neurons observed under the microscope and, consequently, also on their reconstructions and derived anatomical parameters. In fact, z-shrinkage has been previously recognized and found to be highly dependent on the histological processing and embedding: histological procedures which include drying or dehydration of the tissue cause severe shrinkage (Pyapali et al. 1998; Hellwig 2000; Marx et al. 2012). Avoiding such steps in the processing and the use of aqueous mounting

Electronic supplementary material The online version of this article (<https://doi.org/10.1007/s00429-020-02141-3>) contains supplementary material, which is available to authorized users.

✉ Imre Vida
imre.vida@charite.de

¹ Institute of Integrative Neuroanatomy, Charité - Universitätsmedizin Berlin, Berlin, Germany

media can help to eliminate shrinkage during processing; nevertheless the slices show shrinkage after they are embedded under a coverslip (Egger et al. 2008; Swietek et al. 2016).

To prevent this shrinkage, agar spacers between glass slide and coverslip were used in some studies (Booker et al. 2014; Degro et al. 2015). However, the long-term stability of this soft spacer has not been examined. In fact, the process of shrinkage in general has remained poorly characterized. Its precise degree and time course are not known as previous investigations examined only a single and often not well-defined time point (Pyapali et al. 1998; Egger et al. 2008). Furthermore, the impact of shrinkage on neuronal morphology and anatomical parameters are unknown: assuming a uniform, linear shrinkage, correction factors have been employed to three-dimensional (3D) reconstructions in some studies in order to compensate for the distortion effects (Pyapali et al. 1998; Hellwig 2000; Degro et al. 2015). However, there is no evidence that such compensation is, indeed, an adequate approach for shrinkage correction.

Here, we describe a new approach using a metal spacer to minimize tissue shrinkage in fixed brain slices. By comparing embedding with metal spacers to other commonly used methods we demonstrate that metal spacers markedly reduce tissue shrinkage over time. Our analysis further reveals that z-shrinkage during conventional embedding produces non-uniform distortions in the slices and neuronal morphology, which cannot be adequately compensated by common linear methods. Thus, prevention of tissue shrinkage is essential in minimizing measurement errors in anatomical parameters in mounted slices.

Methods

Slice preparation

Experiments and animal maintenance were performed in accordance with local (LaGeSo, Berlin, T 0215/11), national (German Animal Welfare Act) and international guidelines (EU Directive 2010/63/EU). For obtaining whole-cell recordings and examining the shrinkage of acute brain slices, rat hippocampal slices were made and processed as previously described (Booker et al. 2014). In brief, brains were quickly dissected from decapitated rats (male and female Wistar-VGAT-Venus-A rats, P21–P25) after deep isofluran anesthesia (3%) and were put into carbogenated (95% O₂/5% CO₂), semi-frozen, sucrose-based artificial cerebrospinal fluid (sACSF, in mM: 87 NaCl, 2.5 KCl, 25 NaHCO₃, 1.25 NaH₂PO₄, 25 Glucose, 75 Sucrose, 1 Na₂-Pyruvate, 1 Na₂-Ascorbate, 7 MgCl₂, 0.5 CaCl₂). Horizontal slices (300 μm) were subsequently cut from the hippocampal formation using a vibratome (VT1200s, Leica, Germany). The

slices were transferred to carbogenated sACSF (34 °C) and left there for 30 min to recover. Afterwards, the slices were stored at room temperature in sACSF until further procedures. For analysis of shrinkage, slices were directly fixed with 4% paraformaldehyde (PFA) in 0.1 M phosphate buffer (PB) overnight at 4 °C.

Whole-cell recording, intracellular filling and visualization of neurons

To examine the impact of shrinkage on neuronal morphology, whole-cell patch-clamp recordings were performed in combination with intracellular filling in a submerged recording chamber, perfused with carbogenated artificial cerebrospinal fluid (ACSF, in mM: 125 NaCl, 2.5 KCl, 25 NaHCO₃, 1.25 NaH₂PO₄, 25 Glucose, 1 Na₂-Pyruvate, 1 Na₂-Ascorbate, 1 MgCl₂, 2 CaCl₂) at a temperature of about 32 °C. Subicular pyramidal cells were visualized using an upright microscope (BX-51WI, Olympus, Hamburg, Germany) equipped with a digital camera (Zyla 5.5 sCMOS, Andor—Oxford Instruments, Abingdon, UK). Recordings were performed using a Multiclamp 700B amplifier (Molecular Devices, San Jose, CA). Patch pipettes were pulled from borosilicate glass capillaries (2 mm outer/1 mm inner diameter, Hilgenberg, Germany) on a horizontal electrode puller (P-97, Sutter Instruments, Novato, CA) and filled with an intracellular solution (in mM: 130 k-gluconate, 10 KCl, 2 MgCl₂, 10 EGTA, 10 HEPES, 2 Na₂-ATP, 0.3 Na₂-GTP, 1 Na₂-creatinine, and 0.1% Biocytin; 290–310 mOsm). A whole-cell recording was performed for at least 16 min to ensure sufficient diffusion of the biocytin and filling the cell's somato-dendritic domain (Marx et al. 2012).

At the end of the recording, the pipette was carefully removed from the cell to form an outside-out patch and the slice instantly transferred to a 4% PFA containing 0.1 M PB based solution. After overnight fixation at 4 °C, slices were repeatedly rinsed in PB for at least 1 h and incubated with AlexaFlour 647-conjugated streptavidin (1:1000, Invitrogen, Eugene, OR) diluted in 0.1 M PB containing 0.05% Na₃N and 0.5% Triton-X overnight at 4 °C. The slices were subsequently rinsed repeatedly in PB before embedding.

Embedding procedures for acute slices

Slices were embedded in a solidifying aqueous mounting medium (Fluoromount-G, Southern Biotech, Birmingham, AL) using three different approaches:

- (1) For the conventional embedding method, the slices were mounted on a standard glass slide without any spacer and a coverslip placed on top. Care was taken to mount the slices with the recorded neurons (i.e. their somata) closer the upper surface when placed on the

- glass slides. Finally, coverslips were sealed with nail polish.
- (2) To prevent shrinkage of the mounted slice, the conventional embedding procedure was modified by adding a 300 μm thick agar spacer between slide and coverslip (Booker et al. 2014; Degro et al. 2015). To produce these spacers, agar (4%; Formedium Ltd, Hunstanton, UK) was diluted in 0.1 M PB and heated up to 90 $^{\circ}\text{C}$. After cooling down, a solid block was formed, which was cut to the size of the coverslips (24 \times 24 mm) and sectioned at 300 μm on a vibratome. Finally, a round hole with a diameter of 8 mm was stamped into the middle of the spacers. The spacers were collected and stored in 0.1 M PB until usage to prevent them from drying out.
 - (3) In the new embedding approach, the agar spacer was replaced by a 300 μm thick metal spacer (Fig. 1). The metal spacer was made of stainless steel and had rectangular form with measures also defined by the coverslips, but exceeding those by a few millimeters in all directions (42 \times 26 mm) to enable a stable contact and sealing with nail polish. The spacer had a round hole with a diameter of 15 mm in their center. The spacers were sourced from a commercial provider for custom-made metal objects (wh Münzprüfer, Berlin, Germany). For the embedding, one coverslip was glued onto the metal spacer using cyanoacrylate (UHU, Bühl, Germany), serving as a bottom plate during the mounting. After mounting the slice in the aqueous mounting medium, a second coverslip was carefully placed on the top of the assembly, making sure that no air was trapped, and sealed with nail polish.

Confocal imaging, 3D reconstruction and morphological analysis of neurons

Imaging of neurons was performed using a laser scanning confocal microscope (FluoView FV1000, Olympus, Hamburg, Germany) with a 30 \times silicone oil-immersion objective (N.A. 1.05; Olympus). To image slices embedded with metal spacers on the microscope stage, a custom-made adapter (Fig. 1a) was obtained from the commercial provider (wh Münzprüfer). Image stacks were acquired at a xy -resolution of 1024 \times 1024 (2 μs pixel dwell time; pixel size: 0.414 μm) and 0.5 μm steps along the vertical z -axis. To improve imaging for deeper parts of the slices embedded with metal spacers, they were imaged first from the upper surface to the middle of the slice and subsequently from the bottom surface to the middle of the slice by flipping them in the adapter for the microscope stage. For selected neurons, high-resolution images of dendritic segments were performed using a 60 \times silicone oil-immersion objective (N.A. 1.3) at 2048 \times 2048 resolution (2 μs pixel dwell time; pixel

size: 0.207 μm) and 0.05 μm steps between imaging planes along the z -axis.

Obtained image stacks were registered and stitched using the ‘3D stitching’ plug-in (Preibisch et al. 2009) of the Fiji/ImageJ software package (<https://fiji.sc/>; Schindelin et al. 2012). 3D reconstructions were made from stitched image stacks using the ‘Simple neurite tracer’ plug-in (Longair et al. 2011) in Fiji or the Neutube software package (Feng et al. 2015). Reconstructed morphologies were stored as SWC files (Cannon et al. 1998).

Morphological analysis of the reconstructed neurons was performed in the NEURON software environment (Hines and Carnevale, 1997) using custom written ‘hoc’ scripts (Degro et al. 2015). Neuronal morphologies were imported using the ‘import3d’ tool package. To reduce the raggedness of reconstructed neuronal process trajectories, which is inherent to reconstructions made by the ‘Simple neurite tracer’ plug-in, in particular along the z -axis, a Gaussian spatial filter was applied (3-point window, single run in the xy -plane and 15 iterations for values along the z -axis). Z -shrinkage compensation was accomplished by using a correction factor applied to the z -coordinates of the reconstructed neuronal structure. The correction factor was determined by calculating the quotient of the original nominal thickness (300 μm) and the measured thickness of the shrunken slices.

Measurement of z-shrinkage of embedded slices

The thickness of the embedded slice was measured on the laser scanning confocal microscope (FluoView FV1000, Olympus) with an 30 \times objective. Boundaries of the slice could easily be identified due to the non-specific background fluorescence of the tissue. The table’s vertical travel between top and bottom views of the slice was measured and taken as the thickness (Dorph-Petersen et al. 2001). First measurements of slice thickness were made 3 h after embedding, followed by measurements at distinct time points for up to 2 months. The slice thickness was always measured in the same region, at the crest of the granular cell layer of the dentate gyrus. Shrinkage was calculated as the difference of the measured and the nominal thickness (300 μm) expressed as percentage of the nominal value.

Analysis of the impact of shrinkage on the intracellular filled neurons

To analyze the impact of shrinkage with the different embedding approaches, slices ($n = 6$) were first embedded with a metal spacer, and subsequently re-embedded following the conventional approach without a spacer. The slices were imaged 2–5 days after embedding with the metal spacer, to obtain a set of reference images and reconstructions of the neurons in this minimally shrunken state.

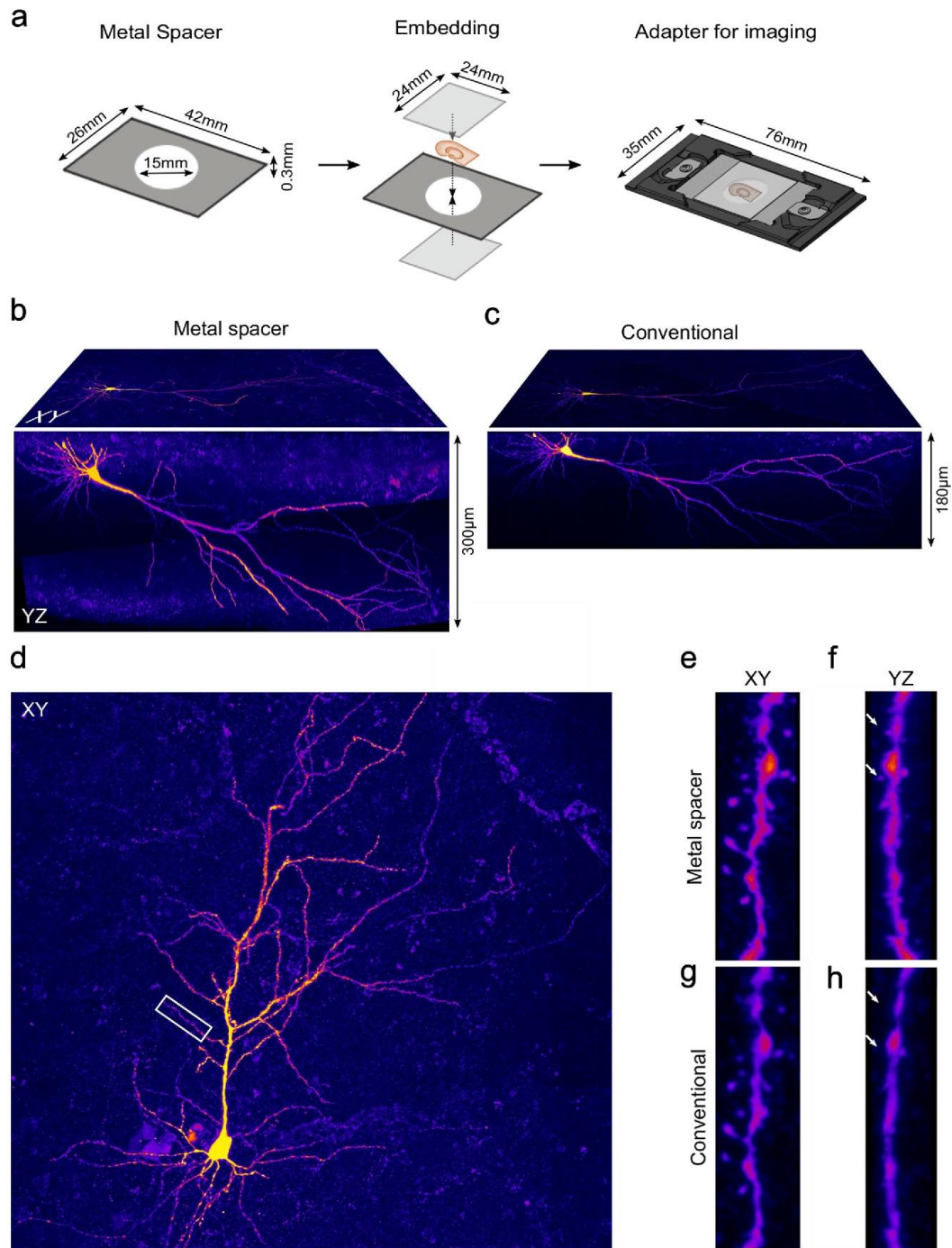


Fig. 1 Embedding of acute slices with the metal spacer system for light microscopic analysis minimizes shrinkage and improves image quality. **a** Schematic representation of the embedding process using the metal spacer system. The 300 μm thick metal spacer (left) and a fixed brain slice are sandwiched between two glass coverslips with a solidifying aqueous mounting medium (middle). A custom-made adapter is required for imaging the embedded slices (right). **b, c** Orthogonal projections of a full confocal image stack of a subicular pyramidal neuron onto the xy - (top surface) and the yz -planes (front surface) embedded with a metal spacer (**b**) and following the conventional embedding approach without a spacer (**c**). Note the substantial shrinkage and the weak signal in the deeper parts of the slice after conventional embedding. **d** Projection of the confocal image stack of another subicular pyramidal neuron onto the xy -plane embedded with a metal spacer. **e–h** High-resolution images of a dendritic segment (rectangle in **d**) embedded first with the metal spacer (**e, f**) and after re-embedding following the conventional approach without a spacer (**g, h**) viewed in xy - (**e, g**) and in yz -projections (**f, h**). The image in panel **h** was compensated for shrinkage for better comparison with panel **f**. Note the reduced detail of the contours of the dendrite and the absence of some spines (arrows in **h** and **g**) in the yz -plane after conventional embedding

The second imaging session was performed 11–14 days after re-embedding without spacer, to obtain images and reconstructions in a strongly shrunken state. Comparative dendritic length measurements were made with and without linear compensation for shrinkage (Degro et al. 2015), performed on the reconstructed neurons in the NEURON software package (see above).

To assess the effect of embedding on the slices in the xy -plane, the z -values of the 3D neuronal structures were set to zero and the total dendritic lengths of the flattened neurons were determined for the two conditions. To directly measure dimensional changes in xy -plane, photomicrographs of slices ($n = 4$) were made in the recording chamber at day 4 after embedding with the metal spacer and subsequently 14 days after re-embedding the slices without a spacer. Measurements of distances between selected landmarks in the plane of the slices were made in these sets of photomicrographs and the changes in distances normalized to their values obtained in the recording chamber. Additionally, lengths of dendritic segments projected in xy -plane were measured and compared for the two embedding conditions: with metal spacer and after re-embedding without spacer.

To assess if shrinkage was uniform along the z -axis in the slices, pairs of image stacks were analyzed. Projections of the two sets of image stacks were made in the yz -plane and the z -dimension of corresponding dendritic segments measured in the upper, the middle and the lower thirds of the slices. The difference of the two measurements, normalized to the value of the first measurement, was taken as the degree of differential shrinkage. As slices embedded with the metal spacer showed a small ($\leq 4\%$), but consistent shrinkage along the z -axis at the time point of the imaging, the values calculated are underestimates of the full scale

of shrinkage. In view of the large difference, however, we consider these estimates as representative for the process.

Statistics

Statistical analysis was performed using Graphpad Prism version 7 (GraphPad Software, San Diego, CA). Time series of slice thickness for the different embedding methods were compared with a two-way ANOVA for repeated measures. Comparisons of slice thickness for the three conditions at given time points as well as the degree of shrinkage in distinct depths of the slices were made using one-way analyses of variance (ANOVA) with Bonferroni correction for multiple comparisons. Paired data were compared with Wilcoxon signed rank tests. Values are indicated as mean \pm SD throughout. Statistical significance was assumed if $p < 0.05$.

Results

Description of the metal spacer system

To minimize shrinkage along the z -axis of acute slices after embedding, we developed a method using a metal spacer (Fig. 1). The metal spacer had a thickness equal to that of the slices (nominal 300 μm) typically used in electrophysiological recordings and had a rectangular shape (42×26 mm), exceeding slightly the size of the coverslips (24×24 mm) (Fig. 1a). To provide sufficient space for mounting slices, we opted for a large, central round opening (15 mm). We chose a spacer design that permits slices to be mounted between two coverslips of high optical quality, rather than between a single coverslip and glass slide, which is the current standard. This design requires a special adapter for imaging on a regular microscope stage, but enables imaging of the embedded slice from both sides (Fig. 1a). Thus, a better signal can be achieved in the depth and imaging of the full extent of the slice is possible when using objectives with short working distances by flipping the slices embedded with the metal spacer in the adapter.

Indeed, slices embedded using the metal spacer preserved their thickness well and showed a higher intensity of labeled structures (e.g. dendrites) and a better signal to noise ratio in their bottom halves when imaged from both sides (Fig. 1b) in comparison to the image stacks made 10–14 days after re-mounting the slices conventionally on a commonly used glass slide without a spacer imaged from the top (Fig. 1c). Images of dendritic segments in slices embedded with the metal spacer also captured more detail of their morphology when compared to image stacks made after re-embedding with the conventional approach (Fig. 1d–h). While differences between the pairs of image sets were not prominent in the xy -plane (Fig. 1e, g), they were very obvious in side

views, e.g. in projections onto the yz -plane, revealing more detail of the contours of dendrites and more spines above and below the dendritic segments with the metal spacer (Fig. 1f) than after re-embedding without a spacer (Fig. 1h). In fact, counting the number of spines on dendritic segments and calculating their density in projection onto the xy -plane delivered matching results for the two embedding states ($0.85 \pm 0.17 \mu\text{m}^{-1}$, vs. $0.8 \pm 0.12 \mu\text{m}^{-1}$, 8 dendritic segments, for metal spacer and conventional embedding, respectively, $p=0.312$, Wilcoxon signed rank test, Online Resource 1a, b), whereas the estimated density was markedly lower in projections onto the yz -plane with the conventional embedding ($0.41 \pm 0.18 \mu\text{m}^{-1}$) than with the metal spacer ($0.62 \pm 0.14 \mu\text{m}^{-1}$, $p=0.016$, Wilcoxon signed rank test, Online Resource 1c,d). Convergently, when applying a 3-d counting approach in the corresponding image stacks, the spine density was underestimated by 16% in slices

embedded with the conventional method ($1.25 \pm 0.19 \mu\text{m}^{-1}$ vs. $1.05 \pm 0.16 \mu\text{m}^{-1}$, respectively, $p=0.0078$, Wilcoxon signed rank test, Online Resource 1e), indicating that shrinkage-induced reduction in physical resolution along the optical axis can result in underestimates of spine densities in slices with conventional embedding.

The metal spacer can minimize the shrinkage of embedded slices

To evaluate the long-term effectiveness of the metal spacer for preventing slice shrinkage, we next assessed the time course of changes in the thickness of acute slices (nominal 300 μm) embedded in a solidifying aqueous mounting medium using three different approaches (Fig. 2a): (1) without any spacer on a regular glass slide with a coverslip (conventional method), (2) a modified version using a

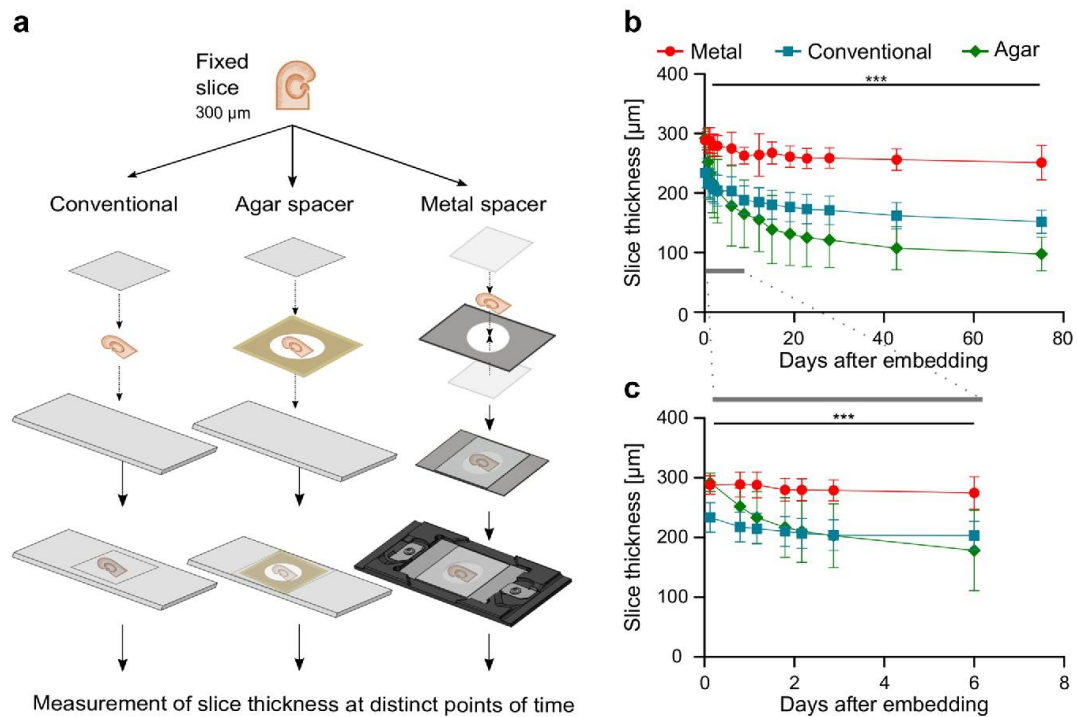


Fig. 2 The rapid and strong shrinkage of fixed brain slices observed after conventional embedding is minimized by the metal spacer. **a** Schematic representation of the embedding of the acute slices using three alternative approaches: (1) conventional embedding method without any spacer on a normal glass slide with a coverslip (left arm), (2) a modified version using a 300 μm thick agar spacer between slide and coverslip (middle), and (3) using the metal spacer (right). **b** Summary graph of the average slice thickness plotted over time after embedding with the metal spacer (red circles, 8 slices), follow-

ing the conventional approach without spacer (blue squares, $n=11$), and with the agar spacer (green diamonds, $n=14$). **c** The plot shows the same data at higher temporal resolution for the first 6 days (gray bar in **b**). Note, that the agar spacer initially prevents shrinkage of the slices, however, the thickness of these specimens rapidly decreases and declines below that of the slices without a spacer already beyond 3 days. Error bars indicate standard deviation; statistical significance: *** $p < 0.001$

300 μm thick agar spacer between slide and coverslip, and (3) using the 300 μm thick metal spacer system. The first measurements of slice thickness were performed on a confocal microscope three hours after embedding (Fig. 2b). Slices embedded without spacer ($n=11$) shrunk substantially by about $22.1 \pm 8.1\%$ in their thickness already at this early time point. In contrast, slices with metal ($n=8$) or agar spacer ($n=14$) showed only minimal shrinkage of $3.9 \pm 4.8\%$ and $2.6 \pm 5.0\%$ along the z -axis, respectively ($p < 0.0001$, ANOVA with Bonferroni correction for multiple comparisons). Thus, there is strong reduction in the thickness of the slices taking place in the first hours after embedding using the conventional approach, but both types of spacer are effective in minimizing this initial shrinking.

The shrinking process of the conventionally embedded slices continued in the following days and weeks, albeit at a progressively decelerating rate and approached asymptotic levels beyond 2 months (Fig. 2b). The thickness of the slices was found to be reduced by $49.4 \pm 6.1\%$ when measured 75 days after embedding (Fig. 2b). Slices embedded with the spacers also continued to shrink, but depending on the type, they showed highly divergent temporal dynamics and reached different asymptotic levels. Slices embedded with the metal spacer shrunk slowly and moderately, losing only $16.3 \pm 8.9\%$ of their thickness when measured after 75 days (Fig. 2b). In contrast, slices with agar spacer showed an accelerated and strong shrinkage, reaching a mean of $67.4 \pm 9.0\%$ by the same time point (Fig. 2b). In fact, although agar spacer could prevent the initial shrinkage, the reduction in the thickness of those slices progressed very rapidly in the first days (Fig. 2c) and was equal to that of conventional embedded slices already at day 3 ($32.2 \pm 17.1\%$ vs. $31.9 \pm 8.1\%$) and exceeded that by day 6 post-embedding ($40.5 \pm 21.6\%$ vs. $32.1 \pm 7.4\%$). In comparison, slices embedded with metal spacer showed a z -shrinkage of only $8.4 \pm 8.5\%$ at day 6 post-embedding ($p = 0.0004$, ANOVA with Bonferroni correction for multiple comparisons, Fig. 2c).

In summary, the use of metal spacers can efficiently minimize shrinkage, offering a major improvement over conventional embedding methods. In contrast, while agar spacer can prevent the initial shrinkage during the first hours after embedding, they are not useful to minimize shrinkage on longer time scales and, in fact, strongly promote shrinkage beyond 1 week.

Shrinkage has an impact on reconstructed structure and anatomical parameters of labeled neurons

Prior morphological studies assumed a uniform slice shrinkage and used linear correction factors to compensate its impact on reconstructions (Pyapali et al. 1998; Hellwig, 2000; Marx et al. 2012). Therefore, we next addressed how

the morphology of filled neurons changes due to shrinkage and whether it was possible to compensate their deformation by applying a linear correction factor.

To obtain neuronal morphologies, we performed whole-cell patch-clamp recordings in combination with intracellular biocytin labeling of pyramidal cells in 300 μm thick acute hippocampal slices (Fig. 3). After histological processing and visualization of the neurons, the slices were embedded first with a metal spacer (Fig. 3a) and imaged on a confocal microscope within 2–5 days (Fig. 3b). Neuronal morphologies were reconstructed using the simple neurite tracer plug-in (Longair et al. 2011) in the Fiji software package (Fig. 3c). Subsequently, the slices were removed from the metal spacer system and re-embedded following the conventional approach without a spacer (Fig. 3a); 11–14 days after re-embedding, the neurons were imaged (Fig. 3d) and reconstructed anew (Fig. 3e). This way we obtained full image sets and reconstructions of the somato-dendritic domains of six pyramidal cells in a minimally shrunken state (embedded with metal spacer) and a strongly shrunken state (conventional embedding). Finally, to compensate for the difference in the shrinkage between the two embedding states, a linear correction factor was applied to the z -coordinates of the second reconstruction (Fig. 3f). The correction factor was calculated as the quotient of the measured thickness for each slice mounted with metal spacer and the corresponding value obtained after re-embedding without spacer.

When visually compared, there were no major differences when the pairs of image stacks or 3D-reconstructions were projected onto the xy -plane (i.e. viewed from the top surface of the slices). In contrast, the impact of shrinkage on dendritic morphology was very obvious when the stacks and reconstructions were projected onto the yz -plane (i.e. viewed from the side, Fig. 3b, c versus Fig. 3d, e). Consistent with the differential shrinkage described above, the thickness of the slices after re-embedding without spacer was reduced by $42.0 \pm 4.6\%$ relative to the values measured during the first embedding using the metal spacer.

To analyze the impact of z -shrinkage on anatomical parameters, the total dendritic length of the neurons was calculated and compared between the two reconstructions for each neuron. This comparison demonstrated that the total dendritic lengths were consistently lower by a factor of $5.7 \pm 1.2\%$ on average in the reconstructions obtained after the re-embedding ($p = 0.03$, Wilcoxon signed rank test, Fig. 3g, h), confirming that shrinkage causes an alteration in morphological parameters. However, this difference was not corrected well when we attempted to compensate for shrinkage in the second set of reconstructions by applying the linear correction factor to the z -coordinates. With this correction, the total dendritic lengths were consistently higher by $6.8 \pm 1.8\%$, than those obtained for

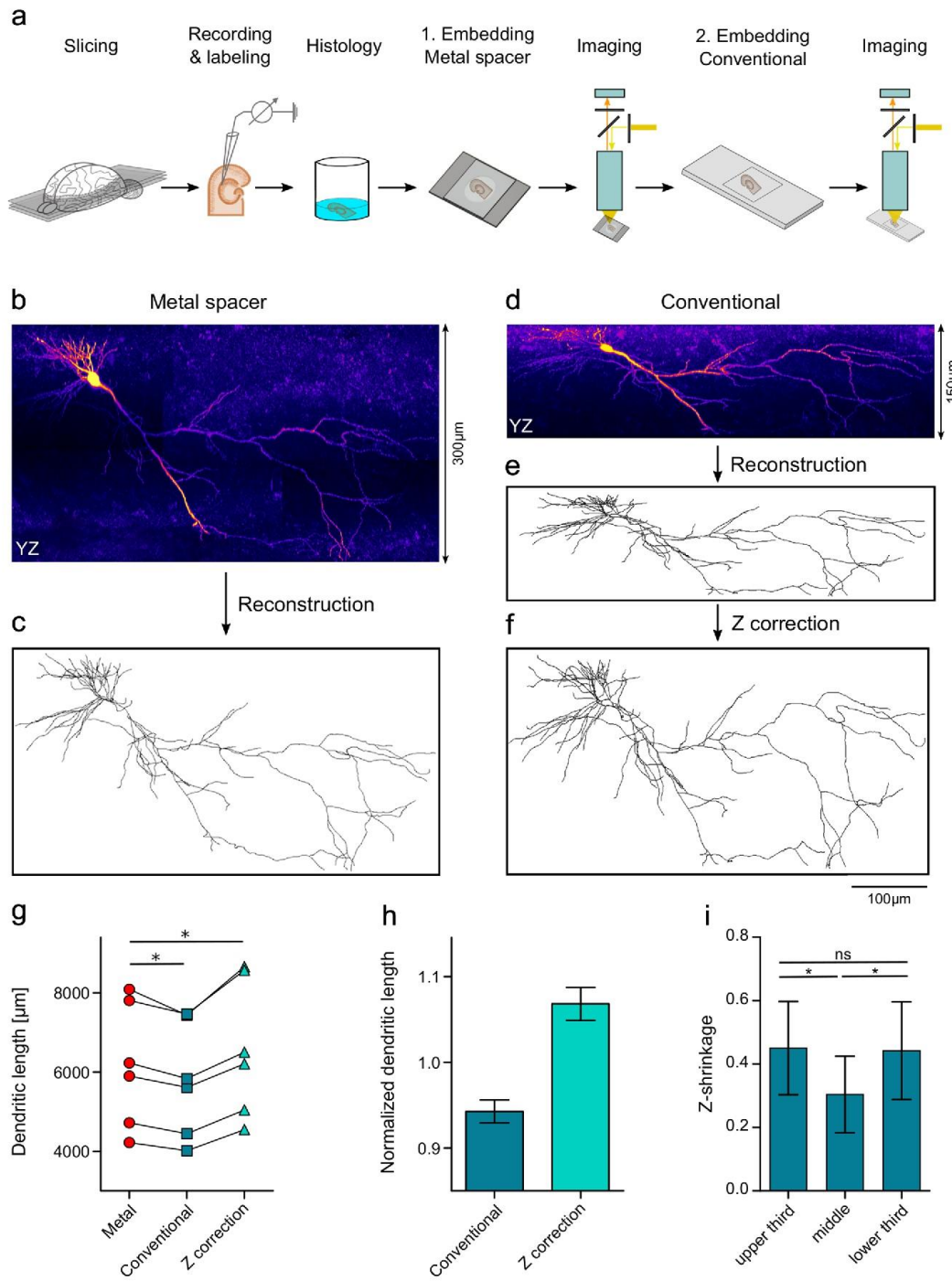


Fig. 3 The impact of shrinkage on the morphology of intracellularly labeled neurons. **a** Schematic representation of the procedure analyzing the impact of shrinkage on neuronal morphology, which includes a first embedding with a metal spacer followed by confocal imaging and a re-embedding without a spacer (**2. Embedding, Conventional**) and repetition of the confocal imaging with a delay of 11–14 days. **b–f** Morphological data of a representative pyramidal cell under the different embedding conditions. **yz**-Projections of the confocal image stacks obtained from the slice embedded with the metal spacer (**b**) and after re-embedding without spacer (**d**). Full 3D reconstructions of the neuron viewed in the **yz**-projection made from the image stacks with metal spacer (**c**) and without spacer (**e**), and the latter reconstruction after correction for shrinkage along the **z**-axis (**f**). **g** Plot of the total dendritic lengths of 6 neurons measured in reconstructions made with metal spacer (red circles), in reconstructions made after re-embedding without spacer (blue squares) and after linear shrinkage correction was applied to the second set of reconstructions (cyan triangles). Lines connect data points representing measurements from the same neuron. **h** Summary bar chart of the dendritic lengths measured in the reconstructions made after conventional embedding (blue bar) and after linear shrinkage correction was applied (cyan bar), normalized to the corresponding lengths measured in reconstructions with metal spacer. **i** Summary bar chart of the degree of shrinkage of dendritic segments in the vertical dimension (**z**-shrinkage) in the upper, middle and lower thirds of slices. Measurements of the **z**-dimension of dendritic segments (15 dendrites from 3 slices for each depth) were made in image stacks obtained after conventional embedding and normalized to the corresponding values measured with the metal spacer. Error bars indicate standard deviation; statistical significance: * $p < 0.05$

the first reconstructions with the metal spacer ($p = 0.03$; Wilcoxon signed rank test, Fig. 3g, h).

To test if the reconstruction algorithm was not introducing errors in this evaluation, we generated a second set of reconstructions from the same image stacks using Neutube as reconstruction software (Feng et al. 2015). The total dendritic lengths measured in these reconstructions (Online Resource 2) were slightly smaller than those in the reconstructions made in Fiji, plausibly due to the lower level of spatial noise produced along the dendritic axes by the algorithms used in Neutube (see “Methods”). Nevertheless, when the second reconstructions of the neurons, obtained from the conventional embedding, were compared with the first ones, obtained from embedding with metal spacer, the total dendritic lengths were found again to be consistently smaller by a factor of $5.5 \pm 1.3\%$ on average ($p = 0.03$, Wilcoxon signed rank test, Online Resource 2a, b). Furthermore, the total dendritic lengths from the corrected reconstructions exceeded the corresponding values with metal spacer by $7.8 \pm 2.0\%$ ($p = 0.03$, Wilcoxon signed rank test, Online Resource 2a, b). These findings convergently suggest that effects of shrinkage on the neuronal morphology cannot be properly compensated, plausibly, because the shrinkage is not uniform and/or the slices may suffer additional deformation during conventional embedding without a spacer.

Shrinkage is not uniform across the depth of the slices

To investigate these possibilities, we examined first if there was any evidence for a non-uniform shrinkage. We made measurements of dendritic segments, which were primarily oriented along the **z**-axis, in the two pairs of confocal image stacks obtained with the metal spacer and after re-embedding. For each slice, three sets of samples were collected corresponding to the upper, the middle and the lower third along the **z**-axis of the slices in order to estimate and compare the degree of shrinkage at different depths. Evaluation of these samples showed that the shrinkage was affecting the **z**-dimension of dendritic segments on average by $45.1 \pm 14.2\%$ in the top, $30.4 \pm 11.7\%$ in the middle, and $44.3 \pm 14.8\%$ in the bottom third of the slices ($p = 0.01$, ANOVA with Bonferroni correction for multiple comparisons, 15 dendritic segments in each sample from 3 slices, Fig. 3i). Thus, the shrinkage was found to be stronger closer to the upper and lower surfaces of the slices than in their middle. To further confirm this notion, we made additional measurements in the top and bottom 20% of the slices and found that shrinkage in these marginal zones of the slices reached $61.3 \pm 9.1\%$ (ten dendritic segments in the top or bottom 20% in two slices). These results clearly indicate a non-uniform, non-linear shrinkage of the slices along the **z**-axis, which renders linear compensation impossible.

Shrinkage is accompanied by a moderate dilation in the **xy**-plane of the slices

Next, we tested if the reconstructions showed evidence of deformation in the **xy**-plane. For this, we first projected all reconstructions into the **xy**-plane by setting all **z** values to zero, thus, reducing them from 3D to 2D ones. In these flattened reconstructions, we repeated the comparison of the 2D-dendritic lengths between the two consecutive reconstructions for each neuron. The comparison revealed that in the second reconstructions, made after the re-embedding with no spacer, the total 2D-dendritic lengths was consistently larger by a factor of $5.2 \pm 2.3\%$ on average than in the first ones ($p = 0.03$, Wilcoxon signed rank test, six neurons; Fig. 4a, b), suggesting that while the slices suffered a substantial shrinkage along the **z**-axis, they also showed a moderate dilation in the **xy**-plane after re-embedding with the conventional method.

To confirm this result, we made measurements of dendritic segments in the pairs of confocal image stacks and compared their **xy**-dimensions for the two embedding states: in the second set of image stacks with no spacer, the sampled dendritic segments had larger **xy**-dimensions when compared to their dimensions in the first set of image stacks made with the metal spacer by a factor of $8.2 \pm 6.1\%$ on average

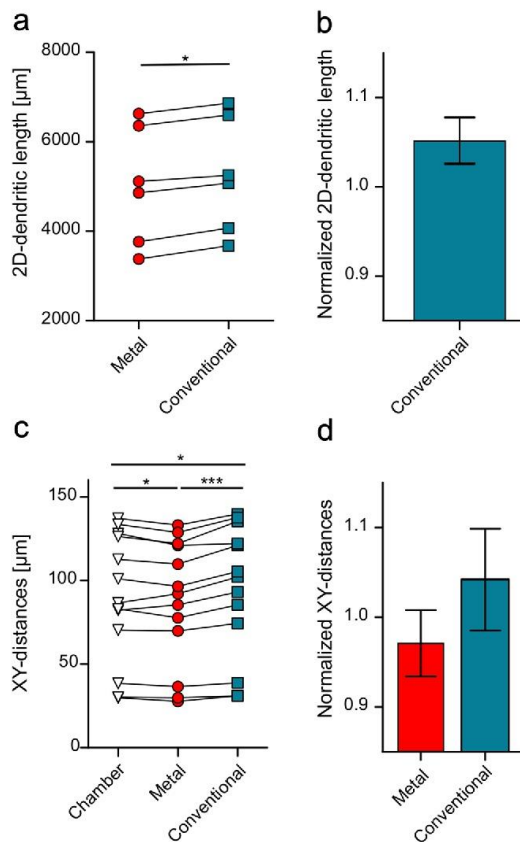


Fig. 4 Dimensional changes in the *xy*-plane of the slices after embedding. **a** Summary plot of the 2D-dendritic lengths of 6 neurons measured in the *xy*-dimensions of reconstructions made with metal spacer (red circles) and after re-embedding without spacer (blue squares). **b** Normalized dendritic length in the *xy*-dimensions of reconstructions made after conventional embedding (blue bar) calculated relative to the length in the reconstructions with metal spacer. **c** Summary plot of distances between landmarks (13 pairs in 4 slices) in the *xy*-plane measured in photomicrographs of the slices made in the recording chamber (open triangles), at day 4 after embedding with the metal spacer system (red circles) and 14 days after re-embedding without spacer (blue squares). **d** Summary bar chart of landmark distances in the *xy*-plane measured in the slices made with the metal spacer (red bar) and after re-embedding without spacer (blue bar) normalized to the corresponding distances in the recording chamber (16 sets of distances in 4 slices). Error bars indicate standard deviation; statistical significance: * $p < 0.05$, *** $p < 0.001$

($p < 0.0001$, Wilcoxon signed rank test, 110 dendritic segments from 4 pairs of image stacks, Online Resource 3a, b).

Finally, to assess the dilation of the slices directly, we have made photomicrographs of a set of slices, first, in the recording chamber, second, at day 4 after embedding with the metal spacer and, finally, 14 days after re-embedding the

slices without a spacer. Measurements of distances between landmarks in the plane of the slices (i.e. in the *xy*-plane) showed that their dimensions were minimally reduced, by a factor of $2.9 \pm 3.6\%$ on average, when they were mounted and imaged with the metal spacer relative to their dimensions in the recording chamber ($p = 0.01$, Wilcoxon signed rank test, 16 sets of measurements in 4 slices; Fig. 4c, d). In contrast, when re-embedded without a spacer, the slices showed a dilation of $4.2 \pm 5.5\%$ relative to their dimensions in the recording chamber ($p = 0.02$, Wilcoxon signed rank test, Fig. 4c, d).

In summary, our analysis of the neuronal morphologies obtained with the two different embedding method demonstrate that shrinkage with conventional embedding is not uniform along the *z*-axis and the slices suffer additional deformation in the form of dilation in the *xy*-plane. Therefore, the use of a linear correction factor applied to the *z*-axis cannot properly compensate for morphological errors produced by the shrinkage process and may even accentuate some aspects of the deformations observed with conventional embedding.

Discussion

Here, we describe a new method for the embedding of acute brain slices with intracellularly labeled neurons and show that the use of a metal spacer can effectively minimize shrinkage along the *z*-axis. We further demonstrated that shrinkage with conventional embedding develops rapidly and leads to a substantial reduction in the thickness of the slices. Moreover, this massive shrinkage along the *z*-axis is non-linear and accompanied by dilation in the *xy*-plane. The impact of these non-uniform deformations on the morphology and anatomical parameters cannot be compensated by linear correction.

Rapid and strong shrinkage of slices with conventional embedding

Histological procedures, which include drying and dehydration, have been shown to produce severe shrinkage of tissue samples (Pyapali et al. 1998; Hellwig, 2000; Marx et al. 2012) unless the samples are postfixed using for example osmium tetroxide to stabilize lipid membranes. A disadvantage of postfixation with osmium, however, is that it leads to strong opacity of the tissue, precluding light microscopic investigations of thicker samples, such as the 300–400 µm acute brain slices used in combined electrophysiological and morphological investigations. While re-sectioning of the slices offers a solution to this problem, the time and workload involved is prohibitive for large series of samples and not justified, unless light microscopy is routinely coupled

with subsequent electron microscopic analysis (Gulyas et al. 1993; Vida et al. 1998).

Elimination of dehydration steps, combined with mounting in an aqueous media, can reduce shrinkage during histological processing. Protocols based on this approach for the visualization of neurons in acute slices have been widely established as a more efficient alternative. However, this approach cannot prevent shrinkage of the slices after embedding (Egger et al. 2008; Swietek et al. 2016). Indeed, our data show that conventional embedding of slices, as whole mounts without spacer, in aqueous media results in severe shrinkage along the *z*-axis. The slices suffer a substantial initial shrinkage already within a few hours after coverslipping. The *z*-shrinkage continues at a high rate in the first days after embedding, but progressively slows down in the following weeks and reaches an asymptotic value of approximately 50% beyond 2 months. Reasons for this shrinkage are most likely the weight of the coverslip and adhesive forces between the glass surfaces and the mounting medium. Additionally, loss of water content can also contribute in the long term. The effect of this deformation on cellular morphology is a function of the direction of neurites: ones which run perpendicular to the slice surface suffer the strongest reduction in length (Egger et al. 2008). Thus, depending on the orientation of the dendrites and axons, some cells will be more affected by this artifact than others.

To prevent shrinkage, an agar spacer has been introduced between slide and coverslip in previous studies (see e.g. Degro et al. 2015). However, we find now that, using such a spacer, one can avoid the initial shrinkage, but cannot prevent it in the long term. In fact, the shrinkage of slices with agar spacer beyond 3–4 days becomes even stronger than in slices embedded without spacer. The dramatic long-term shrinkage (65–75%) with agar spacer was an unexpected finding of our study and the reason for it is not clear. A possible explanation is that water loss of the agar over time could lead to volume loss of the spacer, producing additional adhesive forces affecting the slice. Therefore, we recommended the use of agar spacer only if imaging is performed within a couple of hours after embedding, as a simple and efficient way of temporarily preventing slice deformation. If used in this manner, agar spacer is a cost effective alternative to the metal spacer, as the latter incurs material and production costs.

Non-uniform deformation of embedded slices affects neuronal morphology and anatomical parameters

Assuming a uniform shrinking process, attempt has been made to compensate arising morphological deformation by applying a linear correction factor to 3D reconstructions (Pyapali et al. 1998; Hellwig 2000; Marx et al. 2012; Degro

et al. 2015). However, it is unknown if this compensation is adequate at all. By imaging and reconstructing the same cells twice, first with a metal spacer followed by an embedding without a spacer, we examined the impact of *z*-shrinkage on neuronal morphology and found evidence for a non-uniform shrinkage along the *z*-axis and an associated dilation in the *xy*-plane. These distortions significantly compromise the fidelity of 3D-reconstructions and the derived morphological parameters in a way that cannot be corrected by linear methods: first, our results show that the strongest shrinkage along the *z*-axis occurs closest to the top and bottom cut surfaces of the slices. Non-linear, non-uniform shrinkage in thin brain sections has been previously described in stereological studies (e.g. Gardella et al. 2003). More relevantly, Egger et al. (2008) observed a similar pattern of non-linear shrinkage in acute cortical slices, by comparing neuronal structures imaged first *in vitro* and subsequently after a conventional embedding procedure using aqueous mounting medium. A major reason for the non-uniform shrinkage can be that the superficial parts of the acute slices are more compressible than deeper tissue, due to the damage caused by the slicing procedure and the subsequent washout of debris from these damaged layers (Egger et al. 2008). Additionally, adhesive forces may differentially affect superficial and deep parts of the slices once they are mounted. Thus, while linear models, as a first-order approximation, may help to assess shrinkage-induced morphological errors (Egger et al. 2008), they cannot fully eliminate these errors and will also exaggerate differential deformation by undercompensating *z*-axis shrinkage in superficial and overcompensating it in the deep regions.

Second, our findings reveal that a moderate degree of dilation in the *xy*-plane additionally impacts morphological parameters, such as the dendritic length resulting in an opposing effect. Beside similar histological procedures and embedding, Egger et al. (2008) did not find such dilation. This could be due to the different mounting medium used (Mowiol) in their study. This is supported by findings that, depending on the precise composition of clearing solutions used, tissue samples may show volume expansion, shrinkage, or maintain their volume (Hama et al. 2011, 2015; Kuwajima et al. 2013; Richardson and Lichtman, 2017). The dilation, on one hand, can partially mask the effect of shrinkage. On the other hand, it results in a systemic overestimate of dendritic length, when the linear correction is applied to the *z*-axis. Measurements of the dimensions of the slice before and after embedding can help to estimate the degree of dilation and enabling partial corrections. However, as with *z*-axis shrinkage, these may also suffer from confounding effects of possible non-linearities. In summary, our findings of combined and non-uniform deformations of the slices argue for the need of preventing shrinkage rather than attempting to compensate it.

Metal spacer can efficiently and stably minimize shrinkage of embedded brain slices

Embedding procedure with metal spacers can not only prevent the initial shrinkage directly after embedding, but also strongly minimizes the shrinkage process in the first days post-embedding. Thus, if cells were imaged in that time window, one can achieve minimally-compromised neuronal morphologies and reconstructions. Shrinkage correction is not necessary, as there is only negligible morphological distortion below 5% along *z*-axis and less than 3% in the *xy*-plane. However, the metal spacer system cannot fully prevent slices from shrinkage in the long term, reaching a moderate but significant value of $16.3 \pm 8.9\%$ after two months. As the compression by the coverslips as shrinkage contributor is eliminated, ongoing shrinkage could be caused by the embedding medium. It was previously discussed, that many embedding media, including most aqueous mounting media, enable *z*-shrinkage and only 100% glycerol could fully prevent shrinkage (Claiborne et al. 1986; Mainen et al. 1996). However, when using pure glycerol, it is difficult to seal and handle the slides properly, as medium remains fluid. The slice in its mounting medium can move while imaging with a confocal microscope, leading to compromised images. Long-term storage of mounted slides is a further issue, as the mounting medium evaporates slowly over time. Finally, stained neurons tend to fade in glycerol over time; this effect being noticeable already within weeks (Jaeger 2000). Considering these disadvantages 100% glycerol is not a convenient alternative for embedding.

In summary, slices suffer a marked, non-linear shrinkage along the *z*-axis and associated dilation in *xy*-plane after conventional embedding procedures, causing distortion of neuronal morphology and producing errors in derived anatomical parameters. As these deformations are non-compensable with simple, linear approaches, minimizing these effects is imperative. The metal spacer system can efficiently and stably minimize these artifacts, particularly within the first days post-embedding, and, thereby, provides a substantial improvement for morphological investigations of intracellularly labeled neurons in acute slices.

Acknowledgements We thank Ina Wolter for assisting with tissue processing and Christian Merz for his help creating the schemes for the figures. We also thank Daniel Veik of wh Münzprüfer Berlin for excellent consultancy and support.

Author contributions Study conception and experimental design by IV; data collection and analysis were performed by FB and SG. The first draft of the manuscript was written by FB. All the authors participated in writing, reviewing, and editing of the manuscript. All authors have read and approved the final version.

Funding Open Access funding provided by Projekt DEAL. The research was supported by the German Research Fund (Deutsche Forschungsgemeinschaft, DFG FOR 2143 and VI353-4/1 to I.V.).

Compliance with ethical standards

Conflict of interest The authors declare that they have no conflict of interest.

Research involving animals/ethical approval All procedures, the care and handling of animals in this study followed European Union and national regulations (German Animal Welfare Act) and all experiments were performed in accordance with institutional guidelines (Charité—Universitätmedizin Berlin), with permissions from local authorities (LaGeSo, Berlin, T-0215/11).

Open Access This article is licensed under a Creative Commons Attribution 4.0 International License, which permits use, sharing, adaptation, distribution and reproduction in any medium or format, as long as you give appropriate credit to the original author(s) and the source, provide a link to the Creative Commons licence, and indicate if changes were made. The images or other third party material in this article are included in the article's Creative Commons licence, unless indicated otherwise in a credit line to the material. If material is not included in the article's Creative Commons licence and your intended use is not permitted by statutory regulation or exceeds the permitted use, you will need to obtain permission directly from the copyright holder. To view a copy of this licence, visit <http://creativecommons.org/licenses/by/4.0/>.

References

- Bartos M, Vida I, Frotscher M, Meyer A, Monyer H, Geiger JRP, Jonas P (2002) Fast synaptic inhibition promotes synchronized gamma oscillations in hippocampal interneuron networks. *Proc Natl Acad Sci* 99:13222–13227
- Booker SA, Song J, Vida I (2014) Whole-cell patch-clamp recordings from morphologically- and neurochemically-identified hippocampal interneurons. *J Vis Exp* 91:e51706
- Cannon RC, Turner DA, Pyapali GK, Wheal HV (1998) An on-line archive of reconstructed hippocampal neurons. *J Neurosci Methods* 84:49–54
- Claiborne BJ, Amaral DG, Cowan WM (1986) A light and electron microscopic analysis of the mossy fibers of the rat dentate gyrus. *J Comp Neurol* 246:435–458
- de Sousa G, Maex R, Adams R, Davey N, Steuber V (2015) Dendritic morphology predicts pattern recognition performance in multi-compartmental model neurons with and without active conductances. *J Comput Neurosci* 38:221–234
- DeFelipe J, Lopez-Cruz PL, Benavides-Piccione R, Bielza C, Larranaga P, Anderson S, Burkhalter A, Cauli B, Fairen A, Feldmeyer D, Fishell G, Fitzpatrick D, Freund TF, Gonzalez-Burgos G, Hestrin S, Hill S, Hof PR, Huang J, Jones EG, Kawaguchi Y, Kisvárdy Z, Kubota Y, Lewis DA, Marin O, Markram H, McBain CJ, Meyer HS, Monyer H, Nelson SB, Rockland K, Rossier J, Rubenstein JL, Rudy B, Scanziani M, Shepherd GM, Sherwood CC, Staiger JF, Tamas G, Thomson A, Wang Y, Yuste R, Ascoli GA (2013) New insights into the classification and nomenclature of cortical GABAergic interneurons. *Nat Rev Neurosci* 14:202–216
- Degro CE, Kulik A, Booker SA, Vida I (2015) Compartmental distribution of GABAB receptor-mediated currents along the

- somatodendritic axis of hippocampal principal cells. *Front Synaptic Neurosci* 7:6
- Dorph-Petersen KA, Nyengaard JR, Gundersen HJ (2001) Tissue shrinkage and unbiased stereological estimation of particle number and size. *J Microsc* 204:232–246
- Egger V, Nevian T, Bruno RM (2008) Subcolumnar dendritic and axonal organization of spiny stellate and star pyramid neurons within a barrel in rat somatosensory cortex. *Cereb Cortex* 18:876–889
- Feng L, Zhao T, Kim J (2015) neuTube 1.0: a new design for efficient neuron reconstruction software based on the SWC format. *eNeuro*. <https://doi.org/10.1523/ENEURO.0049-14.2014>
- Gardella D, Hatton WJ, Rind HB, Rosen GD, von Bartheld CS (2003) Differential tissue shrinkage and compression in the z-axis: implications for optical disector counting in vibratome-, plastic- and cryosections. *J Neurosci Methods* 124:45–59
- Gidon A, Zolnik TA, Fidzinski P, Bolduan F, Papoutsis A, Poirazi P, Holtkamp M, Vida I, Larkum ME (2020) Dendritic action potentials and computation in human layer 2/3 cortical neurons. *Science* 367:83–87
- Gulledge AT, Bravo JJ (2016) Neuron morphology influences axon initial segment plasticity. *eNeuro*. <https://doi.org/10.1523/ENEURO.0085-0015.2016>
- Gulyas AI, Miles R, Hajos N, Freund TF (1993) Precision and variability in postsynaptic target selection of inhibitory cells in the hippocampal CA3 region. *Eur J Neurosci* 5:1729–1751
- Hama H, Kurokawa H, Kawano H, Ando R, Shimogori T, Noda H, Fukami K, Sakaue-Sawano A, Miyawaki A (2011) Scale: a chemical approach for fluorescence imaging and reconstruction of transparent mouse brain. *Nat Neurosci* 14:1481–1488
- Hama H, Hioki H, Namiki K, Hoshida T, Kurokawa H, Ishidate F, Kaneko T, Akagi T, Saito T, Saito T, Miyawaki A (2015) ScaleS: an optical clearing palette for biological imaging. *Nat Neurosci* 18:1518–1529
- Hellwig B (2000) A quantitative analysis of the local connectivity between pyramidal neurons in layers 2/3 of the rat visual cortex. *Biol Cybern* 82:111–121
- Hines ML, Carnevale NT (1997) The NEURON simulation environment. *Neural Comput* 9:1179–1209
- Jaeger D (2000) Accurate reconstruction of neuronal morphology. *Computational neuroscience: realistic modeling for experimentalists*. CRC Press, New York, pp 159–178
- Kasper EM, Larkman AU, Lubke J, Blakemore C (1994) Pyramidal neurons in layer 5 of the rat visual cortex. I. Correlation among cell morphology, intrinsic electrophysiological properties, and axon targets. *J Comp Neurol* 339:459–474
- Kuwajima T, Sitko AA, Bhansali P, Jurgens C, Guido W, Mason C (2013) ClearT: a detergent- and solvent-free clearing method for neuronal and non-neuronal tissue. *Development* 140:1364–1368
- Longair MH, Baker DA, Armstrong JD (2011) Simple neurite tracer: open source software for reconstruction, visualization and analysis of neuronal processes. *Bioinformatics* 27:2453–2454
- Mainen ZF, Carnevale NT, Zador AM, Claiborne BJ, Brown TH (1996) Electrotonic architecture of hippocampal CA1 pyramidal neurons based on three-dimensional reconstructions. *J Neurophysiol* 76:1904–1923
- Major G, Larkman AU, Jonas P, Sakmann B, Jack JJ (1994) Detailed passive cable models of whole-cell recorded CA3 pyramidal neurons in rat hippocampal slices. *J Neurosci* 14:4613–4638
- Marx M, Gunter RH, Hucko W, Radnikow G, Feldmeyer D (2012) Improved biocytin labeling and neuronal 3D reconstruction. *Nat Protoc* 7:394–407
- Mihaljevic B, Larranaga P, Benavides-Piccione R, Hill S, DeFelipe J, Bielza C (2018) Towards a supervised classification of neocortical interneuron morphologies. *BMC Bioinform* 19:511
- Norenberg A, Hu H, Vida I, Bartos M, Jonas P (2010) Distinct nonuniform cable properties optimize rapid and efficient activation of fast-spiking GABAergic interneurons. *Proc Natl Acad Sci USA* 107:894–899
- Preibisch S, Saalfeld S, Tomancak P (2009) Globally optimal stitching of tiled 3D microscopic image acquisitions. *Bioinformatics* 25:1463–1465
- Pyapali GK, Sik A, Penttonen M, Buzsaki G, Turner DA (1998) Dendritic properties of hippocampal CA1 pyramidal neurons in the rat: intracellular staining in vivo and in vitro. *J Comp Neurol* 391:335–352
- Ramón y Cajal S (1909, 1911) *Histologie du Système Nerveux de l'Homme et des Vertébrés*. Maloine, Paris, France
- Richardson DS, Lichtman JW (2017) SnapShot: tissue clearing. *Cell* 171:496–496.e491
- Schindelin J, Arganda-Carreras I, Frise E, Kaynig V, Longair M, Pietzsch T, Preibisch S, Rueden C, Saalfeld S, Schmid B, Tinevez JY, White DJ, Hartenstein V, Eliceiri K, Tomancak P, Cardona A (2012) Fiji: an open-source platform for biological-image analysis. *Nat Methods* 9:676–682
- Swietek B, Gupta A, Proddutur A, Santhakumar V (2016) Immunostaining of biocytin-filled and processed sections for neurochemical markers. *J Vis Exp* 118:e54880
- Thomson AM, Armstrong WE (2011) Biocytin-labelling and its impact on late 20th century studies of cortical circuitry. *Brain Res Rev* 66:43–53
- Traub RD, Jefferys JG, Miles R, Whittington MA, Tóth K (1994) A branching dendritic model of a rodent CA3 pyramidal neurone. *J Physiol* 481:79–95
- Vida I, Halasy K, Szinyei C, Somogyi P, Buhl EH (1998) Unitary IPSPs evoked by interneurons at the stratum radiatum-stratum lacunosum-moleculare border in the CA1 area of the rat hippocampus in vitro. *J Physiol* 506:755–773

Publisher's Note Springer Nature remains neutral with regard to jurisdictional claims in published maps and institutional affiliations.

3.2. Dendritic action potentials and computation in human layer 2/3 cortical neurons

RESEARCH

NEUROSCIENCE

Dendritic action potentials and computation in human layer 2/3 cortical neurons

Albert Gidon¹, Timothy Adam Zolnik¹, Pawel Fidzinski^{2,3}, Felix Bolduan⁴, Athanasia Papoutsi⁵, Panayiota Poirazi⁵, Martin Holtkamp², Imre Vida^{3,4}, Matthew Evan Larkum^{1,3*}

The active electrical properties of dendrites shape neuronal input and output and are fundamental to brain function. However, our knowledge of active dendrites has been almost entirely acquired from studies of rodents. In this work, we investigated the dendrites of layer 2 and 3 (L2/3) pyramidal neurons of the human cerebral cortex *ex vivo*. In these neurons, we discovered a class of calcium-mediated dendritic action potentials (dCaAPs) whose waveform and effects on neuronal output have not been previously described. In contrast to typical all-or-none action potentials, dCaAPs were graded; their amplitudes were maximal for threshold-level stimuli but dampened for stronger stimuli. These dCaAPs enabled the dendrites of individual human neocortical pyramidal neurons to classify linearly nonseparable inputs—a computation conventionally thought to require multilayered networks.

The expansion of the human brain during evolution led to an extraordinarily thick cortex (~3 mm), which is disproportionately thickened in layers 2 and 3 (L2/3) (1). Consequently, human cortical neurons of L2/3 constitute large and elaborate dendritic trees (2, 3), decorated by numerous synaptic inputs (1). The active electrical properties of these dendrites largely determine the repertoire of transformations of the synaptic inputs to axonal action potentials (APs) at the output. Thus, they constitute a key element of the neuron's computational power.

We used dual somatodendritic patch clamp recordings and two-photon imaging to directly investigate the active properties of L2/3 dendrites in acute slices from surgically resected brain tissue of the human neocortex from epilepsy and tumor patients. Subthreshold (steady-state) potentials attenuated from the dendrite to the soma with a length constant (λ_{steady}) of 195 μm (fig. S1; $n = 23$ cells). In the opposite direction, the back-propagating action potentials (bAPs) attenuated from the soma to the dendrite with a λ_{bAP} of 290 μm (Fig. 1, A to C; $n = 31$ cells). Both λ_{bAP} and λ_{steady} were shorter than the length of the apical dendrite (the somata of these cells were located ~850 μm below the pia mater, on average, and the apical dendrite extended up to layer 1), which implies that strong attenuation governs the electrical activity to and from most synapses located on the apical dendrite.

We filled cells with the calcium indicator Oregon-green BAPTA-1 (100 μM) and measured the change in fluorescence ($\Delta F/F$) under a two-photon microscope while triggering APs at the soma. Trains of somatic APs (10 APs) at 50 Hz failed to cause Ca^{2+} influx at distal apical dendrites (fig. S2). AP trains with a higher frequency (10 APs at 200 Hz) did invade most of the apical dendrite, similarly to what has been shown previously in rodent L2/3 pyramidal neurons (4). However, these high-frequency signals were substantially attenuated at distal tuft dendrites (fig. S2). Furthermore, Ca^{2+} influx in spines was similar to that in the nearby dendritic branches, regardless of the somatic AP frequency (fig. S2D).

We next examined whether human L2/3 dendrites have intrinsic mechanisms to compensate for the large dendritic attenuation. We injected a current step into the dendrite (I_{dend}) and recorded the membrane potentials at both the dendrite and at the soma. At the soma and at the proximal dendritic sites (170 μm from the soma, on average), a suprathreshold current readily evoked somatic APs, which back-propagated into the dendrite (Fig. 1, A and B, and fig. S5H). However, when the dendritic electrode was positioned more distally, suprathreshold stimuli often evoked trains of repetitive APs that were initiated exclusively in the dendrite (Fig. 1D; for transient stimulus, see fig. S10). These results imply that L2/3 dendrites in human cortical pyramidal neurons are distinctly more excitable than the homolog dendrites in rodents, where similar steady currents evoke, at most, only a single dendritic AP at the beginning of the voltage response (5). In contrast to L2/3 pyramidal neurons, layer 5 pyramidal neurons of the human neocortex were recently reported to have reduced dendritic excitability compared with their homolog neurons in rodents (6).

High-frequency dendritic APs (>200 Hz) that were uncoupled from somatic firing have

been observed in rodent dendrites *in vivo* (7, 8). The authors of these studies have attributed these spikes to dendritic voltage-gated Na^+ channels and/or *N*-methyl-D-aspartate (NMDA) receptors. The dendritic APs in human L2/3 neurons were not blocked by the sodium channel blocker tetrodotoxin (1 μM ; $n = 4$ cells; fig. S3), but they were abolished by the Ca^{2+} channel blocker Cd^{2+} (200 μM ; $n = 5$ cells; fig. S3). The dendritic Ca^{2+} APs that we observed in human L2/3 neurons have not been described in the cortical neurons of other mammalian species. Dendritic APs that are mediated (or are assumed to be mediated) by sodium currents in rodents' neurons have been variously named dendritic spikes (9), prepotentials (10), Na-dSpikes (11), and dendritic action potentials (DAPs) (8). To distinguish the dendritic APs that we found in the human dendrites from those described previously, we refer to them as dendritic Ca^{2+} APs (dCaAPs).

dCaAPs were present not only in neurons from the temporal lobe of epilepsy patients but also in neurons from other neocortical areas of tumor patients ($n = 4$ cells from 3 patients; fig. S4). This suggests that dCaAPs are neither regionally confined nor related to pathology.

The waveform of dCaAPs was stereotypical and easily distinguished from that of bAPs. dCaAPs were typically wider than bAPs (with widths of 4.4 ± 1.4 ms, ranging between 2.6 and 8.0 ms; $n = 32$ cells), they were slow rising, and they did not have a kink at onset (7) (Fig. 1D). The majority of the cells (27 of 39) showed a train of (two or more) dCaAPs with a mean firing rate of 4.6 ± 1.7 Hz (dCaAPs per second). In the remaining 12 dendrites, a single dCaAP was triggered immediately after the beginning of the stimulus. Unlike the bAP (Fig. 1C), the amplitude of the dCaAPs (Fig. 1E) and their upstroke (fig. S5) were not dependent on the distance from the soma (average dCaAP amplitude 43.8 ± 13.8 mV, ranging between 13.0 and 67.0 mV; $n = 32$ cells, measured at threshold). This is consistent with both variability of the dCaAP initiation site and variability of dCaAP properties (for further details, see figs. S5 and S11). We never detected high-amplitude, long-duration, Ca^{2+} -mediated plateau potentials, which are common in the apical dendrites of L5 neurons in rodents.

The impact of dCaAPs on the soma was variable. In some of the cells (17 of 37), the dCaAPs were coupled with somatic APs (coupled dCaAPs; e.g., Fig. 1F). Unlike forward-propagating dendritic APs in other pyramidal neurons (12–14), coupled dCaAPs triggered somatic APs immediately and/or with a delay ranging between 21.6 and 116.9 ms (53.8 ± 26.8 ms, on average, in 11 out of 17 coupled cells; Fig. 1, F and G, and fig. S6). Coupled dCaAPs that triggered somatic APs with a delay were classified as complex.

¹Institute for Biology, Humboldt-Universität zu Berlin, Berlin, Germany. ²Epilepsy-Center Berlin-Brandenburg, Department of Neurology, Charité - Universitätsmedizin Berlin, Berlin, Germany. ³NeuroCure Cluster, Charité - Universitätsmedizin Berlin, Berlin, Germany. ⁴Institute of Integrative Neuroanatomy, Charité-Universitätsmedizin Berlin, Berlin, Germany. ⁵Institute of Molecular Biology and Biotechnology, Foundation for Research and Technology - Hellas (IMBB-FORTH), Crete, Greece. *Corresponding author. Email: matthew.larkum@hu-berlin.de

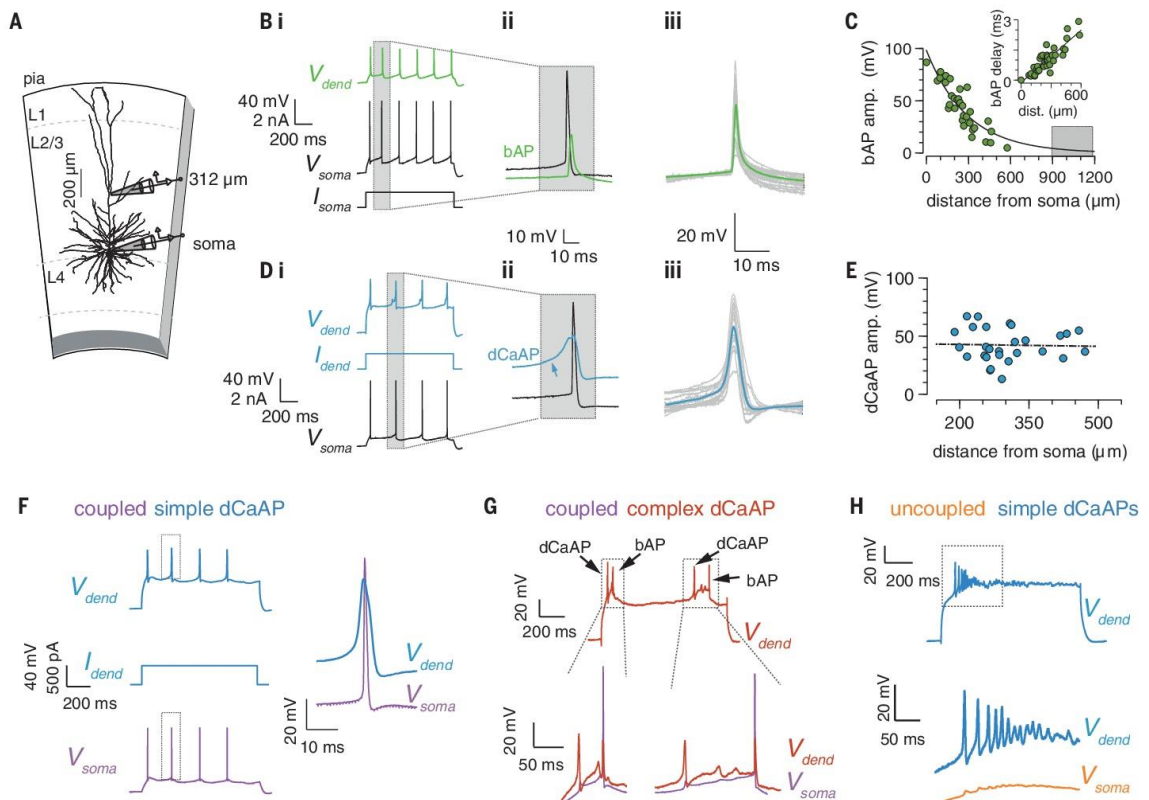


Fig. 1. bAPs and dCaAPs in human dendrites of L2/3 neurons.

(A) Experimental setting: L2/3 neuron at a depth of 1130 μm below the pial surface, with a somatic electrode and a dendritic electrode placed at 312 μm from the soma. (B) (i) Recordings from the cell in (A). bAPs in green (V_{dend}) and corresponding somatic APs in black (V_{soma}) triggered by somatic current injection (I_{soma}) are shown. (ii) Somatic AP preceded the bAP [magnified from the frame in (i)]. (iii) bAPs in 16 dendrites (gray) and their average (green) aligned to their peak. (C) bAP amplitude (green dots) and exponential fit (length constant $\lambda_{\text{bAP}} = 290 \mu\text{m}$; $n = 31$ cells; dashed line) against distance from the soma. Gray area indicates the putative tuft region in layer 1 for the longest dendrite. (Inset) Delay of the bAP peak against distance from the soma with linear fit ($r^2 = 0.78$, where r^2 is the coefficient of determination). amp., amplitude; dist., distance. (D) (i) dCaAPs (V_{dend} ,

blue) triggered by a square current injected at the dendrite (I_{dend}) and the resulting somatic AP (black) from the cell in (A). (ii) Somatic AP (in black) and a dCaAP (in blue) magnified from (i). The slow rising dCaAP (blue arrow) precedes the somatic AP. (iii) Initial dCaAP in each recording at threshold in the same 16 dendrites (gray) in (iii) of (B) and their average trace (blue) aligned to their peak. (E) dCaAP amplitude is independent of the distance from the soma ($n = 28$ cells). Linear fit is shown with the dashed line ($r^2 = 0.0009$). (F) (Left) Coupled and simple dCaAPs (blue trace) and somatic APs (purple trace) triggered by I_{dend} . (Right) Magnified dCaAP (in blue) and a somatic AP (in purple) framed in the traces on the left are shown. (G) (Top) Two coupled and complex dCaAPs (in red) triggered delayed somatic APs [in purple, magnified at (bottom)]. (H) Burst of simple and uncoupled dCaAPs in blue (top) with somatic APs (bottom).

Without exception, each coupled dCaAP triggered a single somatic AP, which implies that, unlike calcium APs in the dendrites of other neurons (15, 16), dCaAPs did not induce bursts of somatic APs. In the other 20 cells, dCaAPs were uncoupled. They were confined to the apical dendrite, unable to evoke somatic APs. Typically, uncoupled dCaAPs were observed in more distal dendritic recording sites ($335 \pm 113 \mu\text{m}$ from the soma) than the coupled dCaAPs that triggered somatic APs ($265 \pm 71 \mu\text{m}$ from the soma), but the distance difference was not statistically significant (Wilcoxon

rank sum test, $P = 0.077$). Additionally, one coupled and three uncoupled cells fired bursts of three or more dCaAPs at the beginning of the stimulus (28 to 73 Hz). In fig. S7, we summarize the classification of the dCaAPs on the basis of their ability to trigger APs at the soma (i.e., coupled versus uncoupled) and their complexity (i.e., complex and/or simple). Most of the dendrites with complex dCaAPs also triggered simple dCaAPs, suggesting that their behavior might be activity- or input-dependent and/or modulated by other factors (17).

dCaAPs affected the input–output transformation of the cells. Typically, somatic AP firing increases with the input current intensity injected to the soma. In contrast, in 4 cells (out of 12 cells that had repetitive and coupled dCaAPs) our recordings revealed an inverse behavior where increasing the intensity of dendritic (rather than somatic) current injection resulted in decreased somatic firing. For example, in Fig. 2, A and B, the dendritic electrode evoked one or two somatic APs with current near threshold but failed to evoke APs for higher current intensity. In contrast, at the

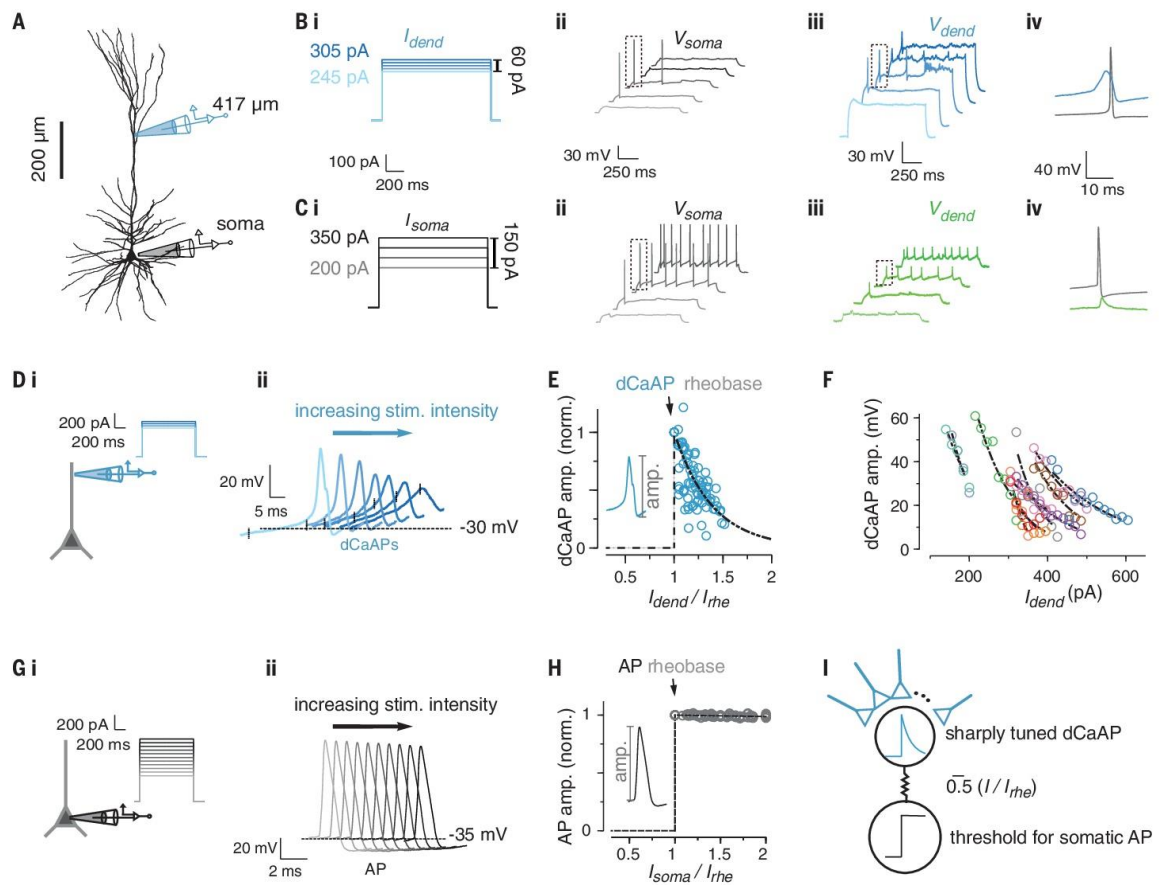


Fig. 2. dCaAPs are sharply tuned to the stimulus intensity. (A) L2/3 pyramidal neuron with soma 886 μm below the pia. The somatic and dendritic electrodes are shown in black and blue, respectively. Recordings from this cell are shown in (B) and (C). (B) Dendritic current (I_{dend}) injected 417 μm from the soma (i) and corresponding somatic (ii) and dendritic traces (iii). (ii) I_{dend} of 260 and 275 pA, but neither smaller nor larger current, resulted in somatic APs. (iii) dCaAP amplitudes were maximal for I_{dend} of 260 and 275 pA, whereas $I_{\text{dend}} > 275$ pA dampened them. (iv) dCaAP (in blue) precedes the somatic AP (in gray); traces are magnified from the framed APs in (ii) and (iii). (C) Somatic current injection, I_{soma} (i), somatic AP trains (ii), and bAP (iii) for similar ranges of current intensity as those shown in (i) of (B). (iv) Somatic AP (in gray) precedes the dendritic bAP (in green); traces are magnified from the framed APs in (ii) and (iii). (D) Increase in I_{dend} (i) dampened

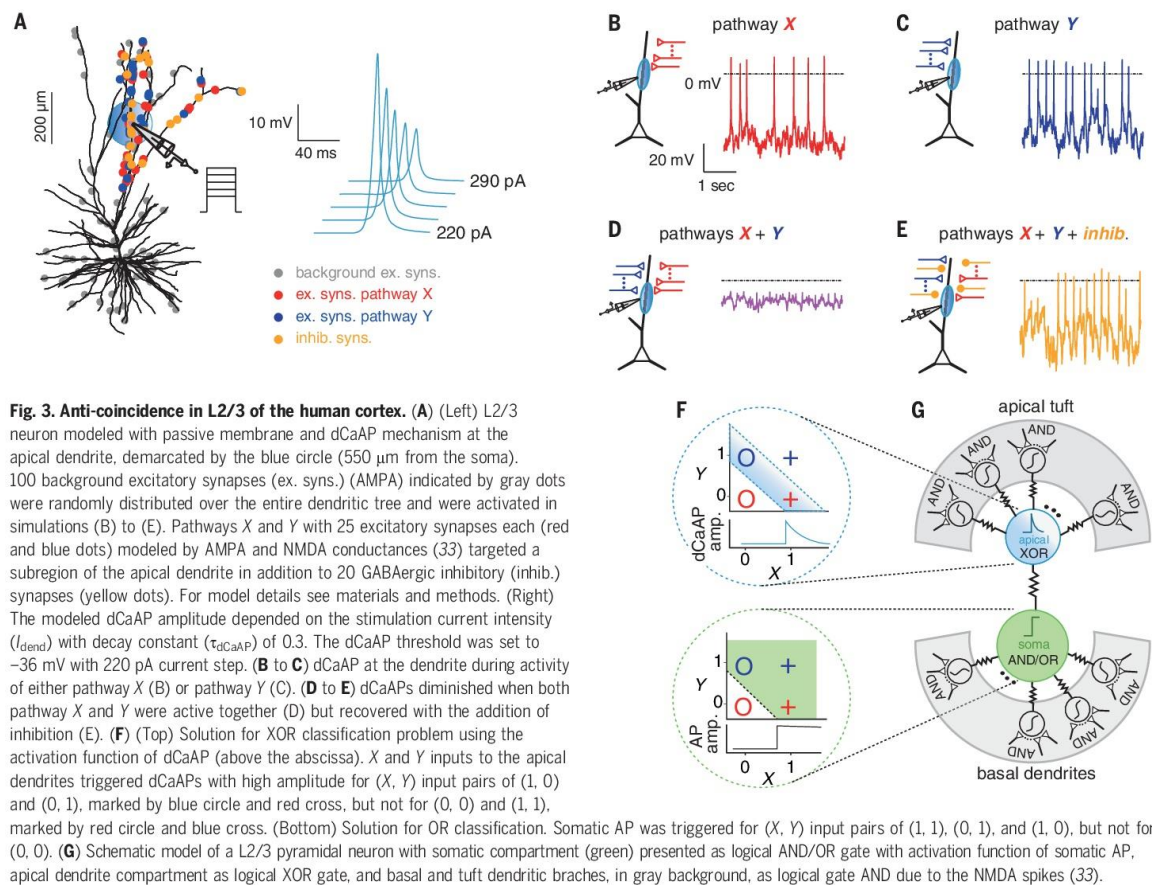
the dCaAPs' amplitude (ii); vertical tick on each trace marks 50 ms after I_{dend} onset. stim., stimulation; norm., normalized. (E) Amplitude of the first dCaAP in each trace against I_{dend} normalized by rheobase (I_{rhe}) for uncoupled dCaAPs (12 dendrites) and exponential fit (dashed line), with a decay constant (τ_{dCaAP}) of 0.39 (median 0.38) in units of rheobase. (F) dCaAP amplitudes as in (E) but not normalized by I_{rhe} . Dots in different colors represent dCaAP amplitudes from different cell (12 dendrites) with exponential fit (dashed lines). (G) As in (D) but for somatic APs. I_{soma} (i) and the resulting somatic APs (ii). (H) AP amplitude plotted against the normalized somatic input current strength ($I_{\text{soma}}/I_{\text{rhe}}$). The amplitude of the somatic AP was fixed and did not depend on I_{soma} for a range of stimuli strengths as in (ii) of (G) (exponential fit with $\tau_{\text{AP}} = 82$, units of somatic I_{rhe}). (I) Dendritic and somatic activation functions for dCaAPs (blue curve) and for somatic APs (black curve).

soma of the same cells, AP output increased with the input's strength (Fig. 2C). These results are explained by the unusual active properties of dCaAPs. dCaAPs evoked by the dendritic electrode triggered somatic APs near threshold but were suppressed by further increase in the stimulus intensity (Fig. 2B).

The dendritic activation function (namely, the amplitude of dCaAPs as a function of the intensity of the current injection in the den-

drite, I_{dend}) reached its maximal value at the rheobase (i.e., for $I_{\text{dend}} = I_{\text{rhe}}$ where I_{rhe} is the threshold current for triggering a dCaAP) and decayed for stronger I_{dend} (Fig. 2, D to F; 12 uncoupled dCaAPs). The mean width of the dendritic activation function (defined here as the decay constant of a single exponential fit) was 0.39 (0.38 median; in units of I_{rhe}), which indicates that dCaAPs are sharply tuned (highly selective) to a particular input strength. Addi-

tionally, L2/3 dendrites were heterogeneous in their activation function threshold and width (Fig. 2F). In contrast, in a similar range of input intensities, somatic APs (Fig. 2, G to H) showed a typical threshold activation function; once a somatic AP was triggered, its amplitude was virtually independent of the input intensity (Fig. 2H). Unlike other dendritic APs in the mammalian neocortex—namely, NMDA spikes (18) and dendritic Ca^{2+} APs in layer



5 pyramidal neurons (15, 19–22)—that were previously shown to increase with the stimulus strength, the activation function of dCaAPs in L2/3 neurons was sharply tuned to a specific input strength (Fig. 2I).

We used a compartmental model of a L2/3 pyramidal neuron that replicated the phenomenology of the dCaAP behavior in the dendrite to investigate the functional outcome of the dCaAP activation function (for a biophysical model of dCaAPs, see fig. S12). L2/3 pyramidal neuron morphology was digitally reconstructed and modeled in the NEURON (23) simulation environment (Fig. 3A). The dCaAP's threshold, width, and amplitude as a function of the input strength were simulated by the sum of current sources with a sigmoidal shape (for details, see materials and methods and Fig. 3A, right panel). To simulate two distinct classes of inputs, pathways X and Y, we used 25 excitatory synapses for each pathway (Fig. 3A), targeting a subregion of the apical dendrite (blue and red dots in Fig. 3A). Each of these pathways was able to trigger dCaAPs by

itself (Fig. 3, B and C). Because of the activation function of the dCaAPs in our simulation, coincident activation of two synaptic input pathways diminished the dCaAP amplitude (Fig. 3D) in contrast to other dendritic APs that amplify coincident dendritic inputs (24) [e.g., in layer 5 pyramidal neurons in the rodent neocortex (25) or in CA1 neurons of the rodent hippocampus (26)]. Our simulation is therefore a simple and explicit demonstration of how the dendritic mechanism computes an anticoincident function for multiple input pathways, limiting the number and/or the strength of inputs integrated in the dendrite (for impact on the cell body, see fig. S9). Inhibition (27, 28) placed at the same dendritic subregion (20 GABAergic synapses), in addition to the two excitatory pathways, repolarized the membrane and recovered the amplitude of the dCaAPs [Fig. 3E; (29)]. These results suggest that the precise balance between excitation and inhibition is essential for the generation of dCaAPs and indicate a

counterintuitive role for inhibition in enhancing the excitability of the dendrite (see also fig. S9, C and D).

It has long been assumed that the summation of excitatory synaptic inputs at the dendrite and the output at the axon can only instantiate logical operations such as AND and OR (30). Traditionally, the XOR operation has been thought to require a network solution (31, 32). We found that the dCaAPs' activation function allowed them to effectively compute the XOR operation in the dendrite by suppressing the amplitude of the dCaAP when the input is above the optimal strength (Fig. 2). Thus, on the basis of our results and those of previous studies (30, 33), we consider a model that portrays the somatic and dendritic compartments of L2/3 neurons as a network of coupled logical operators and corresponding activation functions (Fig. 3, F and G). In this model, the XOR operation is performed in the dendrites with dCaAPs, whereas AND/OR operations are performed at the soma and at tuft and basal dendrites

with sodium and NMDA spikes, respectively (20, 25, 34, 35). Our findings provide insights into the physiological building blocks that constitute the algorithms of cellular function, which ultimately give rise to the cortical network behavior.

REFERENCES AND NOTES

1. J. DeFelipe, L. Alonso-Nanclares, J. I. Arellano, *J. Neurocytol.* **31**, 299–316 (2002).
2. H. Mohan *et al.*, *Cereb. Cortex* **25**, 4839–4853 (2015).
3. Y. Detscher *et al.*, *Cereb. Cortex* **27**, 5398–5414 (2017).
4. J. Waters, M. Larkum, B. Sakmann, F. Helmchen, *J. Neurosci.* **23**, 8558–8567 (2003).
5. M. E. Larkum, J. Waters, B. Sakmann, F. Helmchen, *J. Neurosci.* **27**, 8999–9008 (2007).
6. L. Beaulieu-Laroche *et al.*, *Cell* **175**, 643–651e14 (2018).
7. S. L. Smith, I. T. Smith, T. Branco, M. Häusser, *Nature* **503**, 115–120 (2013).
8. J. J. Moore *et al.*, *Science* **355**, eaaj1497 (2017).
9. B. Sivyer, S. R. Williams, *Nat. Neurosci.* **16**, 1848–1856 (2013).
10. S. Crochet, P. Fuentealba, I. Timofeev, M. Steriade, *Cereb. Cortex* **14**, 1110–1121 (2004).
11. Y. Kim, C.-L. Hsu, M. S. Cembrowski, B. D. Mensh, N. Spruston, *eLife* **4**, e06414 (2015).
12. M. E. Larkum, J. J. Zhu, B. Sakmann, *J. Physiol.* **533**, 447–466 (2001).
13. N. L. Golding, N. Spruston, *Neuron* **21**, 1189–1200 (1998).
14. L. M. Palmer *et al.*, *Nat. Neurosci.* **17**, 383–390 (2014).
15. M. E. Larkum, J. J. Zhu, B. Sakmann, *Nature* **398**, 338–341 (1999).
16. N. L. Golding, H. Y. Jung, T. Mickus, N. Spruston, *J. Neurosci.* **19**, 8789–8798 (1999).
17. C. Labarrera *et al.*, *Cell Rep.* **23**, 1034–1044 (2018).
18. J. Schiller, G. Major, H. J. Koester, Y. Schiller, *Nature* **404**, 285–289 (2000).
19. M. E. Larkum, K. M. M. Kaiser, B. Sakmann, *Proc. Natl. Acad. Sci. U.S.A.* **96**, 14600–14604 (1999).
20. M. E. Larkum, T. Nevian, M. Sandler, A. Polsky, J. Schiller, *Science* **325**, 756–760 (2009).
21. J. J. Zhu, *J. Physiol.* **526**, 571–587 (2000).
22. J. Schiller, Y. Schiller, G. Stuart, B. Sakmann, *J. Physiol.* **505**, 605–616 (1997).
23. M. L. Hines, N. T. Carnevale, *Neural Comput.* **9**, 1179–1209 (1997).
24. M. London, M. Häusser, *Annu. Rev. Neurosci.* **28**, 503–532 (2005).
25. A. Polsky, B. W. Mel, J. Schiller, *Nat. Neurosci.* **7**, 621–627 (2004).
26. A. Losonczy, J. C. Magee, *Neuron* **50**, 291–307 (2006).
27. E. Boldog *et al.*, *Nat. Neurosci.* **21**, 1185–1195 (2018).
28. A. Gidon, I. Segev, *Neuron* **75**, 330–341 (2012).
29. A. T. Gullledge, G. J. Stuart, *Neuron* **37**, 299–309 (2003).
30. G. M. Shepherd, R. K. Brayton, *Neuroscience* **21**, 151–165 (1987).
31. M. Minsky, S. A. Papert, *Perceptrons: An Introduction to Computational Geometry* (MIT Press, 1969).
32. F. Rosenblatt, *The Perception, a Perceiving and Recognizing Automaton: (Project Para)* (Cornell Aeronautical Laboratory, 1957).
33. G. Eyal *et al.*, *Front. Cell. Neurosci.* **12**, 181 (2018).
34. P. Poirazi, T. Brannon, B. W. Mel, *Neuron* **37**, 989–999 (2003).
35. G. Testa-Silva, S. Honnuraiah, C. French, J. King, K. Drummond, L. M. Palmer, G. J. Stuart, “NMDA spikes in human neocortex” program no. 463.12, 2018 *Neuroscience Meeting Planner*, Society for Neuroscience, San Diego, CA, 3 to 7 November 2018.
36. A. Gidon *et al.*, Dendritic action potentials and computation in human layer 2/3 cortical neurons. Zenodo (2020); <https://doi.org/10.5281/zenodo.3530043>.

ACKNOWLEDGMENTS

We thank U. Schneider for providing the human tissue; L. Kraus, A. Ragot, O. Kruchik, and I. Wolter for assisting with human tissue processing; and S. Gresser and F. J. Barreda Tomás for assisting

with confocal imaging. **Funding:** This work was supported by Deutsche Forschungsgemeinschaft DFG: 2112280105 (to T.A.Z.), EXC 257 (to I.V., P.P., and M.E.L.), FOR 2143 (to I.V.), EXC 2049 (to P.F.), LA 3442/3-1 (to M.E.L.), SPP1665 (to M.E.L.), and SFB1078 B2 (to M.E.L.); 7FP Health-F2-602531-2013 DESIRE (to M.H.); Hellenic Foundation for Research and Innovation HFRI and the General Secretariat for Research and Technology GSRT 1357 (to A.P.); Humboldt Foundation Friedrich Wilhelm Bessel Research Award (to P.P.); H2020 European Research Council ERC STG 311435 (to P.P.); H2020 Research and Innovation Programme 720270/HBP SGA1, 785907/HBP SGA2, and 670118/ERC ActiveCortex (to M.E.L.); and EMBO ALTF 1193–2015 (to A.G.).

Author contributions: M.E.L. and A.G. conceptualized and performed the experiments and analysis and wrote the original draft. T.A.Z. performed the 2-p experiments. P.F. and M.H. managed human tissue ethical aspects, delivery, and quality optimization. A.G., A.P., and P.P. conceptualized and created the models. F.B. and I.V. performed visualization, imaging, and morphological reconstruction of recorded neurons. All the authors participated in writing, reviewing, and editing the manuscript.

Competing interests: The authors declare no competing interests.

Data and materials availability: NEURON simulation files are available at <https://modeldb.yale.edu/254217> for Fig. 3 and fig. S9 and at <https://modeldb.yale.edu/260178> for fig. S12. Reconstructed neurons and all summary graphs with corresponding data are stored at Zenodo (36).

SUPPLEMENTARY MATERIALS

science.sciencemag.org/content/367/6473/83/suppl/DC1
Materials and Methods
Figs. S1 to S12
Tables S1 and S2
References (37–51)

[View/request a protocol for this paper from Bio-protocol.](#)

30 April 2019; accepted 22 November 2019
10.1126/science.aax6239

3.3. Distinct Localization of SNAP47 Protein in GABAergic and Glutamatergic Neurons in the Mouse and the Rat Hippocampus



Distinct Localization of SNAP47 Protein in GABAergic and Glutamatergic Neurons in the Mouse and the Rat Hippocampus

Agnieszka Münster-Wandowski^{1*}, Heike Heilmann¹, Felix Bolduan¹, Thorsten Trimbuch², Yuchio Yanagawa³ and Imre Vida^{1,4*}

¹Institute of Integrative Neuroanatomy, Charité—Universitätsmedizin Berlin, Berlin, Germany, ²Institute of Neurophysiology, Charité—Universitätsmedizin Berlin, Berlin, Germany, ³Departments of Genetic and Behavioral Neuroscience, Gunma University, Graduate School of Medicine, Maebashi City, Japan, ⁴Neurocare Cluster of Excellence, Charité—Universitätsmedizin Berlin, Berlin, Germany

Synaptosomal-associated protein of 47 kDa (SNAP47) isoform is an atypical member of the SNAP family, which does not contribute directly to exocytosis and synaptic vesicle (SV) recycling. Initial characterization of SNAP47 revealed a widespread expression in nervous tissue, but little is known about its cellular and subcellular localization in hippocampal neurons. Therefore, in the present study we applied multiple-immunofluorescence labeling, immuno-electron microscopy and *in situ* hybridization (ISH) and analyzed the localization of SNAP47 in pre- and postsynaptic compartments of glutamatergic and GABAergic neurons in the mouse and rat hippocampus. While the immunofluorescence signal for SNAP47 showed a widespread distribution in both mouse and rat, the labeling pattern was complementary in the two species: in the mouse the immunolabeling was higher over the CA3 *stratum radiatum*, *oriens* and cell body layer. In contrast, in the rat the labeling was stronger over the CA1 neuropil and in the CA3 *stratum lucidum*. Furthermore, in the mouse high somatic labeling for SNAP47 was observed in GABAergic interneurons (INs). On the contrary, in the rat, while most INs were positive, they blended in with the high neuropil labeling. ISH confirmed the high expression of SNAP47 RNA in INs in the mouse. Co-staining for SNAP47 and pre- and postsynaptic markers in the rat revealed a strong co-localization postsynaptically with PSD95 in dendritic spines of pyramidal cells and, to a lesser extent, presynaptically, with ZnT3 and vesicular glutamate transporter 1 (VGLUT1) in glutamatergic terminals such as mossy fiber (MF) boutons. Ultrastructural analysis confirmed the pre- and postsynaptic localization at glutamatergic synapses. Furthermore, in the mouse hippocampus SNAP47 was found to be localized at low levels to dendritic shafts and axon terminals of putative INs forming symmetric synapses, indicating that this protein could be trafficked to both post- and presynaptic sites in both major cell types. These results reveal divergent localization of SNAP47 protein in mouse and rat hippocampus indicating species- and cell type-specific differences. SNAP47 is likely to be involved in unique fusion machinery which is distinct from the one involved in presynaptic neurotransmitter release. Nonetheless, our data suggest that SNAP47 may be involved not only postsynaptic, but also in presynaptic function.

Keywords: SNAP47, hippocampus, GABAergic cells, synaptic localization, mossy fiber projection, immunoelectron microscopy, *in situ* hybridization

OPEN ACCESS

Edited by:

Jackson Cioni Bittencourt,
University of São Paulo, Brazil

Reviewed by:

Françisco E. Olucha-Bordonau,
Jaume I University, Spain
Jon I. Arellano,
Yale School of Medicine,
United States

*Correspondence:

Agnieszka Münster-Wandowski
agnieszka.muenster-
wandowski@charite.de
Imre Vida
imre.vida@charite.de

Received: 06 February 2017

Accepted: 22 June 2017

Published: 13 July 2017

Citation:

Münster-Wandowski A, Heilmann H, Bolduan F, Trimbuch T, Yanagawa Y and Vida I (2017) Distinct Localization of SNAP47 Protein in GABAergic and Glutamatergic Neurons in the Mouse and the Rat Hippocampus. *Front. Neuroanat.* 11:56. doi: 10.3389/fnana.2017.00056

INTRODUCTION

Soluble N-ethylmaleimide-sensitive factor attachment protein (SNAP) receptors, also called SNAREs, play a crucial role in synaptic transmission as central components of the fusion machinery (Südhof, 2004). SNAREs comprise two main groups of conserved membrane-associated proteins: the v-SNAREs (“v” for vesicular) VAMP/synaptobrevins and the t-SNAREs (“t” for target) syntaxins and SNAPs (Hohenstein and Roche, 2001). The SNAP family contains four members: SNAP25 (Jahn et al., 2003; Jahn and Scheller, 2006), SNAP23 (Ravichandran et al., 1996; Wang et al., 1997), SNAP29 (Steggmaier et al., 1998); and Synaptosomal-associated protein of 47 (SNAP47; Holt et al., 2006). SNAP47 is the most recently identified neuronal SNAP which shows a widespread distribution on intracellular membranes, including synaptic vesicles (SVs), but also other intracellular membrane pools in the brain (Holt et al., 2006; Takamori et al., 2006).

The different SNAP isoform proteins display distinct patterns of distribution in different neuronal and non-neuronal populations in the central nervous system (CNS). They are strongly expressed in excitatory (glutamatergic) synapses, pre- as well as postsynaptically. The best characterized SNAP25 and SNAP23 proteins are preferentially and abundantly expressed presynaptically in vesicular glutamate transporter 1 (VGLUT1)-positive excitatory terminals in the hippocampus (Verderio et al., 2004; Garbelli et al., 2008) and in vesicular glutamate transporter 2 (VGLUT2)-positive terminals in the neocortex (Bragina et al., 2007), respectively. It has been also reported that hippocampal and cortical inhibitory interneurons (INs) may selectively express SNAP23 (Verderio et al., 2004; Bragina et al., 2007), however, there is very little data regarding the subcellular localization of specific SNAP isoforms in these neurons. These two SNAP isoforms were also found postsynaptically in spines at substantially lower levels. Although their postsynaptic function has not yet been fully identified, SNAP25 is involved in the regulation of spine formation (Tomasoni et al., 2013) whereas SNAP23 contributes to glutamate receptor trafficking (Suh et al., 2010).

In contrast to SNAP25 and SNAP23, SNAP47 do not contain palmitoylated cysteine clusters, important for the localization to surface membranes. This SNAP, thus, may be involved in intracellular vesicle trafficking and fusion events (Kuster et al., 2015), consistent with a wider subcellular distribution (Holt et al., 2006). Recently, Jurado et al. (2013) documented postsynaptic dendritic localization of SNAP47 and suggested an involvement in postsynaptic fusion events in glutamatergic neurons in the hippocampus. However, SNAP47 is not exclusively localized in postsynaptic structures (Holt et al., 2006). In a recently published study, Shimojo et al. (2015) found endogenous SNAP47 distribution to axons in cortical neuronal cultures, as well as, in native tissue. Thus, existing data suggest both pre- and postsynaptic distribution of this protein, but information regarding the precise subcellular localization of SNAP47 in cortical neurons is still lacking.

Therefore, to address the subcellular distribution of SNAP47 protein and RNA in hippocampal neurons, in this

study we applied immunofluorescent, *in situ* hybridization (ISH) and postembedding immunogold labeling combined with confocal- and electron microscopic analysis in mouse and rat hippocampus with a focus on pre- and postsynaptic elements of glutamatergic and GABAergic neurons.

MATERIALS AND METHODS

Animals

A total of three adult male wild-type (WT) C57BL/6J mice (~2.5-month-old, 25–30 g) and three adult male Wistar rats (~3-month-old, 300–350 g) were obtained from the local animal breeding of the Charité, Berlin. In addition, in order to identify cortical GABAergic INs, we used seven adult male transgenic mice and seven adult male transgenic rats expressing improved yellow fluorescent protein (YFP; Venus) under the promoter of the vesicular GABA-transporter (VGAT) of comparable age and weight. The generation of VGAT-Venus transgenic rats and mice has been described previously (Uematsu et al., 2008; Wang et al., 2009). In these transgenic animals, Venus is expressed highly selectively in 95%–98% of cortical GABAergic INs in the neocortex and the hippocampus. VGAT-Venus transgenic mice and rats exhibit otherwise normal growth and reproductive behavior.

Of these animals, all 10 animals (3 WT and 7 transgenic) of both species were used for immunofluorescence labeling; semi-quantitative analysis of SNAP47 labeling intensities were performed in tissue from three transgenic animals of both species. For immunoelectron microscopic analysis two animals and for ISH also two animals of both species were used. All procedures, animal handling and maintenance were performed in accordance with recommendations of the animal welfare committee of the Charité Berlin, Germany; the National Act on the Use of Experimental Animals, Germany; local authorities (LaGeSo Berlin, registration number: O-0098/12) and the European Council Directive 86/609/EEC.

Tissue Preparation

The animals were anesthetized with a mixture of ketamine 50 mg/kg (Actavis) and xylazine (Rompun) 20 mg/ml (Bayer Health Care, Berlin, Germany) and perfused transcardially with fixative containing 4% paraformaldehyde (PFA, Electron Microscopy Sciences, Hatfield, PA, USA) with 0.2% picric acid (Fluka Chemie, Buchs, Switzerland) in a phosphate buffered solution (0.1 M PB, pH = 7.2). For electron microscopy the fixative contained additionally 0.05%–0.1% glutaraldehyde (GA, Electron Microscopy Sciences). The brains were removed and dissected into blocks containing the hippocampus using a coronal rodent brain matrix (ASI Instruments, Warren, MI, USA) and were processed for light- and electron microscopy. In all experiments, we analyzed 3–5 sections of dorsal hippocampus from each animal.

Primary Antibodies

For a comprehensive list of the antibodies including their characteristics, dilution and source please see **Table 1**. Currently only one full length polyclonal antibody against SNAP47 raised

TABLE 1 | List of primary antibodies for immunocytochemistry.

Antibody	Supplier and cat. no.	Host	Dilution	Immunogen
SNARE protein				
SNAP47	Synaptic System 111 403	Rabbit (polyclonal, affinity purified)	LM 1:300 EM 1:30	Recombinant full length rat SNAP47.
Pre-synaptic glutamatergic marker proteins				
ZnT3	Synaptic System 197 004	Guinea pig (polyclonal, crude antiserum)	LM 1:300	Recombinant protein of mouse ZnT3. (aa 2–75).
VGLUT1	Synaptic System 135 304	Guinea pig (polyclonal, crude antiserum)	LM 1:2000	Purified recombinant protein of rat VGLUT1 (aa 456–560).
Post-synaptic glutamatergic marker protein				
PSD95	UC Davis/NIH NeuroMab Facility 75–028	Clone K28/43 Mouse (monoclonal)	1:100	Fusion protein amino acids 77–299 (PDZ domains 1 and 2 of human PSD95).
GFP/YFP				
GFP	UC Davis/NIH NeuroMab Facility 75–132	Clone N86/38 Mouse (monoclonal)	LM 1:2000 EM 1:100	Green fluorescent protein against fusion protein amino acids 1–238 (full length) of jellyfish green fluorescent protein.

in rabbit is available and was used for all double and triple immunolabeling in our study. The antibody against the SNAP47 protein was first used in a single immunofluorescence analysis to determine the distribution profile of this protein in mouse and rat hippocampus. Double and triple-immunostaining for SNAP47 and several specific GABA and glutamatergic cellular and pre- or postsynaptic markers were used to determine the cellular and compartmental distribution of the SNAP47 protein in hippocampus (see **Table 1**).

Viral Construct, Cell Culture and Western Blotting Verification of SNAP47 Antibody Specificity

Due to limited commercial availability of SNAP47 antibody, we characterized specificity of polyclonal SNAP47 recombinant full length antibody from Synaptic System applying a lentiviral-based method.

Lentiviral Constructs and Virus Production

The coding sequences of mouse SNAP47 (NCBI Reference Sequence NM_144521) and rat SNAP47 (NCBI Reference Sequence: NM_199389) were PCR-amplified from total mouse or rat brain cDNA using custom designed primers: msSNAP47 BsrGI fw (5'-gct gta caa ggg atc cgg aat gag ttc tga tat gcg tgt cc-3'), msSNAP47 AscI rev (5'-aag gcg cgc cct aca tca gct ttc tca tac gc-3'), ratSNAP47 BsrGI fw (5'-gct gta caa ggg atc gga atg agc agt gat gta cga gtt c-3'), ratSNAP47 AscI rev (5'-aag gcg cgc cct aca aca gct ttc tca tac gac-3'). The resulting PCR products were cloned into a modified lentiviral GFP expressing vector (Lois et al., 2002) which would lead to the translation of a N-terminal GFP tagged mouse or rat SNAP47 protein which is controlled by a human Synapsin-1 promoter to restrict neuronal expression. After sequence verification, lentiviral particles were prepared by the Charité Viral Core Facility as described previously (Lois et al., 2002).

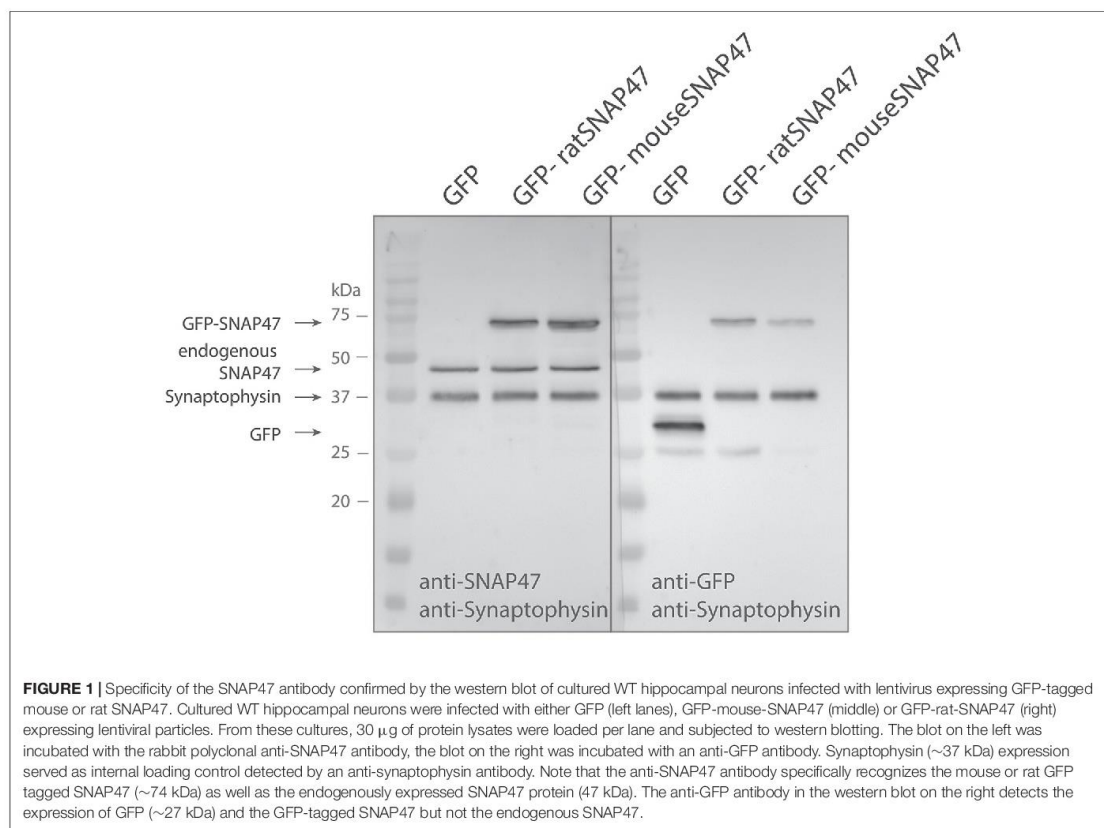
Neuronal Culture and Western Blotting

Murine cell cultures were prepared as described (Chang et al., 2014). Primary hippocampal neurons were prepared from mice on embryonic day E18 and plated at 10,000 cm⁻² on a continental murine astrocyte feeder layer. N-terminally GFP-tagged mouse and rat SNAP47 was lentivirally expressed within murine neuronal cell cultures to validate the SNAP47 antibody. Neurons were infected at DIV 1 with $5 \times 10^5 - 1 \times 10^6$ infectious virus units per 35 mm-diameter well. Protein lysates were obtained at DIV 14. Briefly, cells were lysed using 50 mM Tris/HCl (pH 7.9), 150 mM NaCl, 5 mM EDTA, 1% Triton-X-100, 1% Nonidet P-40, 1% sodium deoxycholate and protease inhibitors (cOmplete protease inhibitor cocktail tablet, Roche Diagnostics GmbH). Proteins were separated by SDS-PAGE and transferred to nitrocellulose membranes. After blocking with 5% milk powder (Carl Roth GmbH) for 1 h at room temperature, membranes were incubated with rabbit anti-SNAP47 (1:1000, Synaptic System 111403), mouse anti-GFP (1:1000, Clontech 632381) and guinea pig anti-Synaptophysin (1:1000, Synaptic System 101004) antibodies overnight at 4°C. After washing and incubation with corresponding horseradish peroxidase-conjugated goat secondary antibodies (all from Jackson ImmunoResearch Laboratories), protein expression levels were visualized with ECL Plus Western Blotting Detection Reagents (GE Healthcare Biosciences).

Anti-SNAP47 recognizes specifically mouse or rat GFP tagged SNAP47 (app. 72 kDa) and endogenously expressed mouse SNAP47 protein (47 kDa), which is not detected in the GFP control western blot (**Figure 1**).

Tissue Processing for Immunofluorescence Labeling

Coronal sections including the hippocampus were cut at 20 μm in a cryostat (CM 3050S; Leica, Wetzlar, Germany). Selected



sections from mouse and rat hippocampus were incubated in a mixture of primary antibodies. The double-labeling antibody combinations were the following: GFP + SNAP47, SNAP47 + PSD95, SNAP47 + gephyrin. The triple-labeling antibody combinations were: GFP + SNAP47 + ZnT3, GFP + SNAP47 + VGLUT1, GFP + SNAP47 + VGAT. For detection of the primary antibodies the sections were subsequently incubated in a mixture of the appropriate secondary antibodies: goat anti-mouse (1:300), goat anti-rabbit (1:500), goat anti-guinea pig (1:500) conjugated to Alexa Fluor series fluorochromes. The immunolabeling protocol was performed as previously described (Booker et al., 2013, 2014). Sections were subsequently mounted in Fluorsave mounting medium (Calbiochem, San Diego, CA, USA), coverslipped and examined using a confocal microscope (FV1000, Olympus, Hamburg, Germany, see below).

Control Experiments

Since no animals deficient of SNAP47 are available, we carefully validated immunolabeling of SNAP47 focusing on proper negative and positive controls. Negative staining controls for all immunofluorescence procedures were performed by substitution of non-immune serum for the primary or secondary antibodies. As positive control we examined immunofluorescence of

SNAP25 protein in hippocampal tissue. To obtain a clear interpretation of the rabbit SNAP47 protein localization, we evaluated first the results of single and double immunostaining for all combinations and compared with those from triple labeling.

RNA *In Situ* Hybridization (ISH)

In the present study, we aimed to characterize the localization, and expression level of SNAP47 in GABA- and glutamatergic neurons in the hippocampus of mice and rats. To this end, we employed ISH and immunocytochemistry. We first assessed the distribution of SNAP47-positive neurons identified by RNA for SNAP47 and the co-localization with the isoform of SNAP47 protein and VGAT-YFP in mouse and rat hippocampus.

Probe Design

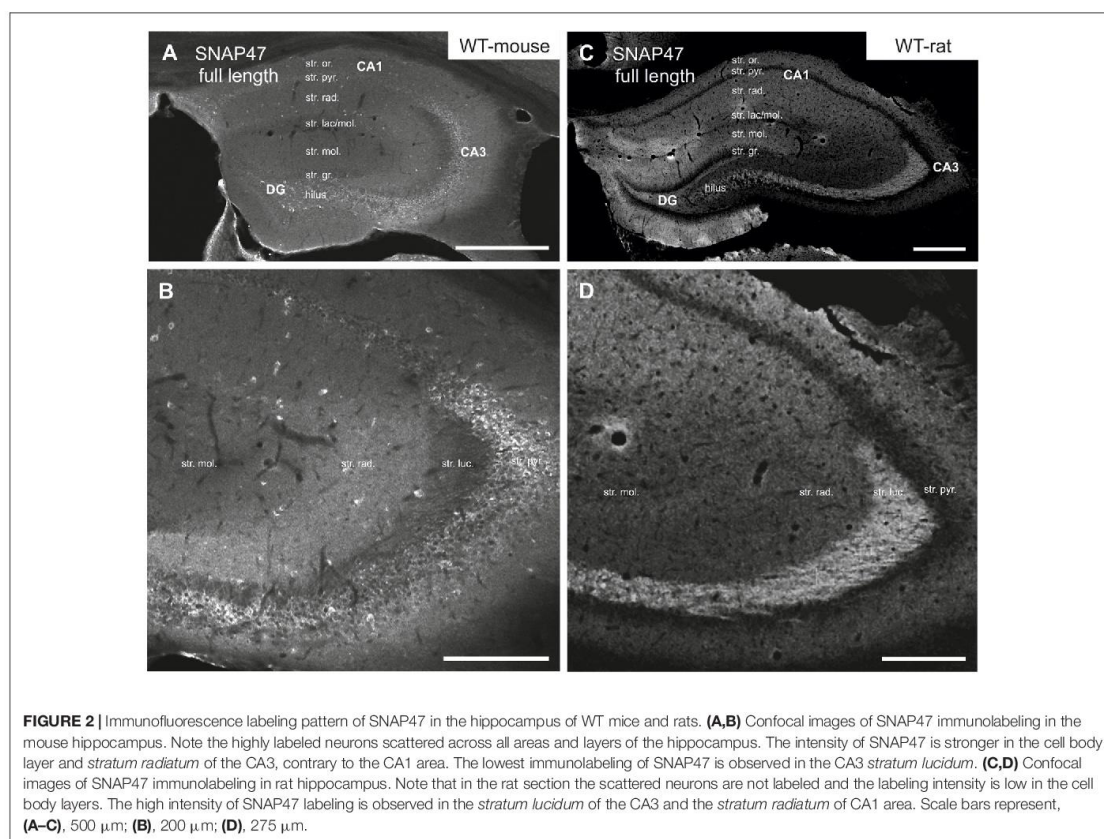
For digoxigenin (DIG) ISH, mice and rat brains were cryoprotected (30% sucrose in TRIS-buffered saline), frozen over liquid nitrogen and cut on a cryostat. DIG *in situ* for SNAP47 RNA expression was performed using a 400 bp DNA fragment which comprised the sequence encoding for Y263 to V395 of the SNAP47 protein in the mouse and V255 to L387 in

the rat. The Fragment was amplified by PCR from the lentiviral SNAP47 expression vector and cloned into plasmids supplied with the T7 promoter sequence (pSPT18/19), and subjected to an *in vitro* DIG RNA labeling using T7-RNA polymerase in the presence of DIG-UTP.

RNA-ISH on Cryosections

Brain sections were washed 5 × 5 min in DEPC-PBS to clear cryoprotectant, and dried at 50°C. Next the slices were postfixed in 4% PFA, washed in DEPC-PBS. Then they were acetylated in 0.25% acetic anhydride in 0.1 M triethanolamine-HCl (pH = 8.0) for 10 min and treated with Proteinase K to inactivate rare-cutting restriction enzymes. Sections were pre-hybridized for 15 min at RT in hybridization buffer containing 0.3 M NaCl, 10% Dextran sulfate, 0.02 M Tris (pH = 8.0), 5 mM EDTA (pH = 8.0), 1 × Denhardt's solution, 0.5 mg/ml tRNA, 50% deionized formamide. Following pre-hybridization, they were hybridized by incubating in hybridization buffer containing a DIG-labeled probe for SNAP47 (total conc. 50 ng/μl; 12–20 ng/slice) at 54°C overnight. Post-hybridization washes were performed sequentially 5 × 5 min at 54°C in 5 × SSC containing 0.05%

Tween at 54°C; 5 × 10 min in 50% formamide/2 × SSC at 54°C; 5 × 10 min in 50% formamide/1 × SSC at 54°C; 3 × 5 min in 0.1 × SSC at 54°C; 3 × 5 min in 0.1 × SSC at RT; 4 × 5 min 1 × Tris Puffer containing 0.05% Tween at RT. Next, the slices were incubated for 1 h in blocking buffer containing 4% sheep serum and 1% milk powder, followed by incubating overnight at 4°C with sheep anti-DIG-AP Fab fragment (Roche, Basel, Switzerland) diluted 1:2000 in blocking buffer. The color development of alkaline phosphatase activity was in the presence of two substrates: of 5-bromo-4-chloro-3-indolyl phosphate (BCIP) and nitroblue tetrazolium (NBT), was controlled under RT and stopped by adding in 1 × PBS. After washing overnight in 1 × PBS, sections were mounted onto slides using Kaisers-Gelantine (Merk, Kat. Nr. 1.09242.0100), coverslipped and examined using an Olympus Microscope and the Metamorph Software. To better compare the distribution of ISH signal to the immunolabeling pattern, sections for ISH were interleaved with section which were processed for immunolabeling for GFP and SNAP47 and examined as described above in "Tissue Processing for Immunofluorescence Labeling" Section.



Specificity of Hybridization Probes and the Anti-DIG-AP Antibody

As controls, hybridization with sense probes for mouse and rat and omission of the anti-DIG-AP antibody completely abolished ISH signals and immunoreactivity.

Confocal Imaging and Quantitative Analysis

In order to get an overview of SNAP47 distribution over the mouse and rat hippocampus, we imaged the 20 μm thick coronal hippocampal sections using an $\times 4$ objective lens on a confocal laser-scanning microscope (Olympus FV1000) and arranged overview images. Higher-resolution images were acquired using an $\times 60$ silicon oil immersion lens, with a zoom factor of either 1 or 4 to resolve individual pre- and postsynaptic puncta. Excitation wavelengths were 488 nm for anti-mouse Alexa Fluor-488 (Invitrogen), 405 nm for anti-guinea pig Alexa Fluor-405 (Jackson Immuno Research, West Grove, PA, USA), 643 nm for anti-rabbit Alexa Fluor-647 (Life Technologies, Darmstadt, Germany) and 515 nm for YFP (Nagai et al., 2002), respectively. The images were acquired through separate channels and temporally non-overlapping excitation of the fluorochromes and analyzed off-line using ImageJ software package (courtesy of W.S. Rasband, U. S. National Institutes of Health, Bethesda, Maryland¹). The analysis of co-localization was performed in Fiji/ImageJ software based on the isodata algorithm (Ridler and Calvard, 1978) using the auto-threshold plugin.

For the semi-quantitative analysis of SNAP47 proteins in GABAergic neurons of mouse and rat hippocampus, we used three VGAT-Venus transgenic mice and rats from three different litters. Confocal images (nine stacks of each hippocampus) were taken using $\times 30$ objective and analyzed by counting the number of VGAT-Venus positive neurons which were also positive for SNAP47 fluorescence. To compare SNAP47 fluorescence signal intensity in GABAergic INs between mouse and rat hippocampus, we determined the mean labeling intensity over the somata (excluding nucleus) of VGAT-positive neurons and compared these to the mean labeling intensity of the surrounding neuropil in the mouse and the rat hippocampus, respectively. All image processing and analysis were performed using Fiji/ImageJ.

Electron Microscopy

In order to identify the precise subcellular localization of SNAP47 protein in mouse and rat hippocampal neuron, we combined freeze substitution, low temperature embedding and postembedding immunogold labeling.

Freeze Substitution Embedding

One millimeter thick hippocampal slices were cut from previously perfused brains and washed repeatedly (six times 10 min) in 0.1 M PB at pH = 7.2. The slices were cryoprotected with increasing concentrations of saccharose (0.5–2.3 M) dissolved in PB. The tissue was subsequently frozen by plunging

it into liquid nitrogen. The samples were then transferred into cold methanol (-90°C) in a freeze-substitution chamber (Leica EM AFS). The methanol was exchanged three times before the specimens were immersed overnight in anhydrous methanol at -90°C , containing 2% (w/v) uranyl acetate (Merck, Darmstadt, Germany). After rinsing several times with methanol, the temperature was gradually raised to -50°C and left overnight. The tissue was then infiltrated with mixtures of Lowicryl HM20 resin (Polysciences, Hirschberg, Germany) and methanol (at proportions of 1:2; 1:1; 2:1, respectively, 1 h each) and finally left in pure resin overnight at -50°C . The samples were transferred to flat embedding molds containing freshly prepared resin at -50°C . UV polymerization was started at -50°C (overnight) and then continued for several days at temperatures gradually increasing from -50°C to -20°C and finally to 20°C . Ultrathin sections (70 nm) were cut on a microtome (Reichert Ultracut S, Leica) and mounted on 200-mesh Formvar-coated nickel grids (Plano, Wetzlar, Germany).

Postembedding Immunogold Labeling

All postembedding steps except for the incubation with primary antibodies were performed at room temperature. For single and double immunolabeling with SNAP47 antibody, sections were first incubated two times for 5 min in 0.1 M PBXT (PBS, 0.001% Triton X-100, 0.001% Tween 20, pH = 7.4), followed by 90 min incubation in PBXT supplemented with 2% bovine serum albumin (BSA, Sigma-Aldrich, Darmstadt, Germany) and 5% normal goat serum (NGS; PAN Biotech) at room temperature. The sections were next incubated with primary antibodies diluted in the same buffer overnight at 4°C in a humid chamber. After rinsing several times with PBXT, the binding of primary antibodies was visualized by incubating with goat anti-rabbit or goat anti-guinea pig secondary antibodies conjugated to either 5 or 10 nm gold particles (British BioCell, International, Wetzlar, Germany) in PBXT supplemented with 0.5% acetylated BSA (Aurion, Wageningen, Netherlands), for 90 min in a humid chamber. Grids were rinsed several times in PBXT, PBS, and finally in water. Ultrathin sections were finally stained with 2% aqueous uranyl acetate (Merck, Darmstadt, Germany) for 2 min, and with lead citrate for 30 s. Sections were examined using a Zeiss TEM-912 equipped with a digital camera (Proscan 2K Slow-Scan CCD-Camera, Zeiss, Oberkochen, Germany). For negative controls, primary antibodies were omitted.

Quantification of Immunogold Signals

Hippocampal sections embedded in Lowicryl HM20, from two animals, were incubated with the rabbit anti-SNAP47 antibody, and immunogold labeling was detected by secondary goat anti-rabbit antibody coupled to 10 nm gold particles. Quantification was performed using the iTEM software (Olympus GmbH, Münster, Germany). The numbers of gold particles were counted within the defined Region of Interest (ROI) area of two populations of glutamatergic synapses in CA3 region of hippocampus: (1) Mossy fiber boutons (MFBs) and their postsynaptic partners, the CA3 complex spines in *stratum lucidum*; and (2) small boutons and

¹<http://rsb.info.nih.gov/ij/>

spines forming asymmetric synapses in *stratum radiatum*. Immunopositive (threshold of two gold particles) and negative synaptic compartments were included in the analysis. Density values were finally calculated as the number of gold particles per section area in μm^2 . The labeling density was comparable in two animals. Non-specific labeling (background) was assessed from mitochondria. In MFBs most mitochondria (91.7%) showed no immunogold particles and the rest only a single gold particles. The mean particle density was 2.9 ± 0.8 particle/ μm^2 (204 mitochondria from two animals with an average area of 0.03 ± 0.002 μm^2). Similarly in the CA3 *stratum radiatum*, the majority of the mitochondria (90%) showed no immunolabeling at all, 10% had only a single particle and the mean density was 2.5 ± 0.8 particle/ μm^2 (100 mitochondria from two animals with an average area of 0.05 ± 0.004 μm^2).

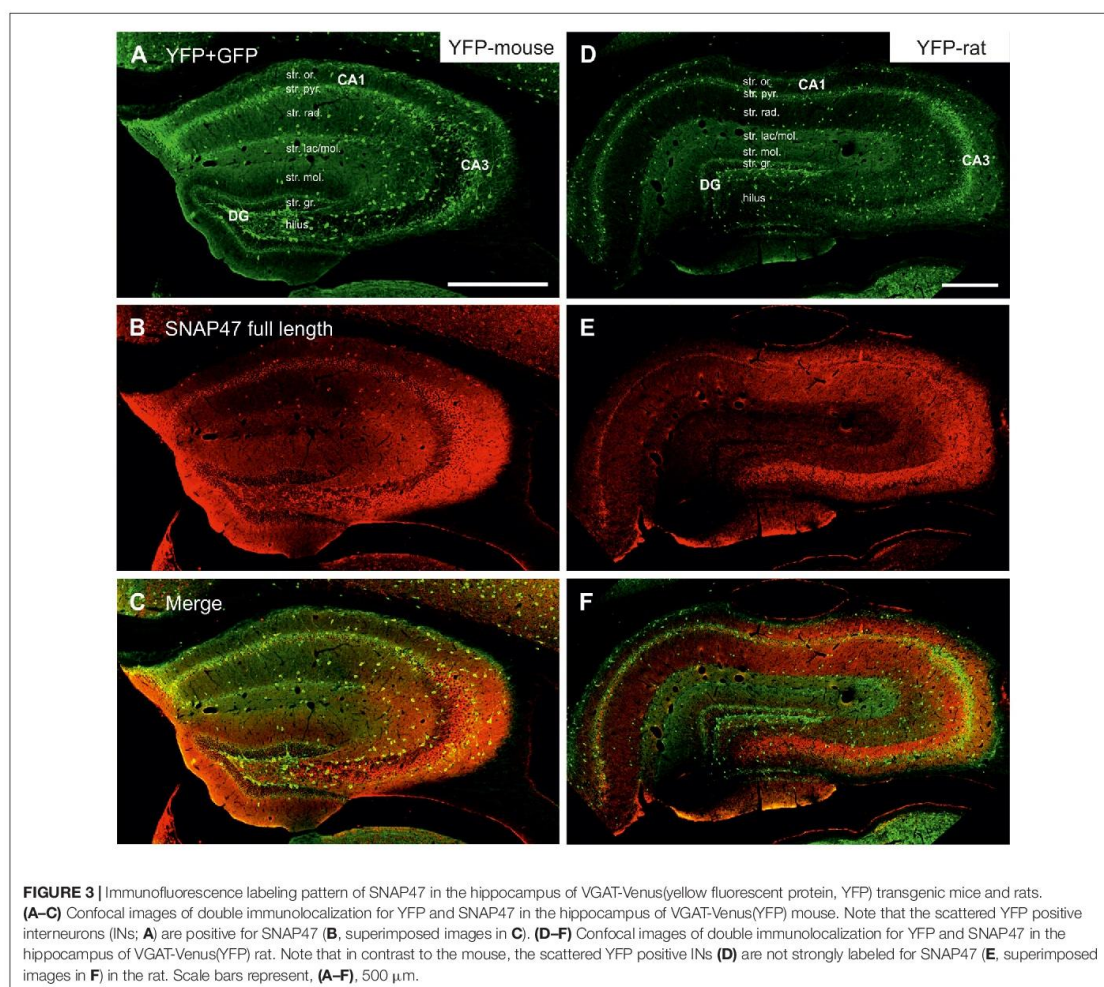
Statistical Analysis

The immunogold particle density over presynaptic boutons, postsynaptic spines and mitochondria (serving as background control), from the *stratum lucidum* and *radiatum* was compared by non-parametric Mann-Whitney test for comparing two group rank differences. Data are reported as mean \pm standard error of the mean (SEM). Between-subjects comparisons were considered significant if the *P* value was <0.05 .

RESULTS

General Distribution Pattern of SNAP47 in the Mouse and the Rat Hippocampus

In order to investigate the cellular localization of SNAP47 in the hippocampus, we first performed immunofluorescence



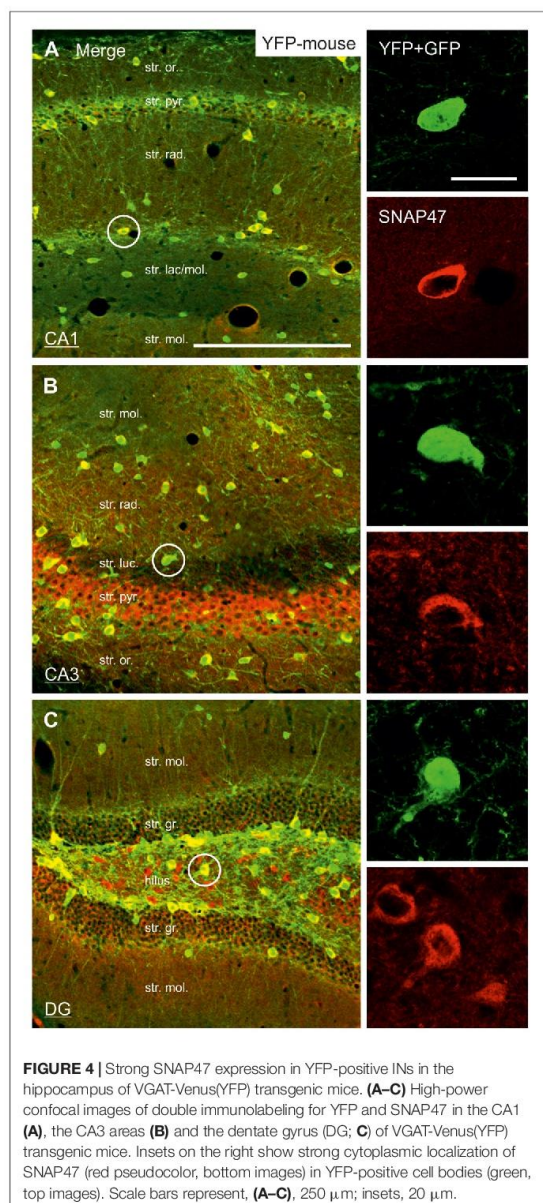


FIGURE 4 | Strong SNAP47 expression in YFP-positive INs in the hippocampus of VGAT-Venus(YFP) transgenic mice. **(A–C)** High-power confocal images of double immunolabeling for YFP and SNAP47 in the CA1 **(A)**, the CA3 areas **(B)** and the dentate gyrus (DG; **C**) of VGAT-Venus(YFP) transgenic mice. Insets on the right show strong cytoplasmic localization of SNAP47 (red pseudocolor, bottom images) in YFP-positive cell bodies (green, top images). Scale bars represent, **(A–C)**, 250 μm ; insets, 20 μm .

labeling in sections from perfusion-fixed WT mouse and rat brains. The immunolabeling revealed a broad distribution of the protein in hippocampal areas and layers in both species; however, the pattern of SNAP47 distribution was divergent.

In the mouse, stronger SNAP47 immunolabeling was observed over the CA3 *stratum radiatum*, *oriens* and the pyramidal cell layer **(Figures 2A,B)**, whereas the *stratum lucidum*

TABLE 2 | Summary of the SNAP47 protein distribution according to regions and layers in the mouse and the rat hippocampus (SNAP47 immunoreactivity: +++, strong; ++, moderate; +, weak; –, virtually absent).

Hippocampus		Mouse	Rat
Region	Layer		
CA1	oriens	+	++
	pyramidale	++	–
	radiatum	+	++
	lacunosum	+	+
CA3	oriens	++	+
	pyramidale	+++	–
	lucidum	+	+++
	radiatum	++	+
	lacunosum	+	+
DG	molecular layer	+	++
	granular cells	+	–
	hilus	++ (cell bodies)	++
INs		++	+/-

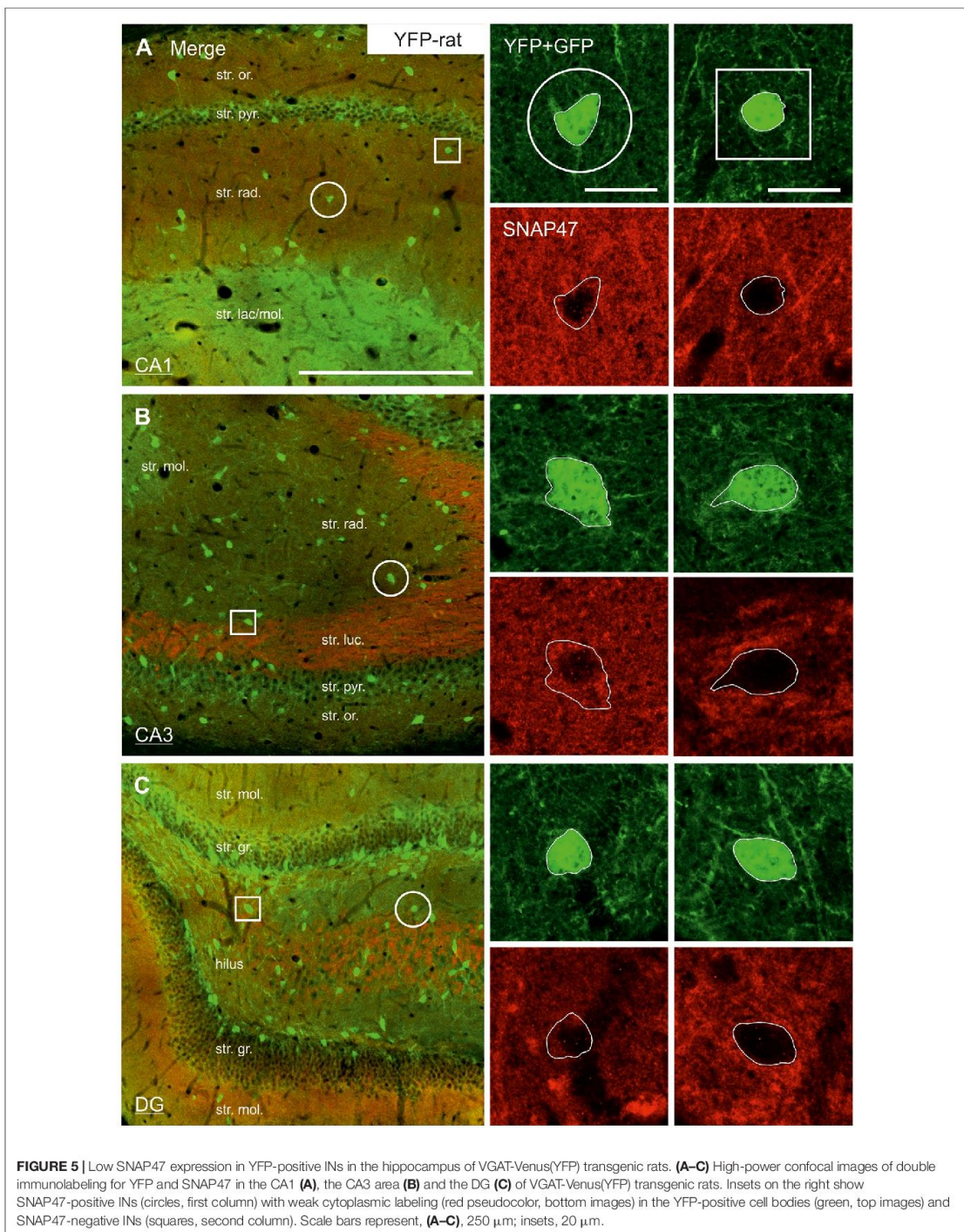
was weakly labeled **(Figures 2A,B)**. In contrast in the CA1 region neuropil labeling in *stratum radiatum* and *oriens* was weak **(Figures 2A,B)**. Finally, in the dentate gyrus (DG) labeling intensity was intermediate with a slightly higher labeling at the border between the molecular and granular cell layers **(Figure 2A)**. Additionally, scattered cell bodies of putative GABAergic INs strongly labeled for SNAP47 could be observed in all areas and layers of the hippocampus **(Figures 2A,B)**.

Intriguingly, SNAP47 showed different and almost complementary labeling pattern in the rat hippocampus. The immunolabeling signal was particularly strong in the CA3 *stratum lucidum* and the hilus of the DG **(Figures 2C,D)** suggesting that the synapses formed by the glutamatergic mossy fiber (MF) projection contains high level of associated SNAP47 protein. In contrast, the CA3 pyramidal cell layer and *stratum radiatum* were less strongly labeled when compared to the mouse. In the CA1 area, the labeling was much stronger over the neuropil in *stratum radiatum* and *oriens* **(Figures 2C,D)**. Slightly stronger labeling was present in the molecular layer of DG, whereas the granular cell layer was weakly labeled **(Figure 2C)**. Finally, in contrast to mouse, the labeling of scattered INs was absent in the rat hippocampus **(Figures 2C,D)**.

In summary, the labeling for SNAP47 is stronger in the cell body layers and interneuron somata of the mouse hippocampus, suggesting a preferential somatic and postsynaptic localization of this protein in this species. In the rat it showed overall stronger neuropil labeling suggesting preferential localization to the neuronal processes. The complementary distribution of SNAP47 in the mouse and in the rat is semi-quantitatively summarized in **Table 2**.

SNAP47 Co-Localizes with GABAergic INs

The strong labeling of scattered cell bodies in all hippocampal areas and layers in WT mouse suggested high expression of SNAP47 protein in GABAergic INs. In order to confirm this hypothesis, we took advantage of the VGAT-YFP transgenic mouse and rat line selectively expressing YFP-Venus in INs under the VGAT promoter and performed labeling for



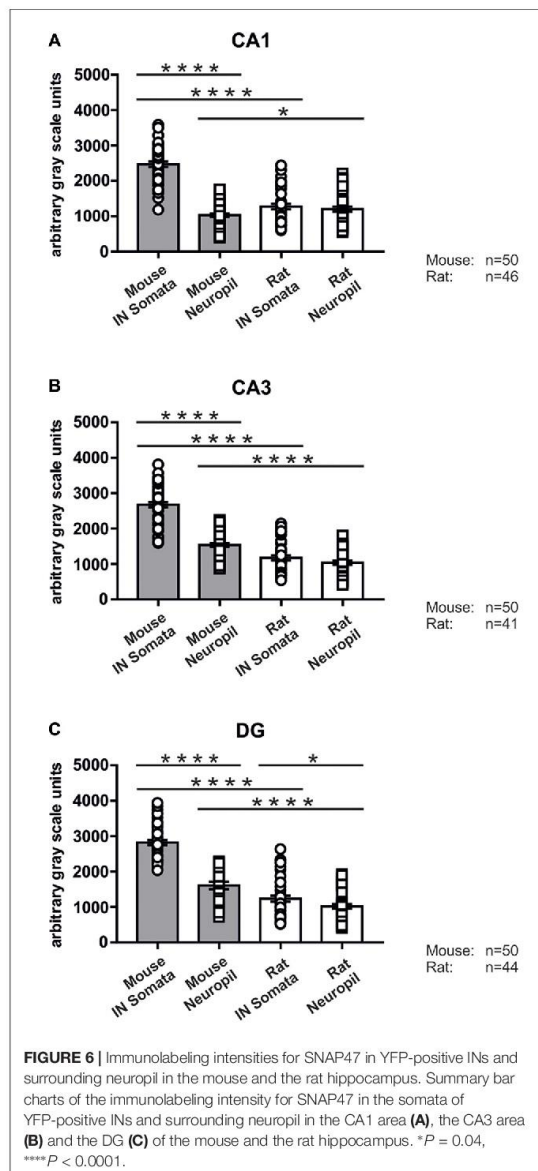
SNAP47 in these transgenic lines (Uematsu et al., 2008; Wang et al., 2009).

High Expression of SNAP47 Protein in VGAT-Positive INs in the Mouse Hippocampus

In good agreement with the labeling observed in the WT mouse, we saw low SNAP47-labeling in the neuropil of the CA1 area (Figures 3B,C, 4A) and *stratum lucidum* of the CA3 (Figures 3B,C, 4B), whereas the labeling was high in the CA3 *stratum radiatum* (Figure 4B), *moleculare* and *pyramidale*, as well as the dentate hilus in sections from transgenic mice (Figures 3B,C, 4C). To facilitate the identification of GABAergic neurons, the YFP signal was amplified by immunostaining using an anti-GFP antibody. In all areas and layers of the hippocampus scattered INs were labeled for YFP (Figure 3C, Supplementary Figure S1) as reported previously (Wang et al., 2009). SNAP47 labeling showed a strong overlap in the somatic cytoplasm of YFP-positive INs (Figures 3A–C, 4A–C and insets). Quantitative data confirmed this observation: in a sample of 537 YFP-positive neurons of the dorsal hippocampi in both hemispheres from three animals essentially all INs were found to be immunopositive for SNAP47. When the mean intensity (arbitrary gray scale units) was assessed in the cytoplasm of YFP-positive cell bodies in the mouse, YFP-positive cell bodies had an almost two-fold higher (239%) mean labeling intensity (2470 ± 76 grayscale value, 50 cells, Figure 6) than the surrounding neuropil in the CA1 *stratum radiatum* (1032 ± 45 , Figure 4A with inset, 6A). In the CA3 and the dentate hilus of the mouse, similarly high difference was found between the somatic SNAP47 labeling intensity of YFP-positive cell bodies and the surrounding neuropil (Figures 4B,C with insets, 6B,C).

Low SNAP47 Immunoreactivity in VGAT-Positive INs in the Rat Hippocampus

The lack of the prominent labeling of putative INs in the rat raises the question whether they are devoid of SNAP47. In order to answer this question, we have performed double immunolabeling in a VGAT-YFP transgenic rat line. In good agreement with the labeling in the WT rat and in contrast to that in the mouse, we observed high and homogeneous neuropil labeling in all areas, particularly in the CA1 area of transgenic rats (Figures 3E,F, Supplementary Figure S2). Over the strongly labeled neuropil we could not detect the scattered somata of INs, neither as a higher, positive nor as a lower, negative signal (Figures 3D,E). The expression of SNAP47 in VGAT-positive neurons in the rat was, thus, weaker than in the mouse, but still detectable in most of the INs at a level comparable to the labeling intensity of the surrounding neuropil (Figure 5, insets). Indeed, we found that in the majority of YFP-positive cells (96%, 459 of total 479 cell bodies; from both hippocampi of three animals) showed SNAP47-positive signal in their cytoplasm, only the nucleus was negative (Figure 5, insets panel with circle). When the mean intensity was assessed in the cytoplasm of YFP-positive cell bodies in the rat, it was on average only 6% higher (1275 ± 80 grayscale value, 46 cells, Figure 6A), than the intensity of the surrounding neuropil in the CA1 *stratum radiatum* (1203 ± 72 , Figure 5A with



insets panel with circle and 6). In other areas, the CA3 and the dentate hilus, similar low difference was found between the SNAP47 labeling intensity in YFP-positive cell bodies and the surrounding neuropil (Figures 5B,C and insets panel with circle, 6B,C), despite the differences in labeling intensities of the neuropil among the areas.

In conclusion, the labeling of the neuropil in the rat obscured the labeling of the cells and made their identification in the SNAP47 labeling difficult. Nevertheless our data indicate that

in the mouse essentially all and in the rat hippocampus most INs express SNAP47, however the labeling intensity was strongly different between these two rodent species.

SNAP47 RNA-Expressing INs in the Mouse and the Rat Hippocampus

ISH showed intense cellular expression pattern of SNAP47 RNA in the mouse hippocampus (Figure 7A, Supplementary Figure S3). The pyramidal cell layer in CA1 and CA3 as well as the granular cell layer of DG displayed strong reaction (Figure 7A). We further observed SNAP47 RNA labeling in scattered neurons over all areas and layers of the hippocampus, consistent with the labeling of GABAergic INs (Figure 7A). The highly similar cellular distribution of SNAP47 RNA and the protein in GABAergic cells were confirmed in consecutive slices double-immunolabeled for GFP and SNAP47 (Figures 7D–F).

In the rat, the expression pattern of SNAP47 RNA was generally weaker compared to the mouse. All areas and layers, in particular the cell body layers, showed much lower RNA expression (Figure 7B).

The sense probes used to detect non-specific hybridization exhibited only very low background level of hybridization signal (Figure 7C).

In summary, ISH complemented our immunocytochemical approach and further highlighted: (1) the expression of SNAP47 in principal cells and GABAergic neurons in the mouse hippocampus; and (2) the divergent cellular expression in the mouse and the rat hippocampus.

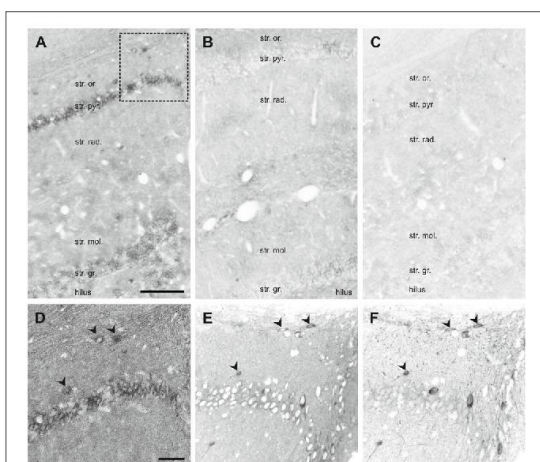


FIGURE 7 | *In situ* hybridization (ISH) of SNAP47 RNA in the mouse and the rat hippocampus. (A,B) Overview images ISH with anti-sense probes in mouse (A) and rat (B) hippocampus. (C) ISH image with sense probe in mouse hippocampus. (D) Higher magnification images of ISH signal in the *stratum oriens*, *pyramidale* and *radiatum* of the mouse CA1 area indicated by a box in (A). (E,F) Higher magnification images of an adjacent section with double immunofluorescence labeling for SNAP47 (E) and GFP (F) shown as separate channels and inverted to grayscale. Scale bar represents 100 μ m in (A–F).

SNAP47 Immunoreactivity is Present Both Pre- and Postsynaptically in the Mossy Fiber Projection System

In order to determine whether the high labeling observed in the rat CA3 *stratum lucidum* (Figures 3E,F, 5B) was localized to pre- or postsynaptic elements, we have next performed double labeling for SNAP47 and the Zn-transporter 3 (ZnT3) as a presynaptic marker, known to be highly enriched in MFs and their terminals (Wenzel et al., 1997) or PSD95 as a postsynaptic marker (Kornau et al., 1995; Müller et al., 1996; Rao et al., 1998; Buckby et al., 2004) to identify the complex spines of CA3 pyramidal cells present in this layer.

Pre- and Postsynaptic Labeling for SNAP47 in the Mossy Fiber Projection System in the Rat

In sections double stained for SNAP47 and ZnT3 (Figure 8B), ZnT3 showed a strong labeling in the CA3 *stratum lucidum* (Figure 8B) and the hilus was particularly strong at locations where MFs were in close contact with somata and dendrites of CA3 pyramidal cells or putative hilar mossy cells. SNAP47 and ZnT3 labeling showed a partially overlapping pattern, indicating that SNAP47 was present presynaptically in MFs in the rat hippocampus (Figure 8B). To confirm the results, we additionally performed double-immunolabeling for SNAP47 and VGLUT1, the most abundant presynaptic vesicular marker for glutamatergic synapses (Alonso-Nanclares et al., 2004). Indeed, we detected overlapping signals for VGLUT1 and SNAP47 in the MF termination zone in the CA3 *stratum lucidum* and the hilus of the rat (Figure 8D). In sections double-labeled for SNAP47 and PSD95, we observed a stronger overlap in the *stratum lucidum* and also in *stratum radiatum* of the CA3 (Figure 9B) as well as in the neuropil of the CA1 area, reflecting a preferential postsynaptic localization of the protein in both the MFB and the commissural/associational fiber systems of the rat.

Predominant Postsynaptic Labeling for SNAP47 in the Mossy Fiber Projection System in the Mouse

In contrast to the rat, the labeling for SNAP47 was low in the CA3 *stratum lucidum* of the mouse hippocampus. Accordingly, we found little co-localization of SNAP47 with ZnT3 (Figure 8A) or VGLUT1 presynaptically in MFs (Figure 8C). Postsynaptically, however, SNAP47 showed a clear co-localization with PSD95 in the CA3 *stratum lucidum* of the mouse (Figure 9A). Furthermore, consistent with the stronger labeling intensity for SNAP47 in the CA3 *stratum radiatum* (Figure 8A), we found substantial colocalization of SNAP47 and PSD95 in this layer of the mouse hippocampus (Figure 9A). Similarly, colocalization of SNAP47 and PSD95 was strong in the CA1 *stratum radiatum*, too.

Subcellular Localization of SNAP47

On the basis of our light microscopic analysis two major observations emerged: (1) SNAP47 is expressed at high levels in VGAT-positive inhibitory neurons in the adult mouse hippocampus; (2) in the rat hippocampus, the highest level of the immunolabeling was observed in excitatory MF system in putative postsynaptic elements. In order to confirm

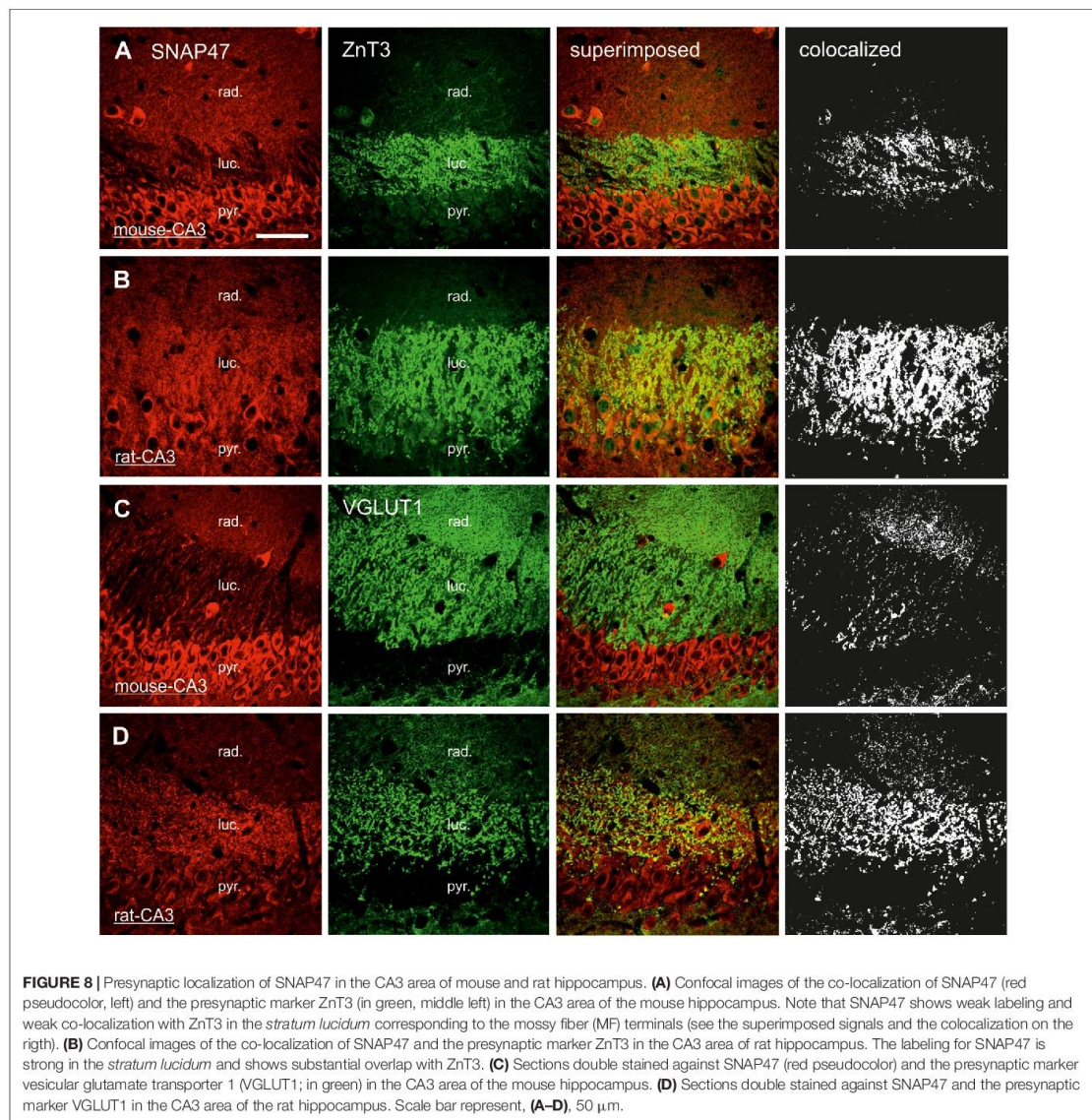


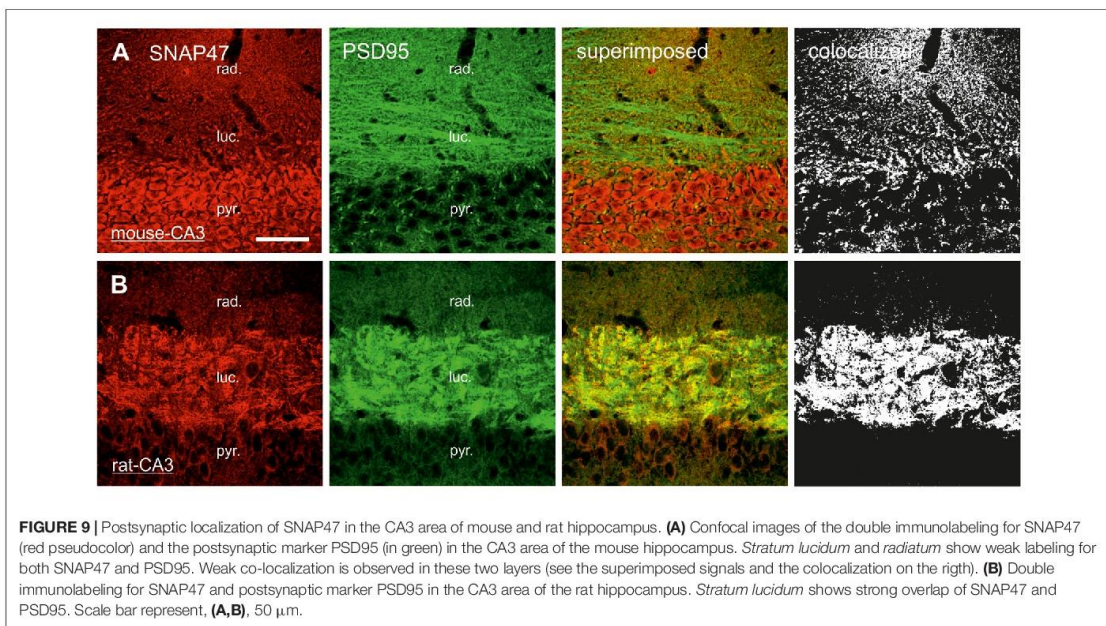
FIGURE 8 | Presynaptic localization of SNAP47 in the CA3 area of mouse and rat hippocampus. **(A)** Confocal images of the co-localization of SNAP47 (red pseudocolor, left) and the presynaptic marker ZnT3 (in green, middle left) in the CA3 area of the mouse hippocampus. Note that SNAP47 shows weak labeling and weak co-localization with ZnT3 in the *stratum lucidum* corresponding to the mossy fiber (MF) terminals (see the superimposed signals and the colocalization on the right). **(B)** Confocal images of the co-localization of SNAP47 and the presynaptic marker ZnT3 in the CA3 area of rat hippocampus. The labeling for SNAP47 is strong in the *stratum lucidum* and shows substantial overlap with ZnT3. **(C)** Sections double stained against SNAP47 (red pseudocolor) and the presynaptic marker vesicular glutamate transporter 1 (VGLUT1; in green) in the CA3 area of the mouse hippocampus. **(D)** Sections double stained against SNAP47 and the presynaptic marker VGLUT1 in the CA3 area of the rat hippocampus. Scale bar represent, **(A–D)**, 50 μm .

and further refine our confocal-microscopy observations, we have next performed postembedding immunogold labeling for SNAP47 combined with quantitative electron microscopic analysis.

Subcellular Localization of SNAP47 to Post- and Presynaptic Components of Glutamatergic MF Projection in the Rat Hippocampus

In order to determine whether SNAP47 can, indeed, be localized to post- as well as presynaptic glutamatergic elements, as

suggested by our immunofluorescence results, we next examined the MF projection in the rat hippocampus. MF boutons and their postsynaptic elements, the complex spines of CA3 pyramidal cells were identified on the basis of their ultrastructural features and localization in the *stratum lucidum*. MFs show typical morphological characteristics, namely large presynaptic surface area, densely packed, clear, sphere-shaped SVs; a low number of dense core vesicles (DCVs); numerous mitochondria; numerous contacts with complex spines and *puncta adherentia* onto dendritic shafts (Frotscher et al., 1994). In ultrathin sections of



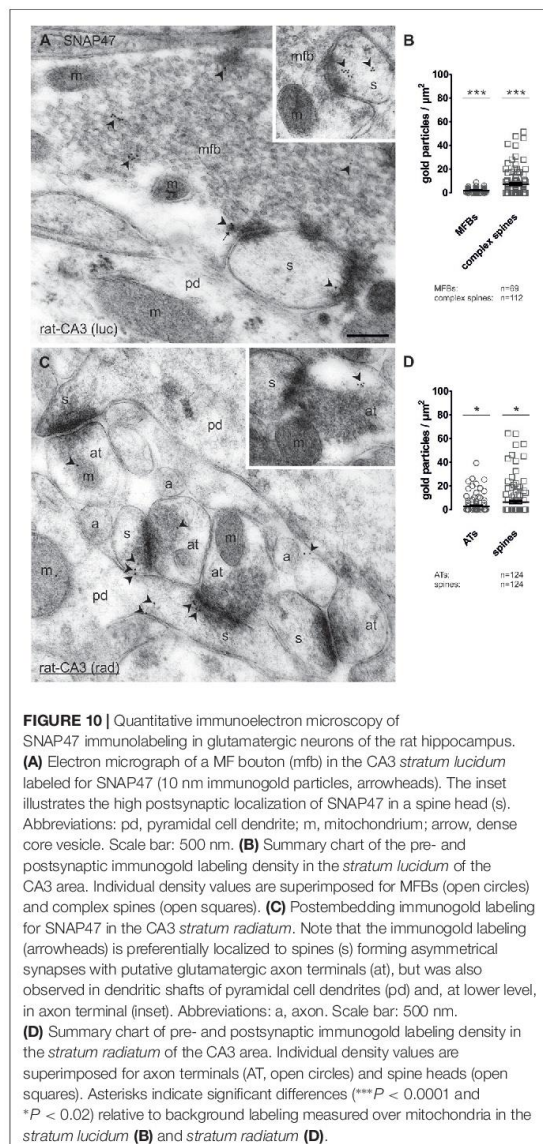
CA3 *stratum lucidum*, immunogold-labeling for SNAP47 were present at high levels in complex spines engulfed by MFBs (Figure 10A and inset). However, the immunogold labeling was not confined to spines, but was also present in dendritic shafts, albeit at lower density. Furthermore, immunogold labeling was present presynaptically in MFBs in areas in close apposition to postsynaptic surface membranes of CA3 pyramidal cell dendrites, though at substantially lower density than on the postsynaptic side (Figure 10A). The labeling density was highly variable between MFBs (0–26 gold particles per MFB profile) and the distributions pattern of SNAP47 within MFBs seemed to be inhomogeneous, with clusters of immunogold particles associated to membrane structures within SV pools (Figure 10A).

Quantification of the labeling intensity confirmed these qualitative observations indicating that 19.7% of complex spines were clearly immunopositive (>2 particles per profile) with up to 15 gold particles per spine. In contrast, 33.9% of complex spines showed only 1–2 particles per profile and 46.4% were not labeled at all. The average density of immunogold particles was 7.4 ± 1.0 particle/ μm^2 over all complex spines (112 spines from two animals with an average area of 0.21 ± 0.02 μm^2 ; Figure 10B). Presynaptically 76.9% were immunopositive (>2 particles per bouton), 13.4% of the MFBs showed labeling with 1–2 particles per bouton and 10.1% had no immunolabeling at all. Despite the high proportion of clearly immunopositive terminals, the mean labeling intensity with 2.1 ± 0.2 particle/ μm^2 (69 MFBs from two animals, mean cross-section area 3.28 ± 0.18 μm^2 , Figure 10B) was three-times lower than postsynaptically in complex spines. The density of immunogold particles

measured in both pre- and postsynaptic compartments was significantly higher compared to the background ($P < 0.0001$ for both compartments; Figure 10B) measured over mitochondria in MFBs.

To further test whether the strong, but sparse postsynaptic localization of SNAP47 applied to other glutamatergic synapses, we also took samples of small glutamatergic boutons in *stratum radiatum* of the CA3 area. These asymmetrical synapses were identified by the close apposition of a small presynaptic boutons filled with small clear SVs and a postsynaptic dendritic spine with strong postsynaptic density (PSD) separated by a well-defined synaptic cleft (Figure 10C and inset). At these synapses gold labeling was much lower than in MFBs and was present only in a total of 6.5% (≥ 2 particles per profile) postsynaptically and 9.7% (≥ 2 particles per bouton) presynaptically. The mean density of immunogold particles postsynaptically, in spines was 6.2 ± 1.3 particle/ μm^2 (124 spines from two animals with an average area of 0.06 ± 0.004 μm^2 ; Figure 10D) whereas it was two-times lower at 2.8 ± 0.6 particle/ μm^2 presynaptically, in small putative glutamatergic axon terminals (124 terminals from two animals with an average area of 0.14 ± 0.01 μm^2 ; Figure 10D). The density of immunogold particles postsynaptically ($P = 0.0101$) and presynaptically ($P = 0.0151$; Figure 10D) was significantly higher than the background obtained over mitochondria in the *stratum radiatum*.

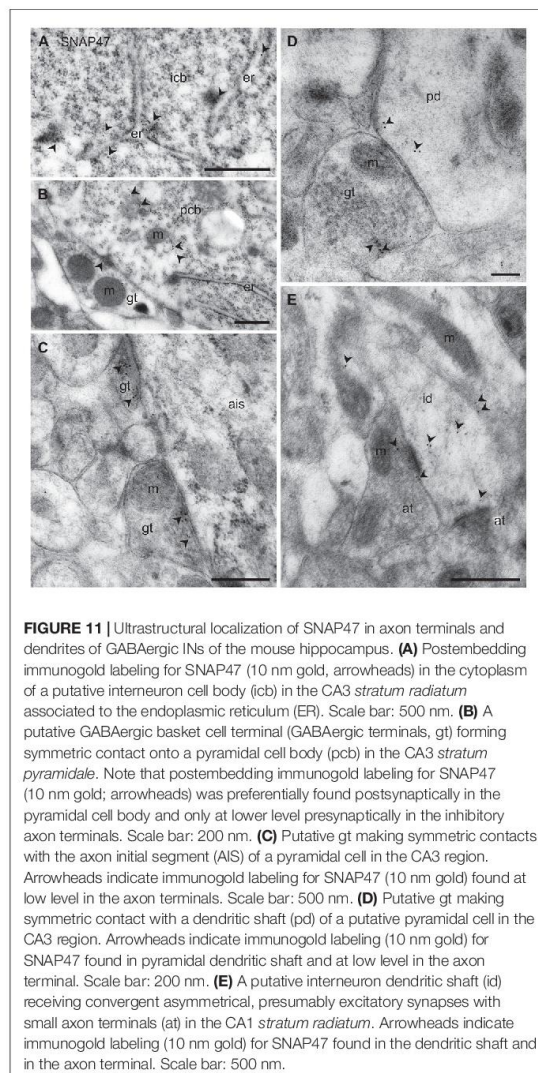
In summary, our quantification documented an enrichment of SNAP47 postsynaptically in spines and additionally revealed quantitative differences in the expression across the layers of the CA3 area, with higher labeling present in complex spines in the *stratum lucidum* as opposed to small dendritic



spines in the *stratum radiatum*. Moreover, labeling for SNAP47 was clearly present in most presynaptic terminals examined, but at a level lower than that detected in postsynaptic compartments.

Subcellular Localization of SNAP47 to Post- and Presynaptic Components of GABAergic INs in the Mouse

Consistent with the strong immunofluorescence labeling for SNAP47 in VGAT-Venus INs in the mouse hippocampus,



immuno-electron microscopy showed high levels of immunogold particles for the protein at the membrane of the endoplasmic reticulum (ER) in cell bodies of VGAT-positive INs (Figure 11A). Similar to INs, somata of putative PCs in the CA1 *stratum pyramidale* showed high levels of immunogold particles associated to the ER (Figure 11B). This localization plausibly reflects a reserve pool, related to production and trafficking of the protein in these neurons.

To address the subcellular distribution of functional protein at pre- and postsynaptic membranes, we next examined immunolabeling for the protein presynaptically in well-defined GABAergic synapse populations: (1) putative

basket cell terminals forming symmetric synaptic contacts with cell bodies of principal cells (Figure 11B); (2) axo-axonic synapses on the axon initial segment (AIS) of principal cells (Figure 11C); and (3) axo-dendritic inhibitory synapses forming contact onto dendritic shafts of principal cells in the CA1 and CA3 area (Figure 11D). All types of inhibitory synapses were identified based on their symmetric contact to the postsynaptic component. In all these three major inhibitory presynaptic axon terminals, we could occasionally detect labeling for SNAP47, suggesting that SNAP47 could be trafficked to presynaptic sites also in inhibitory neuron populations. Finally, we investigated labeling postsynaptically, in IN dendrites in the neuropil. Indeed, immunogold particles for SNAP47 protein were consistently found to be localized, albeit at low levels, to non-spiny dendritic shafts of putative INs receiving convergent asymmetrical, presumably excitatory synapses in the *stratum radiatum* of the CA1 area (Figure 11E).

Thus, the immunogold labeling pattern of SNAP47 in INs observed in the electron microscope indicates trafficking of this protein to both pre- and postsynaptic compartments.

DISCUSSION

The present study reveals a divergent distribution of SNAP47 in mouse and rat hippocampus. While immunolabeling for SNAP47 is broadly distributed in all areas and layers of the hippocampus in both the mouse and rat, it shows an almost complementary staining pattern. In the mouse the strongest labeling was observed in VGAT-positive inhibitory INs of the hippocampus, whereas in the rat hippocampus the highest level of immunostaining was observed in the termination zone of the excitatory MF projection. Independent of these differences in areal and cellular distribution, at the subcellular level the protein was found to be localized to both postsynaptic and presynaptic elements, with higher densities in postsynaptic elements.

High Expression of the SNAP47 in Somata of GABAergic INs in the Mouse

Immunofluorescence labeling for SNAP47 revealed a strong expression of this protein in cell body layers of the mouse hippocampus. Furthermore, particularly high labeling was observed in somata scattered in all areas and layers corresponding to inhibitory GABAergic INs. This finding is in good agreement with previous documented localization of this protein in cell bodies of cultured striatal neurons (Holt et al., 2006). Although the precise subcellular localization could not be identified in that study, our postembedding immunogold data suggest that the protein is closely associated to the ER in both GABAergic VGAT-positive and glutamatergic pyramidal neuron populations. This pool could recruit factors involved in the regulation of the structural organization of the ER or Golgi-ER and post-Golgi transport possibly through interaction with cytoskeletal elements

(Kuster et al., 2015), but the precise role remains to be established.

The high accumulation of SNAP47 in inhibitory GABAergic neurons of the adult mouse hippocampus was an unexpected finding. Previously, Tafoya et al. (2006) reported a high expression of SNAP25 in GABAergic terminals (gt) of the hippocampus and the thalamus, however this finding was contrasted by several reports suggesting the lack of SNAP25 in hippocampal GABAergic axon terminals (Verderio et al., 2004; Bragina et al., 2007; Matteoli et al., 2009). In contrast, SNAP23 has been reported to be highly and selectively expressed in at least a subset of hippocampal and neocortical inhibitory axon terminals (Verderio et al., 2004; Bragina et al., 2007). Our results indicate that GABAergic neurons in the mouse hippocampus synthesize SNAP47 at high levels and the functional protein can be localized both postsynaptically in somato-dendritic compartments and presynaptically in axon terminals. In the rat somatic expression levels were markedly lower than in the mouse, albeit not absent, suggesting that the storage and trafficking of this SNAP isoform underlies species-dependent regulatory mechanisms. Further investigations are necessary to identify the precise localization and role of the functional protein in diverse IN populations and whether, despite a low presynaptic expression, it can participate in the SNARE complexes involved in supporting vesicle fusion in GABAergic boutons.

Post- and Presynaptic Expression of SNAP47 at Glutamatergic Synapses

In the rat hippocampus, SNAP47 immunolabeling of the cell body layers was weak, whereas the neuropil, in particular the CA3 *stratum lucidum* where MFs terminate showed strong staining. We could detect SNAP47 at high level in subset of dendritic spines, and showed localization similar to the postsynaptic marker. This finding is consistent with the conclusion from a previous study demonstrating that SNAP47 is present in postsynaptic compartments and an essential component of the fusion machinery required for regulated AMPAR insertion to the membrane during the expression of LTP (Jurado et al., 2013). However, the protein does not contribute to the regulation of basal AMPAR- or NMDAR-mediated synaptic responses or basal AMPAR surface expression (Jurado et al., 2013). The study by Jurado et al. (2013) did not allow any conclusions about the specific dendritic nanodomains at which AMPAR exocytosis occurs during LTP or about the specific timing of these events. Other studies have found that following NMDAR activation, recombinant AMPAR subunits are inserted into perisynaptic membranes, either adjacent to the PSD or adjacent to the base of dendritic spines, from where they can laterally diffuse into the PSD to increase synaptic strength (Petrini et al., 2009; Opazo et al., 2010). The sources of the AMPARs that are exocytosed during LTP have been suggested to be recycling endosomes containing transferrin receptors (TfRs) in dendrite spines (Jurado et al., 2013). As there is a close correlation between dendritic spine size and PSD size (Harris and Stevens, 1989) and between PSD

size and AMPAR density at synapses (Takumi et al., 1999), small spines in the *stratum radiatum* are likely to contain lower numbers of AMPARs. Assuming that SNAP47 expression is proportional to AMPAR numbers, this could explain the higher intensity of SNAP47 labeling in complex spines in CA3 *stratum lucidum* in comparison to spines in CA3 *stratum radiatum* in rat hippocampus, as observed in our study. In general, predominant localization of SNAP47 to the postsynaptic elements supports role of this protein in the control of receptor trafficking.

In our study, we could also confirm presynaptic localization of SNAP47 in glutamatergic synapses. The labeling intensity was particularly high in MFBs in CA3 *stratum lucidum* in the rat. We could detect co-localization of SNAP47 immunofluorescence signal with both VGLUT1- and ZnT3 in MFBs, but not all MFBs were labeled and the overlap was weaker than with the postsynaptic marker. In fact, postembedding immunogold-labeling confirmed these findings and demonstrated that SNAP47 immunogold particles were present presynaptically in the majority of MFBs however at substantially lower densities than postsynaptically in the complex spines of CA3 pyramidal cells.

The presynaptic localization of SNAP47 in MFBs may have important implications in vesicular exocytosis of BDNF (Shimojo et al., 2015). BDNF is stored in discrete vesicles within MFBs and some MFB-filopodia (Danzer et al., 2004; Dieni et al., 2012). BDNF-containing clusters co-localize neither with SV markers such as synaptophysin or VGLUT1, nor with proteins that are stored in dense core vesicle fractions. In good agreement, the staining pattern for SNAP47 was different from established markers for synapses. Furthermore, the co-fractionation pattern indicates that a pool of SNAP47 resides on a subpopulation of small vesicles, but the nature and origin of these vesicles remains to be established (Holt et al., 2006). Synaptic BDNF is not uniquely stored in MFBs, but was generally found in discrete synaptic granules/vesicles in majority of glutamatergic axon terminals in cultured hippocampal neurons (Andreska et al., 2014). Based on our results which show irregular, clustered localization of SNAP47 within glutamatergic presynaptic boutons, different from the homogenous vesicular labeling for VGLUT1, we hypothesize a co-localization of BDNF and SNAP47. Moreover, as BDNF protein is further localized in cell bodies (Conner et al., 1997) and SNAP47 protein is also accumulated in neuronal (glutamatergic and GABAergic) cell bodies. This co-localization pattern seems not to be restricted to MFBs, but may be a general principal for all neuronal compartments.

In summary, our work shows that SNAP47 is present postsynaptically at high levels in a subset of postsynaptic elements, including CA3 complex spines in the *stratum lucidum* and small spines in the CA1 and CA3 *stratum radiatum*. However, SNAP47 is also present presynaptically at lower levels in subsets of axon terminals, including MFBs and small excitatory axon terminals in the *stratum radiatum*. Concluding, our data suggest that SNAP47 may be involved not only in postsynaptic function but also in unique fusion machinery, distinct from

the one involved in neurotransmitter release at the presynaptic sites.

Future Perspectives

With respect to the strong accumulation of SNAP47 in GABAergic cell bodies and the co-localization of GABA pre- and postsynaptic markers with this SNAP isoform examined in the present study, it will be of interest to clarify its precise cellular and subcellular expression in various types of inhibitory neurons and to identify the mechanisms that regulate its intracellular distribution and trafficking and will help us better understand the functions of SNAP47 protein in GABAergic neurons. The preferential localization of SNAP47 to the postsynaptic components in the rat at physiological conditions raises the question whether the trafficking of this protein, in terms of favored localization to the presynaptic terminals and/or postsynaptic sites, could be changed dynamically during development or brain disorders.

AUTHOR CONTRIBUTIONS

AM-W and IV designed the experiments and analyzed the data; HH performed immunohistochemical labeling experiments; FB performed confocal image acquisition and quantification of immunofluorescence; TT prepared lentivirus construct, western blot analysis and all probes for *in situ* hybridization; HH and AM-W performed *in situ* hybridization; YY generated VGAT-Venus transgenic mice and rats; AM-W performed electron microscopic imaging and quantification; AM-W and IV prepared the manuscript.

FUNDING

This work was supported by the Deutsche Forschungsgemeinschaft (EXC 257 to IV).

ACKNOWLEDGMENTS

We thank Jie Song for his contribution of performing confocal image acquisition. We also thank Denis Lajkó, Katja Pötschke and Bettina Brokowski for technical assistance with *in situ* hybridization and western blotting. VGAT-Venus transgenic rats were generated by Drs. Y. Yanagawa, M. Hirabayashi and Y. Kawaguchi in National Institute for Physiological Sciences, Okazaki, Japan, using pCS2-Venus provided by Dr. Atsushi Miyawaki, Riken, Japan.

SUPPLEMENTARY MATERIAL

The Supplementary Material for this article can be found online at: <http://journal.frontiersin.org/article/10.3389/fnana.2017.00056/full#supplementary-material>

REFERENCES

- Alonso-Nanclares, L., Minelli, A., Melone, M., Edwards, R. H., Defelipe, J., and Conti, F. (2004). Perisomatic glutamatergic axon terminals: a novel feature of cortical synaptology revealed by vesicular glutamate transporter 1 immunostaining. *Neuroscience* 123, 547–556. doi: 10.1016/j.neuroscience.2003.09.033
- Andreska, T., Aufmkolk, S., Sauer, M., and Blum, R. (2014). High abundance of BDNF within glutamatergic presynapses of cultured hippocampal neurons. *Front. Cell. Neurosci.* 8:107. doi: 10.3389/fncel.2014.00107
- Booker, S. A., Gross, A., Althof, D., Shigemoto, R., Bettler, B., Frotscher, M., et al. (2013). Differential GABAB-receptor-mediated effects in perisomatic- and dendrite-targeting parvalbumin interneurons. *J. Neurosci.* 33, 7961–7974. doi: 10.1523/JNEUROSCI.1186-12.2013
- Booker, S. A., Song, J., and Vida, I. (2014). Whole-cell patch-clamp recordings from morphologically- and neurochemically-identified hippocampal interneurons. *J. Vis. Exp.* 91:e51706. doi: 10.3791/51706
- Bragina, L., Candiracci, C., Barbaresi, P., Giovedi, S., Benfenati, F., and Conti, F. (2007). Heterogeneity of glutamatergic and GABAergic release machinery in cerebral cortex. *Neuroscience* 146, 1829–1840. doi: 10.1016/j.neuroscience.2007.02.060
- Buckby, L. E., Mummery, R., Crompton, M. R., Beesley, P. W., and Empson, R. M. (2004). Comparison of neuroplastin and synaptic marker protein expression in acute and cultured organotypic hippocampal slices from rat. *Dev. Brain Res.* 150, 1–7. doi: 10.1016/j.devbrainres.2004.01.006
- Chang, C. L., Trimbuch, T., Chao, H. T., Jordan, J. C., Herman, M. A., and Rosenmund, C. (2014). Investigation of synapse formation and function in a glutamatergic-GABAergic two-neuron microcircuit. *J. Neurosci.* 34, 855–868. doi: 10.1523/JNEUROSCI.0229-13.2014
- Conner, J. M., Lauterborn, J. C., Yan, Q., Gall, C. M., and Varon, S. (1997). Distribution of brain-derived neurotrophic factor (BDNF) protein and mRNA in the normal adult rat CNS: evidence for anterograde axonal transport. *J. Neurosci.* 17, 2295–2313.
- Danzer, S. C., He, X., and McNamara, J. O. (2004). Ontogeny of seizure-induced increases in BDNF immunoreactivity and TrkB receptor activation in rat hippocampus. *Hippocampus* 14, 345–355. doi: 10.1002/hipo.10190
- Dieni, S., Matsumoto, T., Dekkers, M., Rauskolb, S., Ionescu, M. S., Deogracias, R., et al. (2012). BDNF and its pro-peptide are stored in presynaptic dense core vesicles in brain neurons. *J. Cell Biol.* 196, 775–788. doi: 10.1083/jcb.201201038
- Frotscher, M., Soriano, E., and Misgeld, U. (1994). Divergence of hippocampal mossy fibers. *Synapse* 16, 148–160. doi: 10.1002/syn.890160208
- Garbelli, R., Inverardi, F., Medici, V., Amadeo, A., Verderio, C., Matteoli, M., et al. (2008). Heterogeneous expression of SNAP-25 in rat and human brain. *J. Comp. Neurol.* 506, 373–386. doi: 10.1002/cne.21589
- Harris, K. M., and Stevens, J. K. (1989). Dendritic spines of CA 1 pyramidal cells in the rat hippocampus: serial electron microscopy with reference to their biophysical characteristics. *J. Neurosci.* 9, 2982–2997.
- Hohenstein, A. C., and Roche, P. A. (2001). SNAP-29 is a promiscuous syntaxin-binding SNARE. *Biochem. Biophys. Res. Commun.* 285, 167–171. doi: 10.1006/bbrc.2001.5141
- Holt, M., Varoqueaux, F., Wiederhold, K., Takamori, S., Urlaub, H., Fasshauer, D., et al. (2006). Identification of SNAP-47, a novel Qbc-SNARE with ubiquitous expression. *J. Biol. Chem.* 281, 17076–17083. doi: 10.1074/jbc.M513838200
- Jahn, R., Lang, T., and Südhof, T. C. (2003). Membrane fusion. *Cell* 112, 519–533. doi: 10.1016/S0092-8674(03)00112-0
- Jahn, R., and Scheller, R. H. (2006). SNAREs—engines for membrane fusion. *Nat. Rev. Mol. Cell Biol.* 7, 631–643. doi: 10.1038/nrm2002
- Jurado, S., Goswami, D., Zhang, Y., Molina, A. J., Südhof, T. C., and Malenka, R. C. (2013). LTP requires a unique postsynaptic SNARE fusion machinery. *Neuron* 77, 542–558. doi: 10.1016/j.neuron.2012.11.029
- Kornau, H. C., Schenker, L. T., Kennedy, M. B., and Seeburg, P. H. (1995). Domain interaction between NMDA receptor subunits and the postsynaptic density protein PSD-95. *Science* 269, 1737–1740. doi: 10.1126/science.7569905
- Kuster, A., Nola, S., Dingli, F., Vacca, B., Gauchy, C., Beaujouan, J. C., et al. (2015). The Q-soluble N-Ethylmaleimide-sensitive factor attachment protein receptor (Q-SNARE) SNAP-47 regulates trafficking of selected vesicle-associated membrane proteins (VAMPs). *J. Biol. Chem.* 290, 28056–28069. doi: 10.1074/jbc.M115.666362
- Lois, C., Hong, E. J., Pease, S., Brown, E. J., and Baltimore, D. (2002). Germline transmission and tissue-specific expression of transgenes delivered by lentiviral vectors. *Science* 295, 868–872. doi: 10.1126/science.1067081
- Matteoli, M., Pozzi, D., Grumelli, C., Condliffe, S. B., Frassoni, C., Harkany, T., et al. (2009). The synaptic split of SNAP-25: different roles in glutamatergic and GABAergic neurons? *Neuroscience* 158, 223–230. doi: 10.1016/j.neuroscience.2008.03.014
- Müller, B. M., Kistner, U., Kindler, S., Chung, W. J., Kuhlendahl, S., Lau, L.-F., et al. (1996). SAP102, a novel postsynaptic protein that interacts with the cytoplasmic tail of the NMDA receptor subunit NR2B. *Neuron* 17, 255–265.
- Nagai, T., Iba, K., Park, E. S., Kubota, M., Mikoshiba, K., and Miyawaki, A. (2002). A variant of yellow fluorescent protein with fast and efficient maturation for cell-biological applications. *Nat. Biotechnol.* 20, 87–90. doi: 10.1038/nbt0102-87
- Opazo, P., Labrecque, S., Tigaret, C. M., Frouin, A., Wiseman, P. W., De Koninck, P., et al. (2010). CaMKII triggers the diffusional trapping of surface AMPARs through phosphorylation of stargazin. *Neuron* 67, 239–252. doi: 10.1016/j.neuron.2010.06.007
- Petrini, E. M., Lu, J., Cognet, L., Lounis, B., Ehlers, M. D., and Choquet, D. (2009). Endocytic trafficking and recycling maintain a pool of mobile surface AMPA receptors required for synaptic potentiation. *Neuron* 63, 92–105. doi: 10.1016/j.neuron.2009.05.025
- Rao, A., Kim, E., Sheng, M., and Craig, A. M. (1998). Heterogeneity in the molecular composition of excitatory postsynaptic sites during development of hippocampal neurons in culture. *J. Neurosci.* 18, 1217–1229.
- Ravichandran, V., Chawla, A., and Roche, P. A. (1996). Identification of a novel syntaxin- and synaptobrevin/VAMP-binding protein, SNAP-23, expressed in non-neuronal tissues. *J. Biol. Chem.* 271, 13300–13303. doi: 10.1074/jbc.271.23.13300
- Ridler, T. W., and Calvard, S. (1978). Picture thresholding using an iterative selection method. *IEEE Trans. Syst. Man Cybern.* 8, 630–632. doi: 10.1109/tsmc.1978.4310039
- Shimojo, M., Courchet, J., Pieraut, S., Torabi-Rander, N., Sando, R., Polleux, F., et al. (2015). SNAREs controlling vesicular release of BDNF and development of callosal axons. *Cell Rep.* 11, 1054–1066. doi: 10.1016/j.celrep.2015.04.032
- Steggmaier, M., Yang, B., Yoo, J. S., Huang, B., Shen, M., Yu, S., et al. (1998). Three novel proteins of the syntaxin/SNAP-25 family. *J. Biol. Chem.* 273, 34171–34179. doi: 10.1074/jbc.273.51.34171
- Südhof, T. C. (2004). The synaptic vesicle cycle. *Annu. Rev. Neurosci.* 27, 509–547. doi: 10.1146/annurev.neuro.26.041002.131412
- Suh, Y. H., Terashima, A., Petralia, R. S., Wenthold, R. J., Isaac, J. T., Roche, K. W., et al. (2010). A neuronal role for SNAP-23 in postsynaptic glutamate receptor trafficking. *Nat. Neurosci.* 13, 338–343. doi: 10.1038/nn.2488
- Tafola, L. C., Mameli, M., Miyashita, T., Guzowski, J. F., Valenzuela, C. F., and Wilson, M. C. (2006). Expression and function of SNAP-25 as a universal SNARE component in GABAergic neurons. *J. Neurosci.* 26, 7826–7838. doi: 10.1523/jneurosci.1866-06.2006
- Takamori, S., Holt, M., Stenius, K., Lemke, E. A., Grønborg, M., Riedel, D., et al. (2006). Molecular anatomy of a trafficking organelle. *Cell* 127, 831–846. doi: 10.1016/j.cell.2006.10.030
- Takumi, Y., Ramírez-León, V., Laake, P., Rinivik, E., and Ottersen, O. P. (1999). Different modes of expression of AMPA and NMDA receptors in hippocampal synapses. *Nat. Neurosci.* 2, 618–624. doi: 10.1038/10172
- Tomasoni, R., Repetto, D., Morini, R., Elia, C., Gardoni, F., Di Luca, M., et al. (2013). SNAP-25 regulates spine formation through postsynaptic binding to p140Cap. *Nat. Commun.* 4:2136. doi: 10.1038/ncomms3136
- Uematsu, M., Hirai, Y., Karube, F., Ebihara, S., Kato, M., Abe, K., et al. (2008). Quantitative chemical composition of cortical GABAergic neurons revealed in transgenic venus-expressing rats. *Cereb. Cortex* 18, 315–330. doi: 10.1093/cercor/bhm056

- Verderio, C., Pozzi, D., Pravettoni, E., Inverardi, F., Schenk, U., Coco, S., et al. (2004). SNAP-25 modulation of calcium dynamics underlies differences in GABAergic and glutamatergic responsiveness to depolarization. *Neuron* 41, 599–610. doi: 10.1016/s0896-6273(04)00077-7
- Wang, Y., Kakizaki, T., Sakagami, H., Saito, K., Ebihara, S., Kato, M., et al. (2009). Fluorescent labeling of both GABAergic and glycinergic neurons in vesicular GABA transporter (VGAT)-Venus transgenic mouse. *Neuroscience* 164, 1031–1043. doi: 10.1016/j.neuroscience.2009.09.010
- Wang, G., Witkin, J. W., Hao, G., Bankaitis, V. A., Scherer, P. E., and Baldini, G. (1997). Syndet is a novel SNAP-25 related protein expressed in many tissues. *J. Cell Sci.* 110, 505–513.
- Wenzel, H. J., Cole, T. B., Born, D. E., Schwartzkroin, P. A., and Palmiter, R. D. (1997). Ultrastructural localization of zinc transporter-3 (ZnT-3) to synaptic vesicle membranes within mossy fiber boutons in the hippocampus of mouse and monkey. *Proc. Natl. Acad. Sci. U S A* 94, 12676–12681.
- Conflict of Interest Statement:** The authors declare that the research was conducted in the absence of any commercial or financial relationships that could be construed as a potential conflict of interest.
- Copyright © 2017 Münster-Wandowski, Heilmann, Bolduan, Trimbuch, Yanagawa and Vida. This is an open-access article distributed under the terms of the Creative Commons Attribution License (CC BY). The use, distribution or reproduction in other forums is permitted, provided the original author(s) or licensor are credited and that the original publication in this journal is cited, in accordance with accepted academic practice. No use, distribution or reproduction is permitted which does not comply with these terms.

4. Curriculum vitae

Mein Lebenslauf wird aus datenschutzrechtlichen Gründen in der elektronischen Version meiner Arbeit nicht veröffentlicht

5. List of Publications

- 09/2020 Bolduan F, Grosser S, Vida I. (2020) Minimizing shrinkage of acute brain slices using metal spacers during histological embedding. *Brain Struct Funct* **225**, 2577–2589. Published 2020, Sep 12.
- 01/2020 Gidon A, Zolnik T, Fidzinski P, Bolduan F, Papoutsi A, Poirazi P, Holtkamp M, Vida I, Larkum M. (2020) Dendritic action potentials and the computational properties of human layer 2/3 cortical neurons. *Science*, 124, 45-59. Published 2020, Jan 03.
- 07/2017 Münster-Wandowski A, Heilmann H, Bolduan F, Trimbuch T, Yanagawa Y, Vida I. (2017) Distinct Localization of SNAP47 Protein in GABAergic and Glutamatergic Neurons in the Mouse and the Rat Hippocampus. *Frontiers in Neuroanatomy*, 11, 56. Published 2017, Jul 13.

6. Danksagung

An dieser Stelle möchte ich meinen Dank an all diejenigen aussprechen, die mir während meiner Promotion geholfen haben.

Insbesondere danke ich meinem Doktorvater und Betreuer Prof. Dr. Imre Vida, der mich seitdem ich 2015 in seinem Institut anfing stets unterstützt hat, in schwierigen Phasen seine Hilfe anbot und damit maßgeblich am Abschluss dieser Dissertation beteiligt war. Aber auch den anderen Mitgliedern der Arbeitsgruppe danke ich sehr. Vor allem Dr. Sabine Grosser und Alix Guinet, die nicht nur bei der Arbeit unterstützten, sondern beide durch ihre freundliche und humorvolle Art die Zeit im Labor stets angenehm gestalteten. Auch danke ich Claudius Degro, der mich in der ersten Zeit eingearbeitet hat und Dr. Agnieszka Münster-Wandowski, die mich schon früh an einem ihrer Projekte mitarbeiten ließ.

Besonders möchte ich auch meinen engen Freundinnen und Freunden danken, dass sie immer da waren.

Und zuletzt, aber besonders stark, danke ich meinen Eltern und meinem Bruder, die mich während der Promotionszeit, aber natürlich auch unabhängig davon, stets in allen Belangen unterstützten.

Felix Bolduan, Dezember 2020